VYSOKÉ UČENÍ TECHNICKÉ V BRNĚ

Fakulta strojního inženýrství

DIPLOMOVÁ PRÁCE

Brno, 2017 Bc. Jakub Planer

VYSOKÉ UČENÍ TECHNICKÉ V BRNĚ
BRNO UNIVERSITY OF TECHNOLOGY

FAKULTA STROJNÍHO INŽENÝRSTVÍ
FACULTY OF MECHANICAL ENGINEERING

ÚSTAV FYZIKÁLNÍHO INŽENÝRSTVÍ
INSTITUTE OF PHYSICAL ENGINEERING

AB-INITIO VÝPOČTY ELEKTRONICKÝCH A STRUKTURNÍCH VLASTNOSTÍ OLOVO-ZIRKONÁTU-TITANÁTU (PZT)

FIRST-PRINCIPLES STUDIES OF THE ELECTRONIC AND STRUCTURAL PROPERTIES OF LEAD ZIRCONATE TITANATE (PZT)

DIPLOMOVÁ PRÁCE
MASTER'S THESIS

AUTOR PRÁCE — **Bc. Jakub Planer**
AUTHOR

VEDOUCÍ PRÁCE — **Ing. Miroslav Bartošík, Ph.D.**
SUPERVISOR

BRNO 2017

VYSOKÉ UČENÍ TECHNICKÉ V BRNĚ
FAKULTA STROJNÍHO INŽENÝRSTVÍ

Zadání diplomové práce

Ústav:	Ústav fyzikálního inženýrství
Student:	**Bc. Jakub Planer**
Studijní program:	Aplikované vědy v inženýrství
Studijní obor:	Fyzikální inženýrství a nanotechnologie
Vedoucí práce:	**Ing. Miroslav Bartošík, Ph.D.**
Akademický rok:	2016/17

Ředitel ústavu Vám v souladu se zákonem č.111/1998 o vysokých školách a se Studijním a zkušebním řádem VUT v Brně určuje následující téma diplomové práce:

Ab-initio výpočty elektronických a strukturních vlastností olovo-zirkonátu-titanátu (PZT)

Stručná charakteristika problematiky úkolu:

Olovo-zirkonát-titanát (PZT) je intenzivně studovaný materiál díky svým unikátním vlastnostem jako je ferroelektricita a piezoelektricita. Tyto vlastnosti mohou být využity například v senzorech, počítačových pamětích, polovodičových součástkách nebo v palivových článcích. Ačkoli je tento materiál intenzivně studovaný po mnoho let, některé aspekty stále nejsou dostatečně vysvětleny. Současné experimenty ukazují neobvyklý průběh iontové vodivosti dopovaného PZT perovskitu akceptorovými příměsmi, kde hraje důležitou roli vznik kyslíkových vakancí. Tato diplomová práce se snaží vysvětlit tento efekt pomocí výpočtů dle teorie funkcionálu hustoty (DFT) s využitím již vyvinutých počítačových programů.

Cíle diplomové práce:

1) Vysvětlete teoretické metody použité v této práci
2) Proveďte rešerši literatury. Shrňte strukturní a elektronické vlastnosti olovo-zirkonátu-titanátu a jejich praktické využití
3) Vypočítejte v programu VASP (Vienna Ab Initio Simulation Package) strukturní a elektronické vlastnosti PZT perovskitu s důrazem na formování kyslíkových vakancí. Tyto výsledky použijte k výpočtu difuzních koeficientů kyslíkových vakancí a vyšetřete vliv poměru zirkonia a titanu v materiálu na iontovou vodivost PZT perovskitu.
4) Diskutujte výsledky výpočtů s ohledem na nedávno provedené experimenty

Seznam literatury:

IZYUMSKAYA, N., ALIVOV, Y. -I., CHO, S. -J., MORKOÇ, H., LEE, H. a KANG, Y. -S. 2007. Processing, Structure, Properties, and Applications of PZT Thin Films. Critical Reviews in Solid State and Materials Sciences. 32(3), 111-202. DOI: 10.1080/10408430701707347

SÁGHI-SZABÓ, G., COHEN, R. E., KRAKAUER, H., MORKOÇ, H., LEE, H. a KANG, Y. -S. 1999. First-principles study of piezoelectricity in tetragonal PbTiO3 and PbZr0.5Ti0.5O3. Physical Review B. 59(20), 12771-12776. DOI: 10.1103/PhysRevB.59.12771

BOUKAMP, B., PHAM, M., BLANK, D., BOUWMEESTER, H., LEE, H. a KANG, Y. -S. 1999. Ionic and electronic conductivity in lead–zirconate–titanate (PZT). Physical Review B. 59(20), 12771-12776. DOI: 10.1016/j.ssi.2004.03.005

Termín odevzdání diplomové práce je stanoven časovým plánem akademického roku 2016/17

V Brně, dne

L. S.

prof. RNDr. Tomáš Šikola, CSc. ředitel ústavu	doc. Ing. Jaroslav Katolický, Ph.D. děkan fakulty

Abstrakt
Tato práce je zaměřena na výpočty difuzních bariér kyslíkových vakancí v olovo-zirkonátu-titanátu a jeho komponent pomocí teorie funkcionálu hustoty. Zjistili jsme, že velikost bariér je různá v olovo titanátu a olovo zirkonátu, což je způsobené rozdílnou lokalizací elektronů pocházejících ze vzniku kyslíkových vakancí. Difuzní bariéry byly nadále určeny pro směs s vysokým podílem titanu a porovnány s experimentálními výsledky. Přínos této práce spočívá v objasnění neobvykle nízkých difuzních koeficientů, které byly experimentálně měřeny na olovo-zirkonátu-titanátu. Zjistili jsme, že elektronové stavy vyvolané přítomností kyslíkových vakancí vytváří lokální vazby mezi atomy olova, což způsobuje, že kyslíkové vakance jsou nepohyblivé v důsledku zvýšení aktivační energie difuzního procesu.

Summary
This work is focused on Density Functional Theory (DFT) calculations of oxygen vacancy diffusion barriers in mixed perovskite lead zirconate titanate and its pure counterparts. We found out that barrier heights are different in lead titanate and lead zirconate caused by the different localization of the excess electrons due to the oxygen vacancy formation. Diffusion barriers were also determined for titanium-rich mixed phases and compared to experimental values. This work contributes to clarify unusually low experimentally measured diffusion coefficients in PZT. We found out that the induced vacancy states are forming localized bonds to the lead atoms which causes the oxygen vacancies to become immobile due to the increase of the activation energy of the diffusion process.

Klíčová slova
olovo zirkonát, olovo titanát, olovo zirkonát titanát, kyslíkové vakance, difuze, aktivační energie, teorie funkcionálu hustoty

Keywords
lead zirconate, lead titanate, lead zirconate titanate, oxygen vacancies, diffusion, activation energy, density functional theory

PLANER, J. *Ab-initio výpočty elektronických a strukturních vlastností olovo-zirkonátu-titanátu (PZT)*. Brno: Vysoké učení technické v Brně, Faculty of Mechanical Engineering, 2017. 86 s. Vedoucí diplomové práce: Ing. Miroslav Bartošík, Ph.D.

PROHLÁŠENÍ

Prohlašuji, že svou diplomovou práci na téma "*Ab-initio* výpočty elektronických a strukturních vlastností olovo-zirkonátu-titanátu" jsem vypracoval samostatně pod vedením vedoucího diplomové práce a s použitím odborné literatury a dalších informačních zdrojů, které jsou všechny citovány v práci a uvedeny v seznamu literatury na konci práce.

Jako autor uvedené diplomové práce dále prohlašuji, že v souvislosti s vytvořením této diplomové práce jsem neporušil autorská práva třetích osob, zejména jsem nezasáhl nedovoleným způsobem do cizích autorských práv osobnostních a jsem si plně vědom následků porušení ustanovení § 11 a následujících autorského zákona č. 121/2000 Sb., včetně možných trestněprávních důsledků vyplývajících z ustanovení § 152 trestního zákona č. 140/1961 Sb.

Brno ....

(podpis autora)

I would like to express my sincere gratitude to all people who allowed me to work on this diploma thesis and who helped me along the way. First of all, I would like to thank Prof. **Josef Redinger** who admitted me into the Computational Materials Science group on my Erasmus stay and who conscientiously supervised my diploma thesis in Vienna. Dr. **Florian Mittendorfer** helped me a lot by giving advices, discussing occured problems and he is also responsible for reduction of mistakes in this work and he deserves my words of thanks. I am also very grateful to Ing. **Miroslav Bartošík**, Ph.D. who supervised my diploma thesis in Brno and Prof. **Tomáš Šikola** that he allowed me to work on this topic. It was an honor for me to work with Dipl.-Ing. **Wernfried Mayr-Schmölzer** who was my long-suffering trainer on my Erasmus stay and advisor when calculations didn't work. It was a pleasure for me to work with Dr. **Michael Wolloch** and Dipl.-Ing. **Johannes Gugler** in the same office and enjoy their sense of humour.

Dále bych chtěl poděkovat svým sourozencům a všem lidem, kteří mi byli na blízku. Avšak největší dík si zaslouží moji rodiče za jejich trpělivost a celoživotní podporu.

Děkuji.

Bc. Jakub Planer

Contents

1. Introduction

In 1880, Paul-Jacques Curie and his younger brother Pierre Curie discovered the piezoelectric effect. It is a reversible process in certain materials in which an electric potential is generated when the material is subjected to the mechanical stress or vibration. Nowadays this effect is being used even in everyday applications, like actuators, microphones, pickups, piezoelectric motors and many others. Furthermore, some piezoelectric materials evince an unusual property which is called ferroelectricity. This effect was discovered in 1920 on a Rochelle salt by Joseph Valasek and it is similar to the ferromagnetism. In certain materials there is a spontaneous permanent polarization which can be reversed with an external electric field. This property is in a big interest of scientists, e.g., in order to make a tunable capacitors.

One of the materials evincing ferroelectricity and piezoelectricity is called Lead Zirconate Titanate (PZT). Nowadays, it is an intensively studied material which can be employed, for example, in the Non-Volatile Random-Access-Memories (NVRAM), sensors, actuators and transducers applications. Properties of this material can be modulated by doping – adding impurities to the material. This process is mainly known from the semiconductor production of p-type and n-type dopants.

Even through a lot of experimental work has been done to investigate this material, several aspects are still not well understood. Recent experiments show an unusually low ionic conductivity of acceptor-doped PZT ceramics where the formation of oxygen vacancies plays an important role and the aim of this work is to clarify these phenomena which play an important role in applications.

This work supplements very recent experimental results with computer simulations and sheds light on a diffusion process of oxygen vacancies in pure lead titanate, lead zirconate and mixed compounds.

Chapter 2 is focused on the computational methods used in this thesis. They are derived from quantum mechanics and offer a way how to approximately solve a many-body problem with a reasonable computational power. Chapter 3 introduces methods which use the periodic properties of crystals to effectively solve the quantum mechanical problem. In the last methodological chapter 4, we describe methods for evaluating the energy barriers of oxygen vacancy diffusion. These barriers are related to the measured ionic conductivity in experiments. Chapter 5 introduces structural properties of lead zirconate titanate, its applications, and how these properties can be tuned with different dopants. Chapter 6 is focused on structural and electronic properties of the pure edge components of PZT ceramics, related to oxygen vacancy diffusion. The calculated diffusion barriers are discussed and serve to set up proper models for PZT alloys. In the last chapter 7 we move to the titanium-rich PZT alloys and discuss the results obtained from calculations of oxygen diffusion barriers.

2. Computational methods

Since computers have become in recent years more and more powerful, computational methods have been developed in order to study materials at an atomistic level. The first group of these methods is based on the classical (Newtonian) mechanics where the atoms are considered to be the fundamental objects, having specific mass and charge, which interact with other atoms in the system. Nowadays it is possible to treat systems consisting of millions of atoms using the molecular mechanics methods. Their disadvantage lies in the use of the empirical force fields which are unable to describe the quantum effects, and in the huge number of the required empirical parameters for the atomic systems.

The second group of the computational methods is based on quantum mechanics. These methods are aimed at calculating the electronic structure from the many-body Schrödinger equation of an atomic system. Unlike the classical methods, the basic elements of the quantum systems are atomic nuclei and electrons. Solving the atomic systems with the help of the quantum mechanics is much more demanding so the largest systems may contain a few thousands of atoms. The advantage of these methods is the fact that we need much less empirical parameters. First-principles methods don't even need any of them and offer a useful way how to study the electronic properties of the systems, which are essential for the purposes of this thesis. Unfortunately, it is not possible to solve analytically more complex quantum systems than the hydrogen atom and several approximations have to be introduced. This chapter gives a brief outline of used theoretical concepts.

2.1. The basic concepts

In 1929, Erwin Schrödinger published the equation, which is the fundamental object for studying quantum mechanical systems[1]. This equation is the basic tool in quantum mechanics because it determines the state of the system and its time evolution. The time-dependent Schrödinger equation can be written in the following way.

$$\hat{H}\Psi(\mathbf{r}_1, \mathbf{r}_2, \ldots, \mathbf{r}_N, t) = i\hbar \frac{\partial \Psi(\mathbf{r}_1, \mathbf{r}_2, \ldots, \mathbf{r}_N, t)}{\partial t} \tag{2.1}$$

Equation 2.1 is classified as the partial differential equation, second order in the spatial variables and first order in time.

$\hat{H}$ denotes the Hamiltonian operator describing the total energy of the system. We often want to study time independent systems. To remove the time domain from the equation, separation of variables can be used to rewrite the wave function in terms of the stationary wave function and the time propagation.

$$\Psi(\mathbf{r}_1, \mathbf{r}_2, \ldots, \mathbf{r}_N, t) = \Psi_{\mathrm{S}}(\mathbf{r}_1, \mathbf{r}_2, \ldots, \mathbf{r}_N) e^{-\frac{iE}{\hbar}t} \tag{2.2}$$

By substituting the wave function 2.2 to the equation 2.1, we receive time-independent Schrödinger equation which is the starting point for the following introduction to the computational methods.

[1] Erwin Schrödinger won the Nobel Prize in Physics for a derivation of his equation in 1933.

In contrast to the classical mechanics where the state of the system is given by the set of positions and momentums for each particle, the state of the quantum mechanical system containing N particles is given by the wave function $\Psi(\mathbf{r}_1, \mathbf{r}_2, \ldots, \mathbf{r}_N, t)$ and all properties of the system can be determined by solving the eigenvalue problem of the corresponding operator acting on the wave function. The eigenvalues of an operator correspond to a macroscopic observable. Because the quantum mechanical systems are simultaneously in all possible configurations with certain probabilities, it is only possible to calculate the expectation values of the system properties as the sum of the all eigenvalues weighted with the corresponding probability. The expectation value O can be calculated from the wave function and the operator according to the following equation (in Dirac's bra-ket and classical notation):

$$O = \langle \Psi | \hat{O} | \Psi \rangle = \int \cdots \int_{-\infty}^{\infty} \Psi^*(\mathbf{r}_1, \mathbf{r}_2, \ldots, \mathbf{r}_N) \hat{O} \Psi(\mathbf{r}_1, \mathbf{r}_2, \ldots, \mathbf{r}_N) \, d\mathbf{r}_1 \, d\mathbf{r}_2 \ldots d\mathbf{r}_N \qquad (2.3)$$

Atomic units

Quantum mechanical systems usually deal with the atomic particles, e.g., protons or electrons and the basic properties of such particles are expressed with very small numbers, sometimes exceeding all the prefixes in the standard SI system. The system of atomic units provides more comprehensible numbers and also simplifies the form of used equations. The atomic units for the length, charge, mass and energy is presented in the following way:

- atomic unit of charge is the charge of the proton, which is equal to $1.6022 \times 10^{-19}\,\mathrm{C}$
- atomic unit of length is the Bohr radius and is calculated to be $a_0 = \hbar^2/m_e e^2 = 5.2918 \times 10^{-11}\,\mathrm{m} = 0.529\,18\,\text{Å}$.
- the mass of the electron, $m_\mathrm{e} = 9,1059 \cdot 10^{-31}\mathrm{kg}$ represents one atomic unit of mass
- atomic unit of energy – 1 Hartree – is given by $E_a = e^2/4\pi\epsilon_0 a_0 = 4.3598 \times 10^{-18}\,\mathrm{J} = 27.2114\,\mathrm{eV}$.

In this work we use the atomic units to present the equations. The results will be given for convenience in angstroms and electron volts.

Born-Oppenheimer approximation

Using atomic units, Schrödinger equation of the system containing N electrons and M nuclei with charges Z_n can be written as

$$\left\{ -\frac{1}{2}\sum_{i=1}^{N}\nabla_i^2 - \frac{1}{2}\sum_{j=1}^{M}\frac{\nabla_j^2}{m_n} + \frac{1}{2}\cdot\left(\sum_{j\neq j'}^{M}\frac{Z_j Z_{j'}}{r_{jj'}} - 2\sum_{i=1}^{M}\sum_{j=1}^{N}\frac{Z_i}{r_{ij}} + \sum_{i\neq i'}^{N}\frac{1}{r_{ii'}}\right)\right\}\Psi = E\Psi$$

$$\left\{\hat{T}_e + \hat{T}_n + \hat{V}_{ee} + \hat{V}_{en} + \hat{V}_{nn}\right\}\Psi = E\Psi \qquad (2.4)$$

The index i is related to electrons and j to nuclei in the system, m_n denotes mass of the nuclei in the system and Z_n are their charges. The terms can be written in the form

of operators acting on the wave function Ψ as the second part of the equation shows. The first two operators $\hat{T}_e$ and $\hat{T}_n$ are related to the kinetic energy of the electrons and nuclei. The rest of the terms describe the Coulomb interactions in the system. They are successively related to the electron-electron repulsion, electron-nuclei attraction and nuclei-nuclei repulsion. Unfortunately, the exact analytical solution of more complex systems than the hydrogen atoms is unknown[2]. In practice, the reasonable models could consist of many hundreds of atoms and therefore several approximations are needed.

The first, widely used approximation is based on the separation of the motion of the nuclei from the motion of the electrons. The proton itself is 1836 times heavier than the electron and from equation 2.4 it is clear that the expectation value of $\hat{T}_n$ will be very small. The Born-Oppenheimer approximation sets the masses of the nuclei m_n to infinity so the nuclei are static. The electrons thus move in the static potential given by the fixed positions of the nuclei. Performing this approximation, the electronic Hamiltonian has the following form

$$\hat{H}_e = -\frac{1}{2}\sum_{i=1}^{N}\nabla_i^2 + \frac{1}{2}\cdot\left(-2\sum_{i=1}^{M}\sum_{j=1}^{N}\frac{Z_i}{r_{ij}} + \sum_{i=1}^{N}\sum_{j\neq i}^{N}\frac{1}{r_{ij}}\right) = \hat{T}_e + \hat{V}_{ee} + \hat{V}_{en} \tag{2.5}$$

In other words, the fully interacting system is reduced to the decoupled subsystems which are shown in the figure 2.1. In the first subsystem, electrons interact with themselves and with fixed nuclei. The second subsystem describes the nuclei moving in the effective field given by the electrons. Since the electronic and nuclear part of the Hamiltonian have been decoupled, we can rewrite the wave function of the system ψ_S into the following form.

$$\psi_S(\mathbf{r}_i, \mathbf{R}_j) = \psi_e(\mathbf{r}_i, \{\mathbf{R}_j\})\psi_N(\mathbf{R}_j) \tag{2.6}$$

ψ_e is related to the electronic system where the coordinates of the nuclei are fixed, ψ_N notes the wave function describing the nuclei moving in the effective field given by the electrons. We often assume that the nuclei don't move. In that case, the energy of the system is equal to the energy of the electronic system augmented by the electrostatic energy of the nuclei.

In practice, the Born-Oppenheimer approximation can be used to find the electronic ground states and vibrational modes. In other cases, it is a starting point for the perturbation theory describing other phenomena like electron-phonon interactions [1], polaron formation, metal-insulator transitions, and the Bardeen–Cooper–Schrieffer theory of superconductivity [2].

Unfortunately, solving the electronic Hamiltonian presented in the equation 2.5 is still impossible for larger systems and therefore other approximations have to be introduced. The electron-electron interaction is usually decoupled and the many-electron problem is split to the one-electron systems where the interaction between the electrons is replaced

[2]For larger systems like the hydrogen molecule or helium atom, the Schrödinger equation turns into the many-body problem, which is analytically insoluble. Nevertheless, the solution of the Schrödinger equation for the hydrogen atom is extremely useful in solving the approximated systems

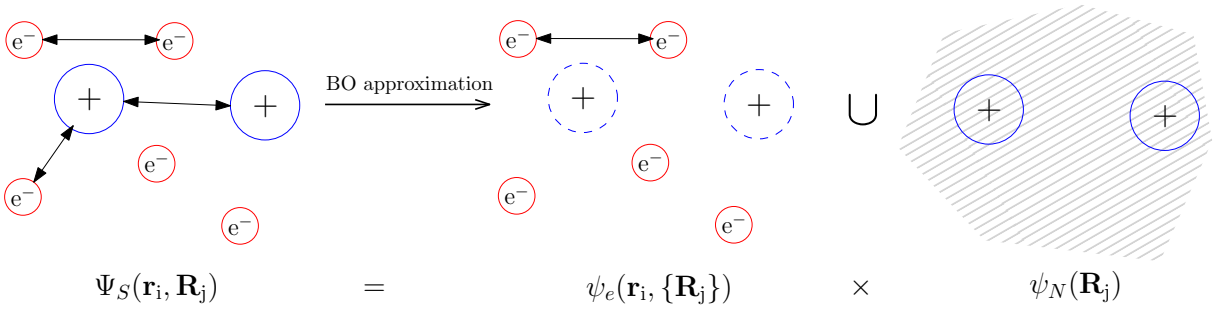

Figure 2.1: Scheme of the Born-Oppenheimer approximation. Full-interacting system with electron-electron, electron-nuclei and nuclei-nuclei interactions is split into two separated systems. The first system consists of interacting electrons moving in the external potential given by nuclei. In the second system we consider the nuclei moving in the effective field given by electrons.

by an average potential, resulting into the independent-particles problem which is soluble. The independent-particles Hamiltonian has always the following form:

$$\hat{H}_{IP} = \sum_{i=1}^{N} \left[\frac{\nabla_i^2}{2} + V\big(\mathbf{r}_i, \{\mathbf{R}_j\}\big) \right] \tag{2.7}$$

where $V\big(\mathbf{r}_i, \{\mathbf{R}_j\}\big)$ is an effective potential in which the electron moves. This potential is generally non-local operator which means that value of the potential at the certain position $\mathbf{r}$ is also dependent on other positions $\mathbf{r}'$. It results into the problem that the value of the potential depends on the distribution of other electrons. In the following sections, two different approaches how to create the independent-particle system with an effective potential $V\big(\mathbf{r}_i, \{\mathbf{R}_j\}\big)$ are going to be discussed.

2.2. Hartree-Fock method

Hartree-Fock method neglects all correlation effects of the interacting system except the antisymmetry of the wave function. Nevertheless, this method provides accurate results in many cases and is used mainly together with density functional theory (DFT).

To keep the antisymmetry, a many-body wave function is expressed as the Slater determinant of one-electron spin-orbitals[3].

$$\psi_S(\mathbf{x}_1, \mathbf{x}_2, \dots) = \frac{1}{\sqrt{N!}} \begin{vmatrix} \psi_1(\mathbf{x}_1) & \psi_2(\mathbf{x}_1) & \dots & \psi_N(\mathbf{x}_1) \\ \psi_1(\mathbf{x}_2) & \psi_2(\mathbf{x}_2) & \dots & \psi_N(\mathbf{x}_2) \\ \vdots & \vdots & \ddots & \vdots \\ \psi_1(\mathbf{x}_N) & \psi_2(\mathbf{x}_N) & \dots & \psi_N(\mathbf{x}_N) \end{vmatrix} \tag{2.8}$$

[3]Spin of the electron proceeds from the Dirac's equation which combines Schrödinger equation with the special theory of relativity. Spin of the electron can be artificially added to the non-relativistic Schrödinger equation with the help of spin-orbitals, which introduces a spin coordinate to the one-electron wave function. If the spin-orbit coupling is neglected, spin-orbitals are orthogonal to each other.

The result of the antisymmetric wave function is the Pauli's exclusion principle which states that two fermions can't occur in the same state, described by the same quantum numbers. The antisymmetry of the wave function is defined as

$$\psi_A(\mathbf{x}_1, \mathbf{x}_2, \ldots, \mathbf{x}_{i-1}, \mathbf{x}_i, \cdots, \mathbf{x}_N) = -\psi_A(\mathbf{x}_1, \mathbf{x}_2, \ldots, \mathbf{x}_i, \mathbf{x}_{i-1}, \cdots, \mathbf{x}_N)$$

We suppose that single particle wave functions $\psi_i(\mathbf{x}_j)$ in equation 2.8 are orthonormal and then the constant $1/\sqrt{N!}$ normalizes the wave function of the system. Variables $\mathbf{x}_i$ contain both position and spin of the electrons. To solve the many-body problem within the Hartree-Fock approximation, a variational principle can be used to derive the Hartree-Fock equations. In principle, we are looking for the wave function which provides the minimal total energy.

$$E_{tot} = \langle \psi_S | \hat{H}_e | \psi_S \rangle$$

Using orthonormality of the spin-orbitals and Lagrange multiplier method to keep the spin-orbitals orthonormal, we obtain the Hartree-Fock equations [3]:

$$\begin{aligned} -\frac{1}{2}\nabla_i^2\psi_i(\mathbf{r}_i) - \sum_{j=1}^{M}\frac{Z_j}{r_{ij}}\psi_i(\mathbf{r}_i) + \sum_{j\neq i}^{N}\left[\int \frac{|\psi_j(\mathbf{r}_j)|^2}{|\mathbf{r}_i - \mathbf{r}_j|}\mathrm{d}\mathbf{r}_j\psi_i(\mathbf{r}_i) - \right. \\ \left. -\delta(\sigma_i, \sigma_j)\int \frac{\psi_j^*(\mathbf{r}_j)\psi_i(\mathbf{r}_j)}{|\mathbf{r}_i - \mathbf{r}_j|}\mathrm{d}\mathbf{r}_j\psi_j(\mathbf{r}_i)\right] = \epsilon_i\psi_i(\mathbf{r}_i) \end{aligned} \tag{2.9}$$

The first term corresponds to the kinetic energy of the electron. The second term describes the potential energy of the electron in an electrostatic field generated by nuclei. The last two terms are connected with electron-electron interactions. The first of them is called Coulomb and the second one Exchange operator. Equation 2.9 can be rewritten in the form of a one-electron Schrödinger-like equation

$$\mathscr{F}\psi_i(\mathbf{r}_i) = \epsilon_i\psi_i(\mathbf{r}_i) \tag{2.10}$$

Where $\mathscr{F}$ is the Fock operator consisting of the operators mentioned above.

To express the one-electron wave functions, a finite basis set can be used

$$\psi_i(\mathbf{r}_i) = \sum_{j=1}^{k} C_{ij}\phi_j(\mathbf{r}_i) \tag{2.11}$$

and the optimal constants C_{ij} needed to be determined. If we multiply the left and the right side of the equation 2.10 by any of the basis function ϕ_j^* and integrate over the all space and spin coordinates, we will receive one by one the linear equations for variables C_{ij}. This system of the linear equations can be expressed in the matrix form:

$$\hat{\mathbf{F}}\mathbf{C} = \epsilon\hat{\mathbf{S}}\mathbf{C}, \tag{2.12}$$

$\hat{\mathbf{F}}$ is the Fock matrix, ϵ notes the eigenvalue and $\hat{\mathbf{S}}$ is the overlap matrix. This problem can be efficiently solved with the help of computer and several packages designed for the matrix diagonalization, e.g. LAPACK [4] (Linear Algebra PACKage).

Hartree-Fock method gives in many cases reasonable results because of the exact form of the exchange energy. The energy given by Hartree-Fock method is a bit higher than exact energy because of the neglect of electron correlations. To describe the correlation effects, methods beyond Hartree-Fock were developed. The most used are the Configuration Interaction method [5], the Coupled Cluster method [6] and methods based on Perturbation Theory [7].

The Hartree-Fock method suffers from several disadvantages. E.g. this method becomes time demanding when it is used on larger systems, because the computational costs of evaluating the wave function scales with $N^{2.2-2.3}$ [8]. The second disadvantage is the complete neglect of the correlation effects of the full interacting system and it might lead to large differences from experimental results.

2.3. Density functional theory

In the previous section we have seen that Hartree-Fock method tries to evaluate the properties of the system (e.g. the total energy) using the wave function. However, in real systems, the many-body wave function which belongs to the $3N$-dimensional Hilbert space is a too complicated object and it is impossible to calculate the properties of the system for a reasonable computational cost.

Density functional theory is based on the proof that any property of a fully-interacting system can be described as a functional of the ground state density ρ_0 which is only a function of 3 space variables. It is therefore sufficient to deal with the density which is a much simpler object than the wave function. In 1964, Pierre Hohenberg and Walter Kohn published a paper in which they described this method as an exact theory for any interacting system with an external time-independent potential $V_{ext}(\mathbf{r})$ [9]. This formulation also includes the full interacting electronic systems within the Born-Oppenheimer approximation discussed in section 2. However, the work doesn't provide a way how to construct these functionals and in fact, their exact forms except for the one-electron systems are unknown and they need to be approximated.

Hohenberg-Kohn Theorems

The basis of DFT consists of two theorems published by Pierre Hohenberg and Walter Kohn. The proofs of these theorems are surprisingly easy and it is possible to find them e.g. in [2]. The theorems are valid for all many-body systems including the electrons moving in the Coulomb potential given by fixed nuclei. The Hamiltonian of this system can be expressed in the form of eq. 2.5 and the Coulomb interaction of the nuclei may be added later.

Hohenberg-Kohn theorem 1: *For any system of interacting particles in an external potential* $V_{\text{ext}}(\mathbf{r})$*, the potential* $V_{\text{ext}}(\mathbf{r})$ *is determined uniquely, except for a constant, by the ground state particle density* $\rho_0(\mathbf{r})$.

The ground state electron density $\rho(\mathbf{r})$ thus determines the whole Hamiltonian of the system. If the Hamiltonian is determined, it means that also the wave function of the ground state and all excited states are determined together with all other properties of the system.

Hohenberg-Kohn theorem 2: *The ground state energy can be obtained variationally: the density that minimizes the total energy which is given by a universal functional $E[\rho]$ is the exact ground state density ρ_0.*

In other words, it is possible to determine the exact ground state density only with the help of the functional $E[\rho]$ by minimizing the total energy. Unfortunately, excited states must be found in a different way. The first statement is restricted to the non-degenerate ground states and its proof is trivial. The second statement can be proven by *reductio ad absurdum*.

$$\begin{array}{ccc} V_{\text{ext}}(\mathbf{r}) & \overset{\text{HK}}{\Longleftrightarrow} & \rho_0(\mathbf{r}) \\ \Downarrow & & \Uparrow \\ \Psi_{\text{i}}(\{\mathbf{r}\}) & \Rightarrow & \Psi_0(\{\mathbf{r}\}) \end{array}$$

Figure 2.2: Visualisation of the Hohenberg-Kohn theorem. $V_{\text{ext}}(\mathbf{r})$ determines in the Schrödinger equation all eigenstates $\Psi_i(\{\mathbf{r}\})$. The eigenstate resulting in the lowest energy of the system is called ground state $\Psi_0(\{\mathbf{r}\})$. The ground state wave function yields the ground state electron density $\rho_0(\mathbf{r})$ and Hohenberg-Kohn theorem proves that there is one-to-one relation between this density and the external potential $V_{\text{ext}}(\mathbf{r})$.

It means that external potential V_{ext}, non-degenerate ground state $|\Psi_0\rangle$ and electron density $\rho(\mathbf{r})$ are determined uniquely by each other as it is shown in the figure 2.2. It was mentioned that all ground state properties and ground state energy are defined by the electron density. Unfortunately, Hohenberg-Kohn theorems don't provide any way how to obtain the explicit form of the functional $E[\rho]$. The way how to map the interacting particles problem onto a suitable effective non-interacting system is described in the following section.

2.3.1. Kohn-Sham scheme

As figure 2.3 shows, Kohn-Sham scheme [10] makes a relation between the full-interacting many-body system with an external potential V_{ext} and a non-interacting system of electrons moving in an effective potential V_{eff}. HK theorems prove that the ground state energy of N interacting particles in the potential V_{ext} can be described by the same ground state density of an auxiliary system of N non-interacting particles. The Hamiltonian of the auxiliary system consists of the operator of the kinetic energy $\hat{T}$ and an effective local potential V_{eff} acting on an electron. Even when the exact form of the effective potential is unknown, we can build its approximated form. This is the cardinal advantage of the auxiliary system and the whole point of the Kohn-Sham scheme, because the original full-interacting electronic system is intractable with respect to the DFT. In the following text we describe how the effective potential is constructed.

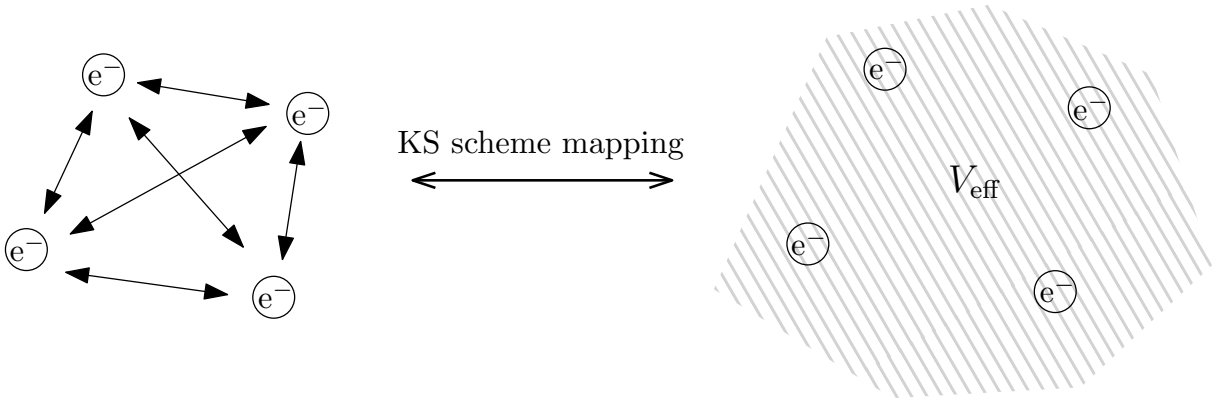

Figure 2.3: Kohn-Sham scheme. Full-interacting electronic system is mapped onto an auxiliary non-interacting system with an effective potential V_{eff}, which yields the same ground state density ρ_0 as the original system. According to the Hohenberg-Kohn theorems, these systems are equivalent.

A functional of the total energy of the full-interacting system can be in principle rewritten into the following form

$$E[\rho] = T[\rho] + U[\rho] + V[\rho] \tag{2.13}$$

The functional of total energy is split into the three functionals describing the different interactions which contribute to the total energy. The first term, $T[\rho]$ is related to the kinetic energy of the electrons. Electron-electron interaction is described with the functional $U[\rho]$. Interactions with the nuclei are included in the last functional, $V[\rho]$. The explicit forms of $T[\rho]$ and $U[\rho]$ are unknown.

Let's consider an auxiliary, non-interacting system. In that case, we can calculate the kinetic term as well as the potential energy of the electrons using the Hartree or Hartree-Fock approximation. Functional of the kinetic energy in the interacting system, $T[\rho]$ can be replaced by a functional of an auxiliary system $T_n[\rho]$.

$$T[\rho] = T_n[\rho] + T_c[\rho] \tag{2.14}$$

$T_c[\rho]$ denotes the kinetic correlation functional which is defined as the difference between the kinetic energy of the full-interacting and auxiliary system. $T_n[\rho]$ can be expressed with the help of single-particle orbitals ϕ_i as

$$T_n[\rho] = -\frac{1}{2}\sum_{i=1}^{N}\int \mathrm{d}^3 r \phi_i^*(\mathbf{r})\nabla_i^2\phi_i(\mathbf{r}) \tag{2.15}$$

where the electronic density ρ is calculated from the orbitals ϕ_i.

$$\rho = \sum_{i=1}^{N}\int \mathrm{d}^3 r \phi_i(\mathbf{r})\phi_i^*(\mathbf{r}) \tag{2.16}$$

In similar way we can also express the functional $U[\rho]$. It is possible to calculate the Hartree term of the potential energy and summarize the missing contributions in the exchange-correlation functional $U_{xc}[\rho]$. This correction term suppresses the self-interaction

error[4] and includes the correlation energy describing the electron-electron interaction in the original system.

$$U[\rho] = U_H[\rho] + U_{xc}[\rho] \tag{2.17}$$

In summary, the functional of the total energy can be expressed with the help of the three terms from the auxiliary system. The last term contains the corrections between the full-interacting and auxiliary system.

$$E[\rho] = T_n[\rho] + U_H[\rho] + V[\rho] + E_{xc}[\rho] \tag{2.18}$$

The term $E_{xc}[\rho]$ is called exchange-correlation functional and includes the self-interaction energy and correlation energy from the kinetic and potential terms. This functional is defined in the way to include all the effects arising from many-body problem. In summary, the exchange-correlation functional is equal to

$$E_{xc}[\rho] = \langle \hat{T} \rangle - T_n[\rho] + \langle \hat{U} \rangle - U_H[\rho] \tag{2.19}$$

Kohn-Sham equations

According to the second Hohenberg-Kohn theorem, we can find the ground state density variationally. The problem of finding the proper density which results in the ground state energy can be viewed as the problem of minimization of the total energy with respect to density ρ. Our aim is to find the formula for an effective potential V_{eff} of an auxiliary system. For the interacting system we can write

$$0 = \frac{\delta E[\rho]}{\delta \rho} = \frac{\delta T_n[\rho]}{\delta \rho} + \frac{\delta U_H[\rho]}{\delta \rho} + \frac{\delta V[\rho]}{\delta \rho} + \frac{\delta E_{xc}[\rho]}{\delta \rho} \tag{2.20}$$

For the *auxiliary*, non-interacting system with the same electron density, the total energy is equal to

$$E_{aux}[\rho] = T_n[\rho] + \int \mathrm{d}^3 r \rho(\mathbf{r}) V_{ext}(\mathbf{r}) \tag{2.21}$$

and we receive a similar result as for the interacting system

$$0 = \frac{\delta E_{aux}[\rho]}{\delta \rho} = \frac{\delta T_n[\rho]}{\delta \rho} + V_{ext}(\mathbf{r}) \tag{2.22}$$

One can see that the electron density can be determined from the *auxiliary* system with the external potential

$$V_{ext}(\mathbf{r}) = \frac{\delta U_H[\rho]}{\delta \rho} + \frac{\delta V[\rho]}{\delta \rho} + \frac{\delta E_{xc}[\rho]}{\delta \rho} \tag{2.23}$$

[4] Hartree term is calculated as the coulomb energy from the electron density.

$$U_H = \frac{1}{2} \int \mathrm{d}^3 r \mathrm{d}^3 r' \frac{\rho(\mathbf{r})\rho(\mathbf{r}')}{|\mathbf{r} - \mathbf{r}'|}$$

We don't know the contribution of the individual electrons to the total electron density and therefore electrons interact with themselves in this expression.

So the Schrödinger equation for non-interacting electrons has the form [3]

$$\left[-\frac{1}{2}\nabla_i^2 + \int \mathrm{d}^3 r' \rho(\mathbf{r}') \frac{1}{|\mathbf{r}-\mathbf{r}'|} + \sum_{i=1}^{M} \frac{Z_i}{|\mathbf{r}-\mathbf{R_i}|} + \frac{\delta E_{xc}[\rho]}{\delta \rho}\right] \phi_i(\mathbf{r}) = \epsilon_i \phi_i(\mathbf{r}) \tag{2.24}$$

where ρ is an electron density, $\mathbf{r}$ and $\mathbf{r}'$ note the position vectors, $\mathbf{R}_\mathrm{i}$ are positions of nuclei with charges Z_i. $\phi_i(\mathbf{r})$ denote one-electron functions and ϵ_i are corresponding eigenvalues. We have just derived so called Kohn-Sham equations which yield the correct ground state density for the interacting system. The total energy of the system is not just sum of the eigenvalues ϵ_i, but the formula can be derived from the equation 2.18. These equations are solved using the self-consistent loop shown in the figure 2.4, because the electron density is dependent on the one-electron orbitals which are being calculated. The first step is the initial guess of the electron density to construct the Schrödinger-like equation. In the next steps, Kohn-Sham equations are solved and new electron density from the Kohn-Sham orbitals is created. This procedure is repeated until a convergence criterion is reached.

2.3.2. Exchange-correlation functionals

It was mentioned that we do not know the exact form of the exchange-correlation functional and some approximations are needed. It turns out that it is possible to approximate $E_{xc}[\rho]$ with a local or semi-local functional with remarkably accurate results.

The general strategy for the evaluation of the exchange-correlation functional is to split it into the exchange and correlation term as it is shown in the eq. 2.25. The origin of the exchange and correlation effect is different so it is reasonable to handle them separately.

$$E_{xc}[\rho] = E_x[\rho] + E_c[\rho] \tag{2.25}$$

There is a certain freedom in defining both terms of the exchange-correlation functional and many ways have been developed how to describe this term. It is possible to divide them into local[5], semi-local[6], hybrid[7] and others[8]. In the following text we will briefly describe how are these functionals constructed.

Local Density Approximation (LDA)

The most simple approximation which still provides reasonable results for many systems is called Local Density Approximation (LDA). The exchange and correlation parts are calculated from the homogeneous electron gas model. We can define the exchange-correlation energy density $\epsilon_\mathrm{xc}(\rho(\mathbf{r}))$ which is a local function with respect to the electron density. The exchange-correlation energy is then calculated as an integral over the whole space with $\epsilon_{\mathrm{xc}(\rho(\mathbf{r}))}$ taken at each point of the space assumed to be the same as in a homogeneous

[5]The exchange-correlation energy depends only on the electron density at specific point of the space

[6]The exchange-correlation energy depends on the electron density and its gradient at the certain point of the space

[7]The exchange term is calculated within the Hartree-Fock method, correlation energy is usually mixed from more correlation parts of other functionals

[8]There are also other ways how to define the exchange-correlation functional, but it is not connected with this work

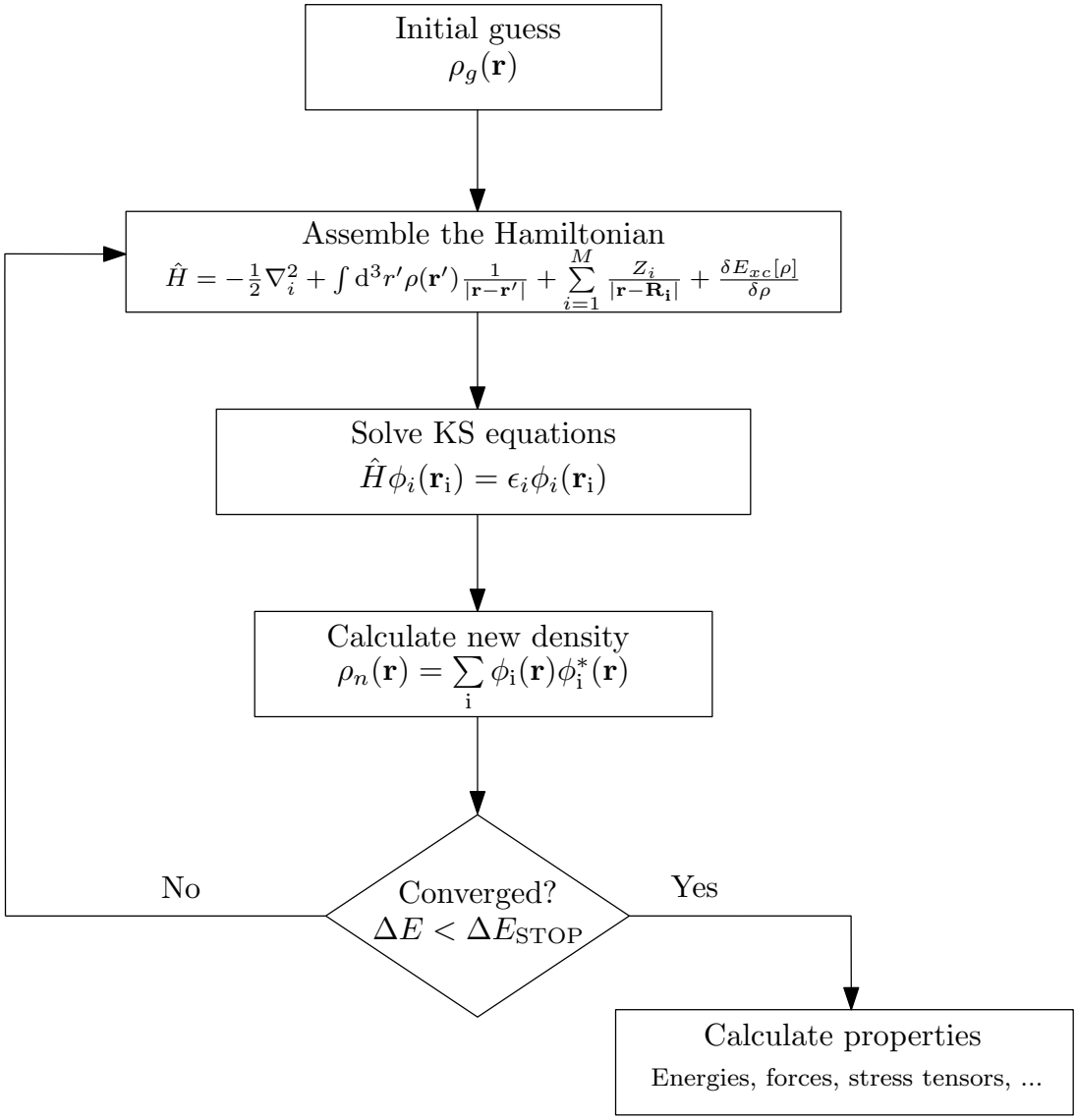

Figure 2.4: Scheme of the self-consistent DFT cycle.

electron gas with the same density. The exchange part is known for the homogeneous electron gas and can be evaluated according to this formula [11].

$$E_x^{\mathrm{LDA}}[\rho] = -\frac{3e^2}{4}\left(\frac{3}{\pi}\right)^{1/3} \int \mathrm{d}^3 r \rho^{4/3} \tag{2.26}$$

The correlation part E_c can be calculated using parametrized expressions taken from Quantum Monte Carlo calculations.

The Local Density Approximation works well for the systems where the exchange-correlation effects are short-ranged (e.g. nearly free-electron metal). If the density goes continuously to zero in the system (like in a one-atom system), LDA usually fails, mainly because of the large self-interaction errors in the exchange functional.

The systems where LDA doesn't work sufficiently are a motivation to improve the functionals with taking into account how is the electron density changing in the close surrounding.

Generalized gradient approximation (GGA)

The Local Density Approximation fails in the systems with rapidly changing electron density like molecules. To improve the description of these systems, the gradient of the electron density is taken into account to compute the exchange-correlation energy. These functionals are called semi-local because the gradient includes the information of the infinitesimal area around the point in the space where the exchange-correlation energy is calculated. Exchange correlation functional can thus be formally written in the following form.

$$E_{xc} = E_{xc}[\rho, \nabla\rho] \tag{2.27}$$

Generalized Gradient Approximation provides an improvement of the properties like ionization energies of the atoms, electron affinities, atomization energies, lattice parameters or surface energies [12]. On the other hand, in some cases GGA doesn't provide better results. For example, phonon frequencies are usually calculated more accurately with LDA [13]. The electronic properties of the materials like the band gap are also described insufficiently [14] and other approaches are needed to use in order to receive more accurate results. The functional used in this thesis which belongs to the GGA class is called PBE [15], named by the authors Perdew, Burke, Ernzerhof. In 2008, a modification of the PBE functional was invented. PBESol describes the equilibrium properties like lattice parameters, bond lengths better than PBE, but it is usually worse for the properties like atomization energies [16].

Hybrid functionals

It was mentioned that the the exchange-correlation functionals suppress the self-interaction error. The hybrid functionals combine the orbital dependent Hartree-Fock method where the exchange energy is calculated exactly, with a certain DFT functional which describes the correlation energy. The exact exchange energy can be expressed in the terms of the orbitals which is equal to

$$E_x^{HF} = -\frac{1}{2}\sum_{i,j}\int\int \psi_i^*(\mathbf{r}_i)\psi_j^*(\mathbf{r}_j)\frac{1}{|\mathbf{r}_i - \mathbf{r}_j|}\psi_j(\mathbf{r}_i)\psi_i(\mathbf{r}_j)\mathrm{d}\mathbf{r}_i\mathrm{d}\mathbf{r}_j \tag{2.28}$$

Even when the exchange operator is non-local, it can be implemented to the Kohn-Sham equations with using the optimized effective potential method [17]. Since the hybrid functional calculates the exchange energy from the Hartree-Fock method, the calculations are $10-100\times$ more expensive than regular DFT calculations. This is caused by evaluating two-electron integrals in equation 2.28.

Hybrid functionals can provide more accurate results for insulators because of the exact treatment of the exchange energy. For example, the B3LYP hybrid functional [18] which is widely used in the chemistry community defines the exchange-correlation energy as

$$E_{xc}^{B3LYP} = (1-a_0)E_x^{LSDA} + a_0E_x^{HF} + a_x\Delta E_x^{B88} + a_cE_c^{LYP} + (1-a_c)E_c^{VWN} \tag{2.29}$$

In periodic systems, the long-range exchange interaction cancels with the correlation effects so the non-local functional is needed to treat only for the short-range part of

the exchange interaction. This idea is used within the HSE functional [19], where the screened Coulomb potential is applied only to the exchange interaction in order to screen the long-range part of the Hartree-Fock exchange. The HSE functional has the form

$$E_{xc}^{HSE} = aE_x^{HF,SR}(\omega) + (1-a)E_x^{PBE,SR}(\omega) + E_x^{PBE,LR}(\omega) + E_c^{PBE} \tag{2.30}$$

The biggest advantage of the hybrid functionals is the improvement in the fields where the local or semi-local functionals fail. For example, there is a great progress in evaluation of the material properties such as band gap values, phonon spectra or the excitation energies.

3. Quantum mechanics in a periodic system

The previous chapter introduced the Density Functional Theory and the functionals which can be used in the Kohn-Sham scheme to calculate the electronic and structural properties of the materials from first principles. Nevertheless, a computational cost of DFT calculations doesn't allow to work with systems containing more than a few thousands of atoms. In this chapter we will describe the way how to convert a real solid crystal (usually consisting of $\sim 10^{23}$ atoms) to the much simpler system using the periodicity of the crystal. Mathematically, it is possible to solve the Schrödinger equation in a unit cell with proper boundary conditions instead of solving the problem for a chunk of material directly.

Crystals are considered to be perfectly translationally symmetric materials ordered in a periodic lattice. This lattice can be defined in real space by three basis vectors $\mathbf{a}_1$, $\mathbf{a}_2$, $\mathbf{a}_3$ as it is shown in figure 3.1. The positions in a lattice $\mathbf{R}$ are defined by a linear combination of the basis vectors

$$\mathbf{R} = \sum_{i=1}^{3} c_i \mathbf{a}_i \tag{3.1}$$

where the coefficients c_i are scalars.

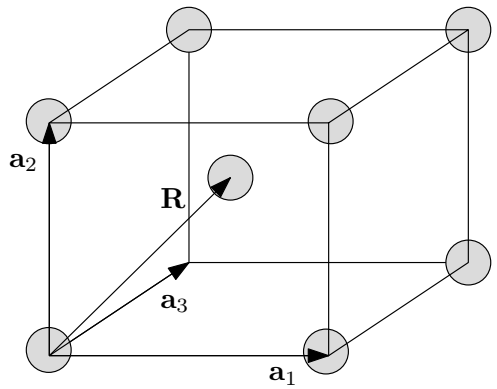

Figure 3.1: Scheme of the unit cell of a crystal. Vectors $\mathbf{a}_1$, $\mathbf{a}_2$, $\mathbf{a}_3$ represent lattice vectors, the position of atoms $\mathbf{R}$ in the unit cell can be obtained by the linear combination of the lattice vectors $\mathbf{a}_1$, $\mathbf{a}_2$, $\mathbf{a}_3$.

We have defined the unit cell in the real space as the smallest translationally invariant volume but it can be equally described in the reciprocal space, which is, as we will see, more suitable to build the whole mathematical formalism and to introduce reasonable approximations.

Any function which is periodic in a unit cell ($f(\mathbf{r}+\mathbf{T}) = f(\mathbf{r})$) can be expanded into the plane waves representation using the Fourier transform. The wave vectors $\mathbf{Q}$ used for the Fourier transform must fulfill the condition[1]

$$\mathbf{T} \cdot \mathbf{Q} = 2\pi n \tag{3.2}$$

Where $\mathbf{T}$ is the primitive lattice translational vector and n denotes an integer. Similarly in the reciprocal space, we can define the reciprocal basis set from which we can construct any suitable wave vector $\mathbf{Q}$ in the following way

$$\mathbf{Q} = \sum_{i=1}^{3} d_i \mathbf{b}_i \tag{3.3}$$

For this purpose, the basis vectors $\mathbf{b}_i$ must fulfill the condition

$$\mathbf{b}_i \cdot \mathbf{a}_j = 2\pi\delta_{ij} \tag{3.4}$$

Which can be provided by this explicit expression for the vectors $\mathbf{b}_i$.

$$\mathbf{b}_i = 2\pi\epsilon_{ikl}\frac{\mathbf{a}_k \times \mathbf{a}_l}{\mathbf{a}_1 \cdot \mathbf{a}_2 \times \mathbf{a}_3} \tag{3.5}$$

Where ϵ_{ikl} is a tensor which is equal to +1 for even ikl permutations and -1 for odd permutations.

Now we can define the first Brillouin zone as the volume of the reciprocal space consisting of the points which are closer to the origin than to any other reciprocal lattice point. It means that we can decompose any reciprocal vector $\mathbf{q}$ into the vector $\mathbf{k}$ located in the first Brillouin zone and a vector $\mathbf{Q}$ of the primitive reciprocal lattice.

$$\mathbf{q} = \mathbf{k} + \mathbf{Q} \tag{3.6}$$

It is possible to express the positions of the atoms and the Coulomb potential given by the cores in the reciprocal space. The only missing component which is needed to transform the Schrödinger from the real space to the reciprocal space, is the wave function. This is done with help of Bloch's theorem which uses the periodicity of a solid crystal to reduce the number of electrons in the whole crystal to the number of electrons in the unit cell.

[1] The wave vectors needed for the Fourier expansion must have the same periodicity as the expanded function. It means that

$$e^{i\mathbf{T}\cdot\mathbf{Q}} = 1$$

which results in the condition

$$\mathbf{T} \cdot \mathbf{Q} = 2\pi n$$

3.1. Bloch's theorem

Since the Hamiltonian in a periodic potential is invariant with respect to all lattice translations, the eigenvalues of the Hamiltonian can be chosen to be eigenvalues of the translational operators $\hat{T}_n$ as well, defined as

$$\hat{T}_n \psi(\mathbf{r}) = \psi(\mathbf{r} + \mathbf{T}_n) \tag{3.7}$$

It can be proven that the eigenstates of the translational operators are equal to $e^{i\mathbf{k}\cdot\mathbf{T}_n}$ and the equation 3.7 turns into

$$\hat{T}_n \psi(\mathbf{r}) = e^{i\mathbf{k}\cdot\mathbf{T}_n} \psi(\mathbf{r}) \tag{3.8}$$

which is known as the Bloch's theorem. The eigenstates of the Hamiltonian with a chosen wave vector $\mathbf{k}$ – $\psi_\mathbf{k}(\mathbf{r})$ can be expressed as

$$\psi(\mathbf{r}) = e^{i\mathbf{k}\mathbf{r}} u_\mathbf{k}(\mathbf{r}) \tag{3.9}$$

where $e^{i\mathbf{q}\mathbf{r}}$ is a plane wave and $u_\mathbf{k}(\mathbf{r})$ is a periodic function satisfying the condition

$$u_\mathbf{k}(\mathbf{r} + \mathbf{T}) = u_\mathbf{k}(\mathbf{r}) \tag{3.10}$$

A scheme of the Bloch wave is visible in figure 3.2. The periodic function $u_\mathbf{k}$ is modulated by the plane wave with proper boundary conditions. Using Bloch's theorem it is possible to solve the Schrödinger equation for the crystal considering only one unit cell for each wave vector $\mathbf{k}$ and periodic boundary conditions arising from equation 3.9. In principle, we can choose between reciprocal and real space. As we can see, reciprocal space takes into account symmetry of the crystal and in these cases it is the most used way to calculate the electronic properties.

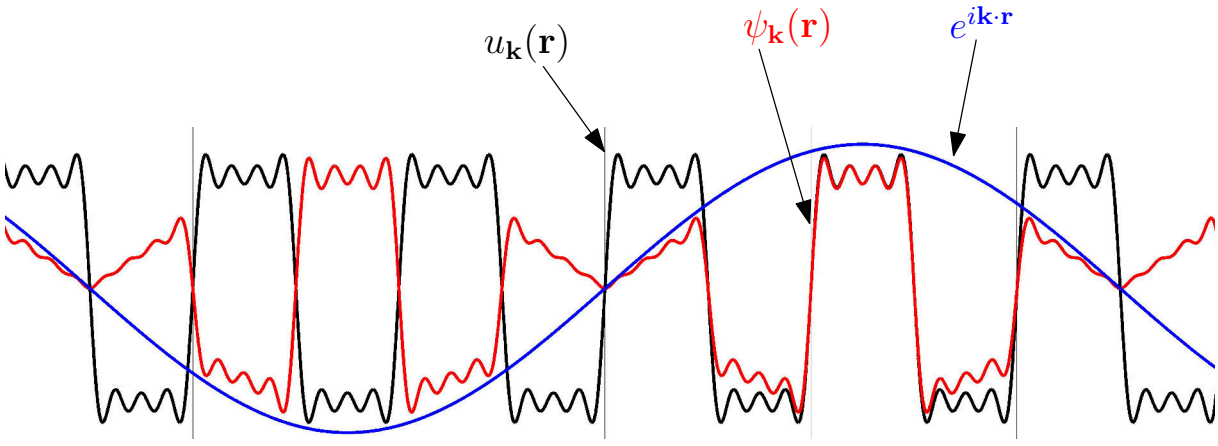

Figure 3.2: A scheme of the Bloch wave $\psi_\mathbf{k}(\mathbf{r})$ which consists of the periodic function $u_\mathbf{k}(\mathbf{r})$ modulated by the plane wave $e^{i\mathbf{k}\cdot\mathbf{r}}$ with the proper periodicity. Only the real parts of the functions are visible.

It turns out that all possible eigenstates defined by the wave vector $\mathbf{k}$ are included in the first Brillouin zone. This is very important for evaluating the physical properties like density of states, total energies, etc. because it is possible to build an approximation to calculate only the certain amount of the eigenstates and estimate the desired property

as the average value per unit cell. Any physical property can be calculated using the following formula

$$\overline{f} = \frac{1}{N_k} \sum_{\mathbf{k}} f_i(\mathbf{k}) \iff \frac{1}{\Omega_{BZ}} \int_{BZ} f_i(\mathbf{k}) \mathrm{d}\mathbf{k} \tag{3.11}$$

Where Ω_{BZ} is the volume of the first Brillouin zone and N_k denotes number of evaluated wave vectors. The right side of the equation 3.11 takes into account an infinite number wave vectors and the variable can be considered as continuous in the Fourier space.

3.2. Band structure methods

Using Bloch's theorem and the Fourier transform of the potential V, the Schrödinger equation can be written in the reciprocal space for each vector $\mathbf{k}$ in the first Brillouin zone

$$\left[\frac{1}{2}(\mathbf{k}+\mathbf{K})^2 - \epsilon\right] C_{\mathbf{k}+\mathbf{K}} + \sum_{\mathbf{K}'} V_{\mathbf{K}-\mathbf{K}'} C_{\mathbf{k}+\mathbf{K}'} = 0 \tag{3.12}$$

in the equation 3.12, the wave vectors $\mathbf{k}+\mathbf{K}$ and $\mathbf{k}'+\mathbf{K}'$ are decoupled and we can therefore solve the eigenvalue problem for each wave vector $\mathbf{k}$ from the first Brillouin zone separately. The eigenvalues ϵ form a discrete spectrum for all reciprocal vectors $\mathbf{k}$. The energy values are dependent on the level of the band and also on the wave vector $\mathbf{k}$. The eigenvalues can be thus labeled with respect to the wave vector $\mathbf{k}$ and the energy level n.

$$\epsilon = \epsilon_{n\mathbf{k}} \tag{3.13}$$

To solve the Schrödinger equation (3.12), it is necessary to define a proper basis set for the $u_{\mathbf{k}}(\mathbf{r})$ of the Bloch wave shown in equation 3.9. The most simple case is nearly free electron model in which the electrons are expressed in the form of plane waves, moving in a smooth potential. This approximation works well in the case of homogeneous electron gas or valence electrons in metals.

The tight-binding model works with the electrons which are tightly-bound to the nuclei and feel the spherically-symmetric Coulomb potential. The one-electron wave functions are expressed in terms of the atomic orbitals located around the nuclei. This approach is closely related to the Linear Combination of Atomic Orbitals (LCAO) method used in quantum chemistry. The tight-binding model was successfully, e.g. used to explain the band structure of the graphene.

However, it is clear that many systems wouldn't be sufficiently described neither within the nearly free electron approximation nor tight-binding model. These methods fail because the coulomb potential is strong in the vicinity of the cores, but smooth in the interstitial region. In theory, it is possible to express the periodic function of the Bloch wave in the plane wave basis set, but it turns out that the wave function rapidly oscillates only in the core region close to the nuclei and therefore a huge number of the plane waves would be necessary which would make the calculations time-demanding. For this reason, several more effective methods were developed which are more suitable to use in these cases.

3.2.1. Augmented plane wave method (APW)

The first approach that leads to a reduction of the number of plane waves considers the fact that a wave function of an electron strongly oscillates in the vicinity of cores, whereas in the region between the atoms, there are almost no oscillations. So in the augmented plane wave method [20], the wave function near the cores is expressed in terms of atomic-like functions, i.e.

$$\chi^{\mathrm{APW}}_{\mathbf{k}+\mathbf{K}} = \sum_{l} \sum_{m=-l}^{l} C_{lm}(\mathbf{k}+\mathbf{K}) A_{lm} \mathcal{R}_l(r) Y^l_m(\theta,\phi) \tag{3.14}$$

where $Y^l_m(\theta,\phi)$ are spherical harmonics and $\mathcal{R}_l(r)$ notes the solutions of the radial Schrödinger equation with a certain energy E. The expansion coefficients A_{lm} are found in the way to match the Bloch wave, $e^{i(\mathbf{k}+\mathbf{K})\cdot\mathbf{r}}$ outside the core region. It is important to note that the radial functions $\mathcal{R}_l(r)$ are energy-dependent and therefore the Hamiltonian will be also energy-dependent. It means that the equations are non-linear in energy and they have to be solved using the iterative schemes. However, this approach is very time-demanding.

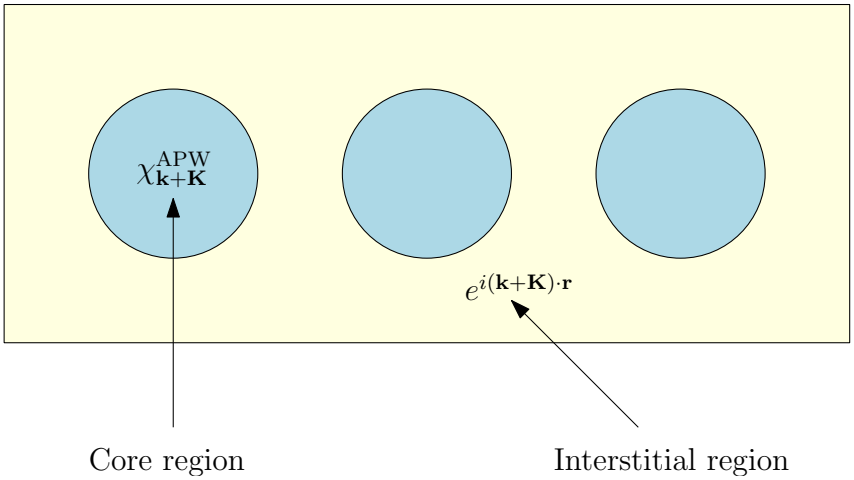

Figure 3.3: Scheme of the APW method. The wave function in the core region is expressed in terms of spherical harmonics, in the interstitial region where the potential is smooth, the basis functions are plane waves.

In order to avoid energy-dependence of the radial functions, the linearized augmented plane wave method (LAPW) was developed. The main idea is to use a set of pivot energies and employ their corresponding solutions of radial Schrödinger equation together with the energy derivatives.

3.2.2. Pseudopotentials

In section 3.2.1 we have seen that the Coulomb potential of nuclei gives rise to rapid oscillations of the wave function in the core region. In the pseudopotential methods, the real Coulomb potential is replaced with the weaker potential in the core region which matches the same potential in the interstitial region. As the consequence, the pseudopotential methods don't describe the core region right, but many properties of the systems

like bonding, electrical conductivity or the ionization energy depend only on the valence electrons which are located outside the core region and are therefore described correctly by the pseudopotential.

There are several requirements for the pseudopotential. First of all, the pseudo-wave function outside the core region must be the same as the wave function in the full-potential. The change of the potential results in the phase shift of the wave function. Therefore the pseudopotential must cause the phase shift equal to $2n \cdot \pi$ of the pseudo-wave function to obtain the same wave function in the interstitial region. This requirement also implies that there are more ways how to construct the pseudopotential. Figure 3.4 shows how

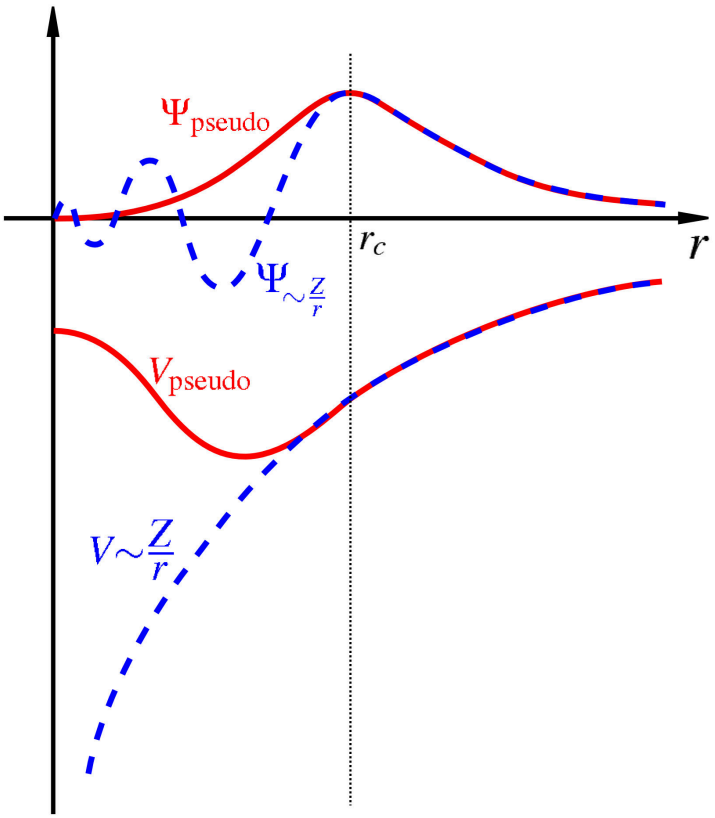

Figure 3.4: The principle of pseudopotentials. The pseudopotential V_{pseudo} is constructed in the way that the full-wave function Ψ and the pseudo-wave function Ψ_{pseudo} are equal beyond the radius r_c. Image taken from [21].

does the pseudopotentials work. The nodes of the full-wave function in the core region are removed while the wave function in the interstitial region remains unchanged. It means that the lower basis set of the plane waves is needed to describe the pseudo-wave function. The other requirement – transferability guarantees that the pseudopotential constructed in one system (usually an atom) can sufficiently well describe the properties of the valence electrons in other systems like atoms, molecules, bulks or surfaces.

Norm-conserving pseudopotentials [22] were developed in order to keep the right charge distribution in the core region for the pseudo-wave function $\tilde{\phi}(r)$ and full-wave function $\phi(r)$ is therefore satisfied this condition

$$4\pi \int_0^{r_c} \tilde{\phi}(r)\tilde{\phi}^*(r)r^2 \mathrm{d}r = 4\pi \int_0^{r_c} \phi(r)\phi^*(r)r^2 \mathrm{d}r \tag{3.15}$$

The second class of pseudopotentials were introduced by D. Vanderbilt in 1990 [23]. It offers a way how to even more decrease the number of the plane-waves that are needed to describe well the valence electrons. In this method, the norm-conserving condition is relaxed in order to make the pseudo-function as smooth as possible and augmentation charges are added to counterbalance the wrong charge distribution. These pseudopotentials are called ultrasoft because the pseudo-wave function is calculated with the lowest possible cut-off energy.

The disadvantage of the pseudopotential methods is that the wave function of the non-valence electrons is lost, which might influence certain calculated properties. Another drawback of this method is that the transferability of the pseudopotentials is not guaranteed and the results might be unreliable.

3.2.3. Projector augmented wave method (PAW)

In 1994, Peter Blöchl published the projector augmented wave method (PAW) [24], which provides a way how to calculate the all-electron wave function with a great computational efficiency, similar to the pseudopotential methods. The PAW method uses projectors to transform the strongly oscillating wave function in the core region to the smoother wave function, which can be expressed with a smaller basis set.

The PAW method seeks the linear operator $\hat{\mathcal{T}}$ which transforms the smooth pseudo-wave function $|\tilde{\Psi}\rangle$ into the all-electron wave function $|\Psi\rangle$.

$$|\Psi\rangle = \hat{\mathcal{T}}\,|\tilde{\Psi}\rangle \tag{3.16}$$

Since $|\Psi\rangle$ is smooth enough in the interstitial region, the transformation is only needed in the core region where the wave function oscillates strongly. The operator is written in this form

$$\hat{\mathcal{T}} = \mathbf{1} + \sum_R \hat{\mathcal{T}}_\mathrm{R} \tag{3.17}$$

where R is a position of an atom and $\hat{\mathcal{T}}_\mathrm{R}$ modifies the wave function only in the core region while it remains the wave function unchanged in the interstitial region. We require that the both all-electron wave function and pseudo-wave function can be expanded to the basis sets

$$|\Psi\rangle = \sum_i c_i^R\,|\phi_i^R\rangle \tag{3.18}$$

$$|\tilde{\Psi}\rangle = \sum_i c_i^R\,|\tilde{\phi}_i^R\rangle \tag{3.19}$$

where c_i^R notes the expansion coefficients for the basis sets ϕ_i^R or $\tilde{\phi}_i^R$.
Because $|\phi_i^R\rangle = \hat{\mathcal{T}}\,|\tilde{\phi}_i^R\rangle$, both basis sets have identical expansion coefficients.

Since we require the operator $\hat{\mathcal{T}}$ to be linear, it is possible to find the projector functions $\langle p_i^R|$ which determine the expansion coefficients c_i^R.

$$c_i^R = \langle p_i^R|\tilde{\Psi}\rangle \tag{3.20}$$

Equation 3.19 implies that the projector functions $\langle p_i^R|$ must satisfy the completeness relation for all core regions

$$\sum_i |\tilde{\phi}_i^R\rangle\,\langle p_i^R| = \mathbf{1} \tag{3.21}$$

which implies that the projector functions are orthonormal to the basis set of the pseudo-wave function inside the core region. It means that

$$\langle p_{i_1}^R|\tilde{\phi}_{i_2}^R\rangle = \delta_{i_1,i_2} \tag{3.22}$$

Using equation 3.21, the operator $\hat{\mathcal{T}}_\mathrm{R}$ can be rewritten:

$$\hat{\mathcal{T}}_\mathrm{R} = \hat{\mathcal{T}}_\mathrm{R}\sum_i |\tilde{\phi}_i^R\rangle\,\langle p_i^R| = \sum_i \hat{\mathcal{T}}_\mathrm{R}\,|\tilde{\phi}_i^R\rangle\,\langle p_i^R| = \sum_i (|\phi_i^R\rangle - |\tilde{\phi}_i^R\rangle)\,\langle p_i^R| \tag{3.23}$$

Since the pseudo-wave function and the all-electron wave function are equal outside the core region, the operator $\hat{\mathcal{T}}$ can be written in the following way

$$\hat{\mathcal{T}} = \mathbf{1} + \sum_R \sum_i (|\phi_i^R\rangle - |\tilde{\phi}_i^R\rangle)\,\langle p_i^R| \tag{3.24}$$

There is also certain freedom how to define the projector functions (they must only satisfy equation 3.21) like in the case of the pseudopotentials. One of the possibilities how to define the projector functions giving the smooth pseudo-wave functions is to use the smooth Kohn-Sham potential v_s [25]:

$$|p_i^R\rangle = \left(-\frac{1}{2}\nabla^2 + v_s - \epsilon_i\right)\tilde{\phi}_i^R \tag{3.25}$$

The PAW method offers to calculate the observable properties of the all-electron system with the smoother pseudo-wave functions which are more convenient to calculate. Furthermore, the all-electron wave function is not lost and can be calculated from the pseudo-wave function using the projector functions. PAW also provides the way how to calculate the observables using the linear operator $\hat{\mathcal{T}}$. Any observable operator $\hat{\mathcal{O}}$ acting on the all-electron wave function $|\Psi\rangle$ can be transformed to the operator $\hat{\tilde{\mathcal{O}}}$ using the pseudo-wave function $|\tilde{\Psi}\rangle$:

$$\hat{\tilde{\mathcal{O}}} = \hat{\mathcal{T}}^\dagger\hat{\mathcal{O}}\hat{\mathcal{T}} \tag{3.26}$$

More details about the PAW method and the expressions for the individual operators can be found in [25, 26].

3.3. Vienna ab initio simulation package

Vienna Ab initio Simulation Package [27] (VASP) is a complex computer program developed by the research group of Georg Kresse from the *University of Vienna*. VASP uses various ways how to find the solution of the many-body Schrödinger equation, including Hartree-Fock approximation, Density Functional Theory (DFT) or the hybrid functionals. Many-electron methods like Green's function methods and perturbation theory is implemented as well [28].

VASP uses plane wave basis set to treat the valence electrons within the Vanderbilt's ultrasoft pseudopotentials or PAW method which allow an efficient reduction of the basis set. Optimization of the structural properties is implemented with the help of calculating forces and stress tensors. The electronic ground-state is calculated using the self-consistency cycle for which the efficient methods of matrix diagonalization (e.g. RMM-DISS [29] or blocked Davidson scheme [30]) are implemented.

3.3.1. VASP input and output files

VASP uses several files for the setup and the output of the calculations. This section gives a brief introduction to the input and output files which are used in VASP.

Input files

- *INCAR* file specifies what kind of calculation is made, which methods are used and also includes the corresponding parameters. These parameters can be for example related to the electronic or ionic relaxation settings, density of states (DOS) calculations or magnetic properties of the system.

- The *POTCAR* file contains the parameters of the pseudopotential and the exchange-correlation potential used in the Kohn-Sham equations. Since these parameters are transferable, there is a database of the pre-calculated *POTCAR* files for all common atoms from the periodic table of elements. If the calculated system contains more types of atoms, the *POTCAR* file consists of merged *POTCAR*s of the individual atoms. We can also find the basic properties inside this file describing the atom, e.g. atomic configuration or number of valence electrons.

- Geometry of the system – unit cell, atom types and the atom positions – is specified in the *POSCAR* file. We can choose between the *direct* notation of the atom positions which is defined as the linear combination of the vectors defining the unit cell, and the *cartesian* notation, which defines the coordinates for each atom, independently on the unit cell.

- The last file which must be defined at the beginning of every calculation is called *KPOINTS* file. This file specifies how is the first Brillouin zone sampled, using the k-point grid. There are several ways how to define the k-point grid. It is possible to either enter all k-points manually, to define the strings of k-points necessary for the band structure calculations, or automatically generated k-point meshes [31].

- There might be other input files which are necessary to run the specific method. For example *ICONST* or *PENALTYPOT* files are needed to be specified for the meta-dynamics calculations.

Output files

- The most important output file which contains the whole procedure of the calculation is called *OUTCAR*. The file contains the results of electronic and ionic relaxations, band energies, Fermi energy, k-point occupations, stress tensors, forces acting on ions and many other properties.

- The *CONTCAR* file contains the final structure after the calculation is finished. It is always provided in the direct coordinates.

- The calculated total charge density is stored in the *CHGCAR*. This file also contains the lattice vectors and the positions of atoms so it can be easily visualized. Furthermore, *CHGCAR* file can be used as the input file so the calculation starts from the predefined charge density.

- Information about the wave function can be found in the *WAVECAR* file. For the ionic relaxations, this file is generated only for the last step. As in the case of the *CHGCAR* file, *WAVECAR* can be also used to restart the calculation from the defined wave functions.

- Density of states (DOS) and the integrated DOS are specified in the *DOSCAR* file. It is also possible to calculate the projected density of states (PDOS) within the PAW method and the partial occupancies which are stored in this file as well.

- In the case of the ionic relaxation, *XDATCAR* file contains the structures of all ionic steps. This file is useful to visualize the relaxation processes or molecular dynamics simulations.

4. Methods for finding minimum energy paths

This chapter briefly introduces methods used to find the diffusion barriers of an oxygen vacancy in the perovskite structures which is one of the aims of this diploma thesis. Density functional theory can be used to estimate the energy of the system with the fixed positions of nuclei. We can therefore consider the Minimum Energy Path (MEP) which connects initial and final states of a reaction, passing the least energetically favorable point with the lowest possible energy on a Potential Energy Surface (PES). This configuration, called transition state, is a saddle point connecting the initial and final states. PES has the dimensionality equal to the number of degrees of freedom of the calculated system. For the system consisting of N atoms, the PES dimensionality is equal to $3(N-2)$[1]. It means that more complex systems have more degrees of freedom and it becomes harder to find a proper minimum energy path.

It is possible to overcome this barrier using a molecular dynamics simulation at elevated temperatures. However, due to the magnitude of the barrier, the transition would be a rare event, resulting in unfeasible simulation times. This method based on the spontaneous transition is not therefore usable in many cases because these simulations would take too much time. For this reason, more effective methods were developed where bias forces or potentials are introduced. These forces and potentials influence the system in order to scan the minimum energy path with a much lower computational effort.

4.1. Nudged elastic band method

Nudged elastic band method is one of the techniques used to find the transition paths from the initial to final positions. The method is based on a construction of intermediate images which are chained together with spring forces to ensure an equal spacing of the reaction path. These forces are defined to act along the chain, whereas the forces coming from the potential energy are projected to the perpendicular direction of the band so a relaxation is only allowed in the hyperplanes perpendicular to the path.

The great advantage of this method is an explicit mapping of the reaction pathway with a reasonable computational cost, depending on the number of evaluated images. In practice, we need to define the images connecting the initial and final state, which is possible with a linear interpolation of the atomic positions as it is shown in figure 4.1. However, this initial guess doesn't have to be optimal in all cases and we might end with the transition path which is not the minimal energy path. Another drawback of this method is the fact, that the transition state is not calculated directly. If the sufficient number of images is generated, this method provides a structure close to the saddle point, but if one needs to calculate the saddle point accurately, it is necessary to use variations on NEB, such as climbing NEB or another method. The other disadvantage is related to the temperature dependent simulations. Because the nudged elastic band method works at the 0 K temperature, one needs to use more advanced methods to estimate e.g. the temperature dependences of energy barriers. More comprehensive study concerning the nudged elastic band method can be found in [32].

[1] for all $N > 2$.

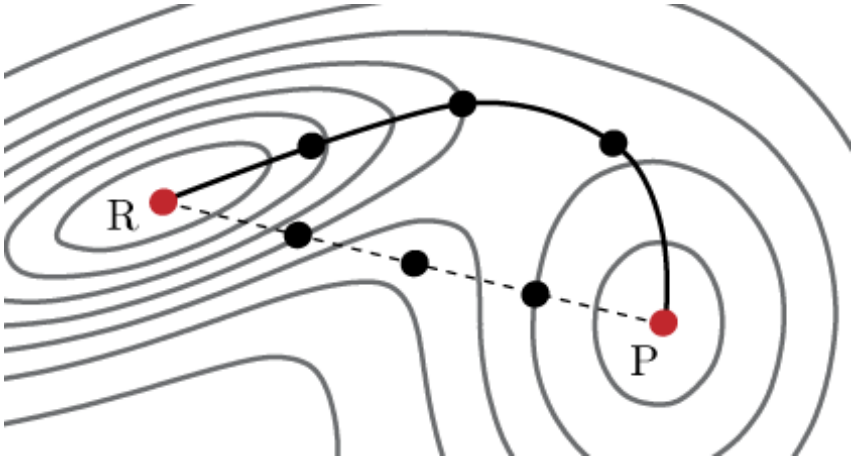

Figure 4.1: A scheme of the Nudged Elastic Band method. The dashed line notes the band connecting the initial and final state at the beginning of the calculation. Images composing the band are relaxed with help of projected forces coming from the spring binding of the images and potential energy of the landscape. The final band marked as the solid line is obtained by minimizing the total energy for each image which is biased by these forces. Image taken from [33].

4.2. Dimer method

Dimer method is a technique for finding saddle points on the potential energy surface. The main idea is to move a reactant in the direction of the softest vibrational mode. To find this direction, two auxiliary systems need to be created which are equally displaced from the actual position on the opposite sides along an axis, creating a dimer as it is shown in figure 4.2. The dimer is rotated around the middle point and we look for the lowest sum of total energies of the auxiliary systems composing the dimer. This procedure aligns the dimer along the softest unstable vibrational mode. As the last step, the energy is maximized in this direction, while all other perpendicular directions are minimized. It results into an introduction of an "Effective Force" which is a sum of the "True Force" acting on atoms in the system and the force acting along the lowest curvature direction, as it is shown in figure 4.2.

Because there are usually many saddle points in the potential energy landscape, it is necessary to define an initial dimer axis. The axis can be guessed or we can also overcome this problem by the vibrational analysis to find the proper direction for the first step of the dimer method. This method works better when we have an idea about the structure of the transition state so we are close to the saddle point on PES. For our purposes, the main advantage of this method is the possible combination with the nudged elastic band method discussed in the previous section.

A disadvantage of the dimer method is again connected with more complex systems. Unfortunately, there is no guarantee that this method finds the proper saddle point which might be a problem in more complex systems. More information about this method, e.g., how does the rotation of the dimer work with different algorithms, the process of translation of dimer, how to select the initial configurations and some practical examples can be found in [34].

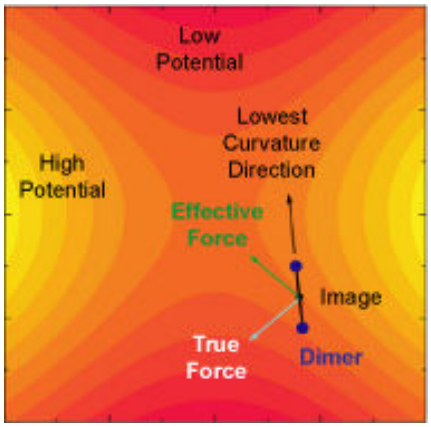

Figure 4.2: A scheme of a dimer method. A dimer is created from the image and it is aligned along the lowest curvature direction. The force acting on ions is biased by the force acting along the dimer axis, resulting to the effective force.

4.3. Metadynamics

The last method discussed in this chapter and used in the thesis is called metadynamics. Unlike the previous methods, this method calculates free energies which also includes the entropic contribution. In this method, the bias potential $\tilde{V}$ is introduced which acts on the geometrical parameters, e.g., distances between atoms, angles, torsions and its linear combinations, which are called collective variables. The bias potential is updated during the simulation with the Gaussian hills, usually after several ionic steps, according to this equation:

$$\tilde{V}(\xi) = h \sum_{i=1}^{N} e^{-\frac{(\xi-\xi_i)^2}{2w^2}} \tag{4.1}$$

where h and w are parameters provided by a user defining the Gaussian hill – height and width respectively. After several ionic steps, another Gaussian hill is added to the bias potential at the actual position of the collective variable ξ_i. The bias potential influences the Hamiltonian of the system in the following way:

$$\tilde{H} = H + \tilde{V} \tag{4.2}$$

where $\tilde{H}$ is the Hamiltonian for a metadynamics simulation and H notes the Hamiltonian for an original unbiased system. Once we define a collective variable, a bias potential starts to fill the low-energy regions which allows to overcome the barriers placed at the collective variable. Furthermore, it is possible (and often necessary) to perform temperature-dependent calculations by giving a kinetic energy to the atoms and investigate a temperature dependence of the barriers. When the calculations don't run under the 0 K temperature, this method provides a free energy barrier [35].

The calculation process is shown in figure 4.3. The collective variable is filled with the bias potential, until the whole valley is filled and the movement along the collective variable is diffusive. The free energy is then estimated from the sum of all Gaussian hills put to the system.

This method provides a way how to overcome the problems of NEB and dimer method, because we can introduce a temperature for these calculations and we scan the whole relevant part of the potential energy surface for the transition. A drawback is related to the computational cost of these simulations, because we usually need thousands of ionic steps to obtain relevant results.

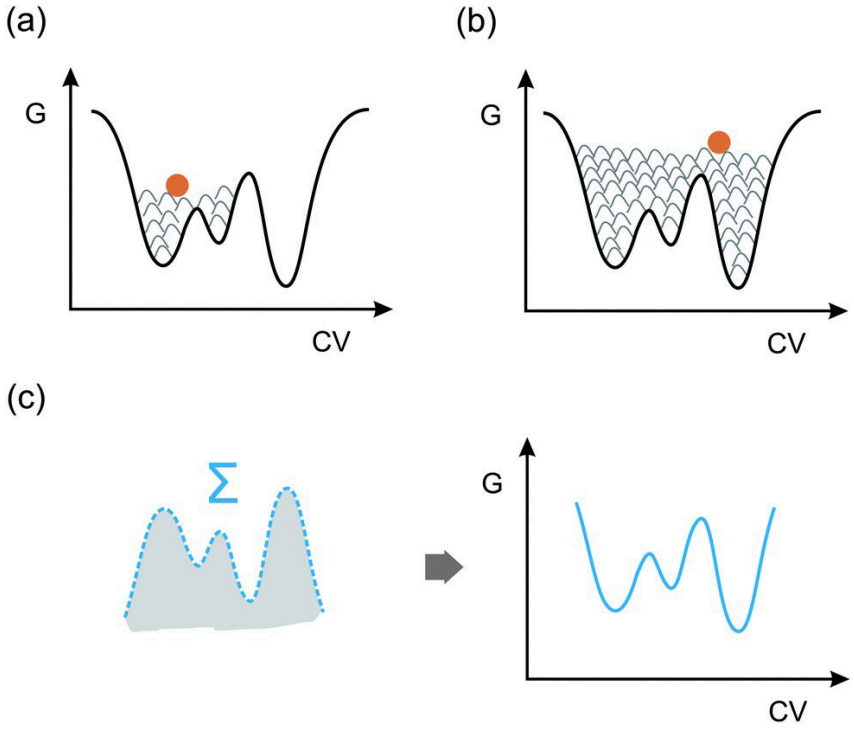

Figure 4.3: Computational procedure of a metadynamics simulation. Image taken from [35].

More comprehensive study concerning metadynamics method can be found in [36].

5. Lead zirconate titanate (PZT)

Lead zirconate titanate is a piezoelectric and ferroelectric ceramics material which consists of lead titanate ($PbTiO_3$) and lead zirconate($PbZrO_3$). It belongs to the perovskites group which has a general formula ABO_3, where "A" denotes the divalent cation[1] located at the corners of the unit cell, "B" is related to the tetravalent cation[2] placed in the middle of the unit cell, and "O_3" marks the oxygen atoms which are located in the center of the faces. The structure of the single compounds of the PZT ceramics is shown in figure 5.1.

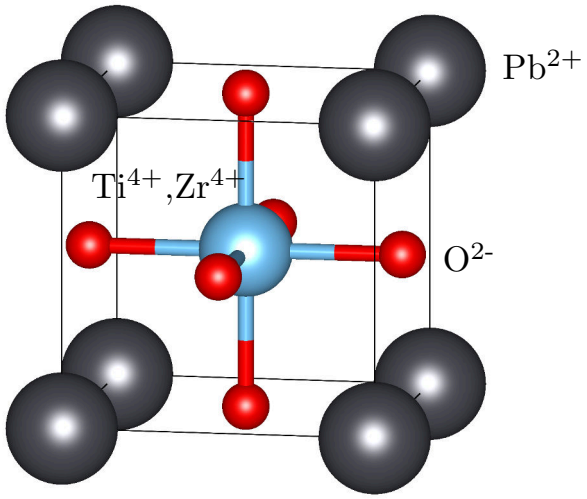

Figure 5.1: Structure of the cubic phases of $PbZrO_3$ and $PbTiO_3$.

The PZT ceramics can be formally written as $PbZr_{1-x}Ti_xO_3$ and can be considered as an alloy made of two compounds. Structural properties depend on a fraction of titanium (equal to x in the chemical formula) and temperature. As the phase diagram which was reported by Woodward et al. [37] in figure 5.2 shows, PZT exists in the rhombohedral phase for the high Zr:Ti ratio ($x < 46$) while the tetragonal phase is preferred in the titanium-rich alloys. The most important part of the phase diagram is the vertical line located at $x \sim 0.47$ which is called morphotropic phase boundary (MPB). It divides the region into the titanium-rich part with the antiferroelectric tetragonal phase with the space group symmetry *P4mm*. The region located on the left side where the concentration of zirconium dominates, is composed of the ferroelectric rhombohedral low-temperature and high-temperature phases with the space group symmetry *R3m* and *R3c*. The phase diagram also shows the temperature-dependent phase transition to the cubic phase which doesn't evince any ferroelectricity when the temperature exceeds the Curie point. These points form the highest line in the graph which goes from 230 °C for the lead titanate to 490 °C for the pure lead zirconate. The experiments show increased piezoelectric sensitivity near the morphotropic phase boundary. It was proposed that the increased piezoelectricity is observed due to the coexistence of both rhombohedral and tetragonal phases. In 1999, Noheda et al. explained this effect by the presence of the monoclinic phase [38] which was also reported in other experiments [39–41]. However, the measure-

[1] In our case Pb^{2+}

[2] Zr^{4+} or Ti^{4+} for the PZT ceramics

ments in [39] showed that the monoclinic phase is also present in the Zr-rich region and the real composition of the phase diagram is therefore still unsolved.

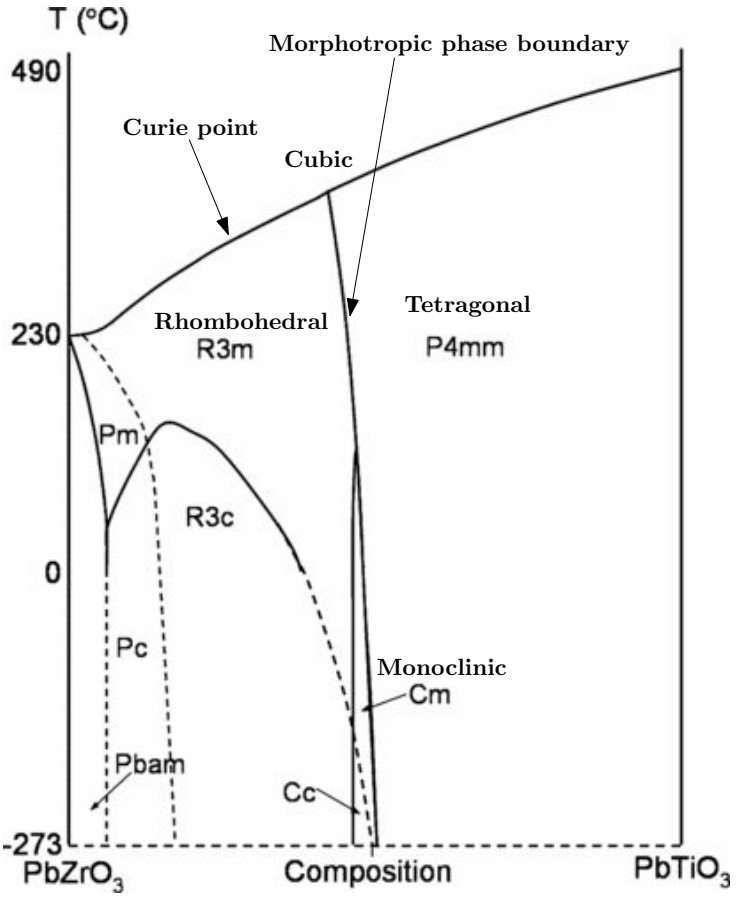

Figure 5.2: Phase diagram of the lead zirconate titanate alloy. Taken and rearranged from [37].

5.1. Applications

Ferroelectricity and piezoelectricity of the lead zirconate titanate can be employed in the number of applications and it is nowadays one of the most frequently studied piezoelectric material. Unfortunately, lead oxide, which is a part of this material, is very toxic and causes the pollution of an environment. Therefore lead-free piezoelectric materials like bismuth sodium titanate, potassium sodium niobate and bismuth potassium titanate are being recently studied [42]. However, because there is not still reasonable substitute for PZT, it is still being used in many applications.

Piezoelectric sensors are used to measure the stress changes by generating a charge output which is proportional to an applied stress. PZT ceramics has been successfully used for these purposes because of high piezoelectric coefficients near the morphotropic phase boundary [43]. Nevertheless, Dubois reported [44] that also other alloys which are not located at MPB are usable because of their high transverse piezoelectric coefficient. Figure 5.3 shows a simple scheme of a sensor. The structure of the sensor is equal to the capacitor, consisting of two metal plates and a piezoelectric material between them.

When an external pressure is applied, the sensor is deformed which invokes an excess of the surface charge which results in a voltage. Since the voltage is proportional to an applied stress, it is also possible to use the piezoelectric effect reversely in manipulators used e.g. in the Atomic Force Microscopy (AFM) cantilevers [45]. When the voltage is applied to the piezoelectric manipulator, the material is deformed due to the piezoelectricity. The goal of the manipulator is to repeat slow and fast displacements which cause the motion.

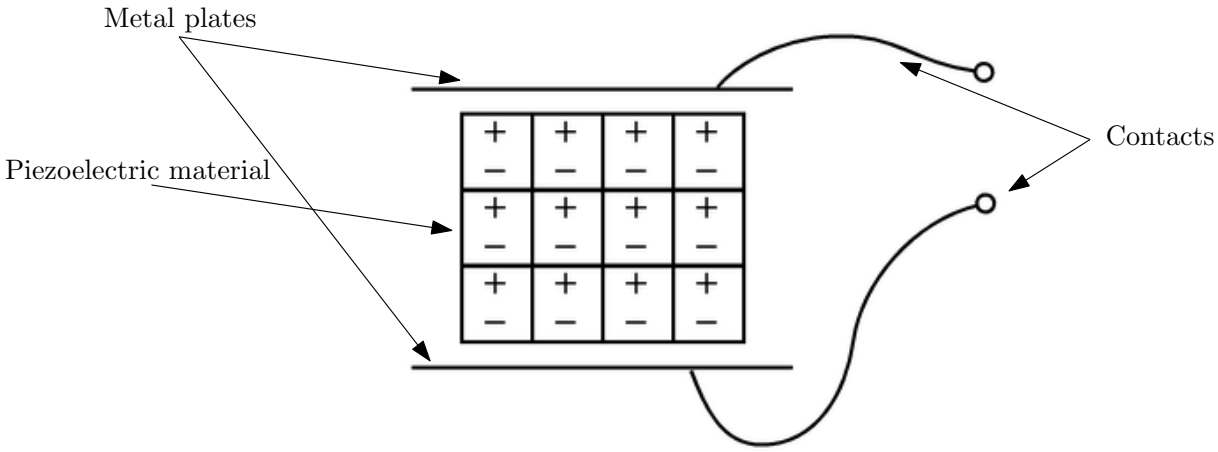

Figure 5.3: A scheme of the piezoelectric sensor.

Ferroelectric materials have two different electric polarization states which are stable even when the external electric field is absent. These states can be swapped by applying an external field which makes the PZT ceramics possible to use it in non-volatile ferroelectric random access memory applications [46]. With the help of these two different polarization states it is possible to store a binary information – logic 1 and logic 0. Unfortunately it was revealed that PZT suffers from the fatigue problem which is probably connected with trapping of oxygen vacancies at electrodes [47].

5.2. Effect of doping

Properties of the lead zirconate titanate can be tuned with a dopant which replaces an original ion in the structure. Doping of the PZT ceramics can be used to enhance the specific structural or electronic property which is crucial in real applications. For example, in the case of sensors or actuators, high dielectric constant and piezoelectric coefficient is required. Doping can be also used to suppress the fatigue problem occurred in non-volatile memories [48]. Considering the perovskite ABO_3 structure, both ions in"A" site or "B" site can be substituted. The preference is mainly dependent on the atomic radius of the doped atom. If the atom radius is small, the "B"-sites are rather occupied with a dopant, "A"-sites are preferred in the case of large atomic radius. The doping of the PZT ceramics can be divided on the "soft"-donor doping (e.g. Nb^{5+}, Sb^{5+}, La^{3+}, Fe^{2+}) and "hard"-acceptor doping (Fe^{3+}, Mn^{3+}) [49].

Effect of doping strongly influences formation of oxygen vacancies which have an important impact on functionality of the PZT. Recent experiments show unusual behavior of the ionic conductivity in doped PZT ceramics which is related to the ability of the

oxygen vacancies to diffuse through the material. The following subsections describe the experimental results [50] of the donor-doped and acceptor-doped lead zirconate titanate which is in focus of computational simulations presented in this work.

Soft doping

Formation of an oxygen vacancy is done by removal of an oxygen atom from the perovskite structure. The oxygen is in O^{2-} state and it is needed to balance the charge of two electrons by other atoms in the material to create an oxygen vacancy. In other way, we can consider the oxygen vacancy as a positive particle which can react with doped atoms. The "soft" doping is caused by an electron donor, e.g. La^{3+}, which replaces the lead atoms at "A"-sites. Replacement of a divalent lead by a trivalent lanthanum brings an extra electron which can react with the positively-charged oxygen vacancy according to the equation:

$$La^{2+} + \frac{1}{2}V_O^{2+} \Longleftrightarrow La^{3+} \tag{5.1}$$

According to this formula, oxygen vacancies are being trapped with the divalent lanthanum atom, which comes to the more stable, trivalent configuration. It means that donor-doping suppresses the formation of the oxygen vacancies in the bulk. However, the ionic conductivity is not completely suppressed, but it is only significant at the grain boundaries which is a defect-rich area. Image 5.4b shows the distribution of the ^{18}O tracer in the near-surface region. The areas with high concentrations of the ^{18}O tracer implies high diffusion of the oxygen vacancies. As it is shown in figure 5.5, the penetration of the oxygen tracer is suppressed in the case of lanthanum-doped samples which corresponds to the lower mobility of the oxygen vacancies. More information concerning the results for the soft-doped PZT can be found in the experimental paper [50].

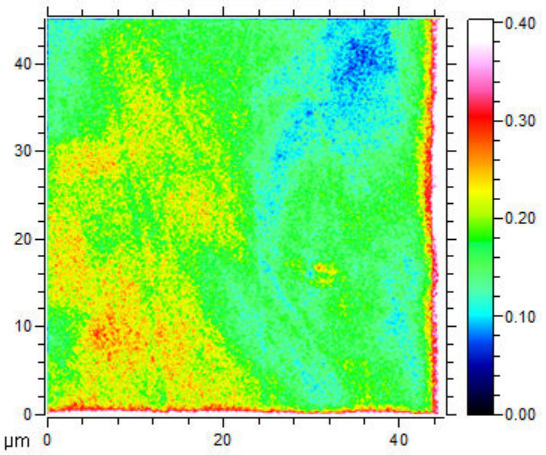

(a) ^{18}O tracer fraction of 0.5 % hard-Fe doped PZT. The oxygen vacancies diffuse through the whole material, the grain boundaries are not visible

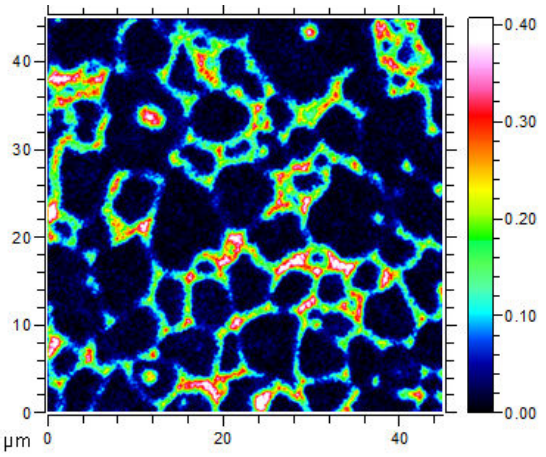

(b) ^{18}O tracer fraction of 0.5 % soft-La doped PZT. The diffusion of the oxygen vacancies is limited to the grain boundaries.

Figure 5.4: ^{18}O tracer fractions of differently doped PZT analyzed by Time of Flight Secondary Ion Mass Spectroscopy (ToF-SIMS). Images taken from [50].

Hard doping

In contrary to the soft-doped PZT, hard doping supports creation of the oxygen vacancy in the material. Unlike the soft doping, when a tetravalent Ti^{4+} is replaced with a trivalent Fe^{3+}, it forms half of an oxygen vacancy by trapping an electron from the oxygen and the oxygen vacancy is created according to the following formula:

$$Fe^{4+} \Longleftrightarrow Fe^{3+} + \frac{1}{2}V_O^{2+} \tag{5.2}$$

The acceptor-doped samples exhibit less sharp hysteresis loops and lower dielectric constants [50]. Mobility of the oxygen vacancies is also higher than in the donor-doped case which causes the accumulation near the film-electrode interfaces. Higher concentration of the oxygen vacancies causes higher ionic conductivity without indication of the fast grain boundary diffusion. Figures 5.4a and 5.4b show the main difference in the oxygen vacancy diffusion in acceptor-doped and donor-doped PZT. In the first case, the oxygen vacancy diffuse through the whole material, while in the donor-doped PZT, the diffusion is limited only to the grain boundary.

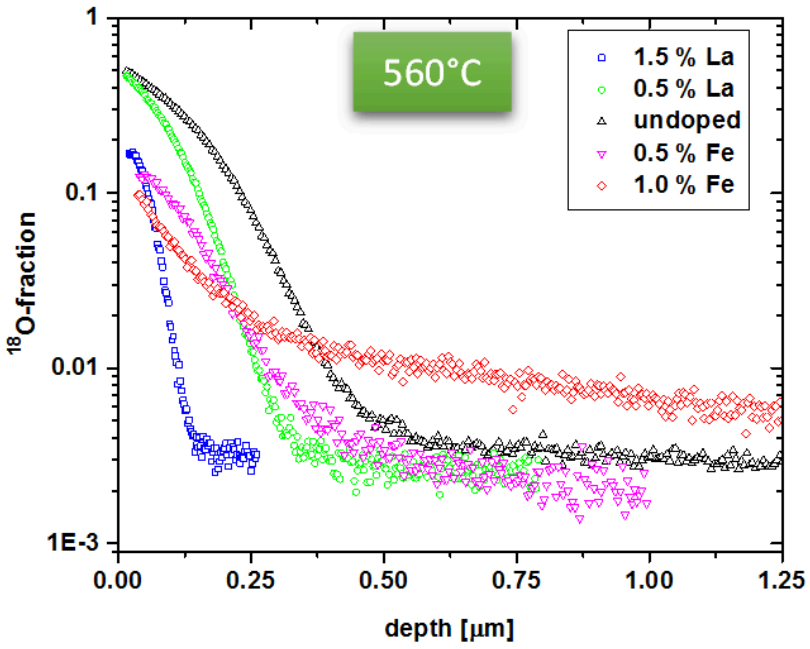

Figure 5.5: Depth profiles of donor-doped, undoped and acceptor-doped samples measured by Time of Flight Secondary Ion Mass Spectroscopy after 30 min tracer diffusion at 560 °C. Image taken from [50].

Figure 5.5 shows the logarithmic depth profile of five differently doped PZT samples. It is shown that the 1 % Fe-doped samples evince higher oxygen penetration than the undoped PZT ceramic. The rest of the samples have the smaller penetration depth which indicates that the oxygen vacancies are trapped even in the acceptor 0.5 % Fe case.

Diffusion of the oxygen vacancies is described by the diffusion coefficient D_V resulting from the Fick's laws of diffusion. The tracer diffusion coefficients D_b measured in the

experiments are related to the correlated motion of the mobile oxygen vacancies χ_V by [50]

$$D_b = f\chi_v D_v \tag{5.3}$$

where f is the correlation factor of the lattice. The diffusion coefficients are dependent on the temperature according to the Arrhenius equation

$$D_b = D_0 e^{-\frac{E_A}{RT}} \tag{5.4}$$

where E_A notes the activation energy and T temperature of the system.

The estimated diffusion coefficient for the oxygen vacancy is in terms of $10^{-12}\,\mathrm{cm^2 s^{-1}}$ according to [50] for a acceptor-doped case and the similar value is predicted in the earlier study for undoped case [51].

5.3. Trapping mechanisms of oxygen vacancies

This section summarizes the experimental results [50] concerning diffusion coefficients of the oxygen vacancies in both doped and undoped lead zirconate titanate. The resulting values of diffusion coefficients in the acceptor-doped PZT couldn't be explained by simple chemical considerations which sets up the motivation for the practical part of this thesis.

The first remarkable fact proceeds from the comparison of the relative differences between measured diffusion coefficients of the 1.5 % La-doped and 1 % Fe-doped PZT. The ratio between the diffusion coefficients in the donor-doped and acceptor-doped PZT was estimated to be ~ 371 for 560 °C and ~ 54 for 715 °C. However, the ratios are very small compared to the expectation values. Concentration of mobile oxygen vacancies in a similar Nd-donor doped PZT was estimated to 0.01 ppm range [52] which would result in 4 ppm concentration of mobile oxygen vacancies for the 1 % Fe-doped PZT. If all iron dopants were participated in the creation of the mobile oxygen vacancy, there would be the normalized vacancy concentration 1667 ppm with respect to the oxygen sites. Comparison of diffusion coefficients and activation energies in the $SrTiO_3$ perovskite [53] also indicates that concentration of the mobile oxygen vacancies in the lead zirconate titanate is in terms of 2 ppm. It was proposed that the unusually low diffusion coefficients for the acceptor doped PZT are caused by trapping of the oxygen vacancies and a trapping mechanism increases the activation energy in equation 5.4 which causes the oxygen vacancies to be immobile. To explain the trapping of oxygen vacancies, several mechanisms were proposed:

- The first mechanism known from the $SrTiO_3$ perovskite is based on the formation of the Fe^{4+} cations – the reverse process described by the equation 5.2. However, it was assumed that this cannot be the only relevant trapping mechanism because some experimental results, like temperature dependence of the hole conductivity couldn't be explained.

- Existence of the tetravalent Pb^{4+} instead of on the"A"-site in the perovskite structures was proposed in many works [54–56]. It was suggested and discussed in [50,51] that trapping of the oxygen vacancies can be caused by formation of a tetravalent lead.

There are some theoretical works dealing with structural, electronic and piezoelectric properties in the PZT or in pure compounds [57, 58], using GGA and hybrid functionals. Because there are not any published theoretical works estimating the activation energies of the oxygen vacancy motion in lead zirconate titanate, the aim of this diploma thesis is to use the density functional theory to investigate the trapping mechanisms from a theoretical point of view using the GGA and hybrid DFT approach to perform the calculations.

6. Application of DFT on lead perovskites

This chapter is focused on density functional theory calculations of electronic and structural properties of lead titanate ($PbTiO_3$) and lead zirconate ($PbZrO_3$). The aim of the presented work is to identify the diffusion energy barriers of oxygen vacancies inside the bulk material. Our aim is to explain the trapping mechanisms of oxygen vacancies which is still unclear. All structural and electronic calculations were performed in *Vienna ab-initio simulation package* (VASP) and the structural plots were exported using VESTA program [59].

Lead zirconate titanate is an alloy of two perovskite materials – lead zirconate and lead titanate. We will discuss the structural and electronic properties of the separate alloys and changes of these properties by presence of an oxygen vacancy. We will also present results of activation energies and energy barriers related to the diffusion of an oxygen vacancy in the lead titanate and lead zirconate perovskites.

DFT pre-calculations

First-principles (or ab-initio) methods don't generally need any empirical parameters for a calculation process. Nevertheless, these methods often solve problems numerically and it is necessary to define properly certain parameters related to the accuracy of the calculations to obtain reliable results. In all cases, it is needed to define properly at least two parameters which correspond to the convergence issue and which are dependent on the specific material, shape of the unit cell and the size of the cell. The first required parameter, k-points grid, is related to sampling of the Brillouin zone, according to the formula 3.11 where the sufficient number of k-points must be evaluated to describe the sampling correctly. The number of essential k-points also depends on the electronic properties of the system. For example, metallic materials generally require more k-points than insulators or semiconductors. A relevant grid is also dependent on the chosen smearing method and on the cut-off energy. Furthermore, even and odd uniform k-points grids can provide different results so it is necessary to reach the absolute convergence. For our purposes we chose Gamma-centered and Monkhorst-Pack schemes [31]. The convergence criterion for the k-points grid was established in the way that the absolute difference of the total energy per atom of the systems calculated with the converged grid and 12x12x12 Monkhorst-Pack grid was below 1 meV.

The second parameter corresponds to a size of thew plane-wave basis set which is needed to describe correctly valence electrons. Number of required plane waves depends on the chosen k-points grid, atoms inside the unit cell and also on the shape and volume of the cell. Size of the basis set is defined by the cut-off energy of plane waves that fulfill the inequation

$$\frac{\hbar^2}{2m_e}|\mathbf{K}+\mathbf{k}|^2 < E_{\text{cut}} \tag{6.1}$$

are considered. The left part of this equation is related to the kinetic energy of a free electron described by the wave vector $\mathbf{K}+\mathbf{k}$. Usual values of the energy cut-off are given in terms of hundreds of electronvolts. The chosen convergence criterion is similar to the

case of the k-points grid. We took the energy cut-off which results in the error of the total energy per atom lower than 1 meV. The reference cut-off energy was set to 1000 eV.

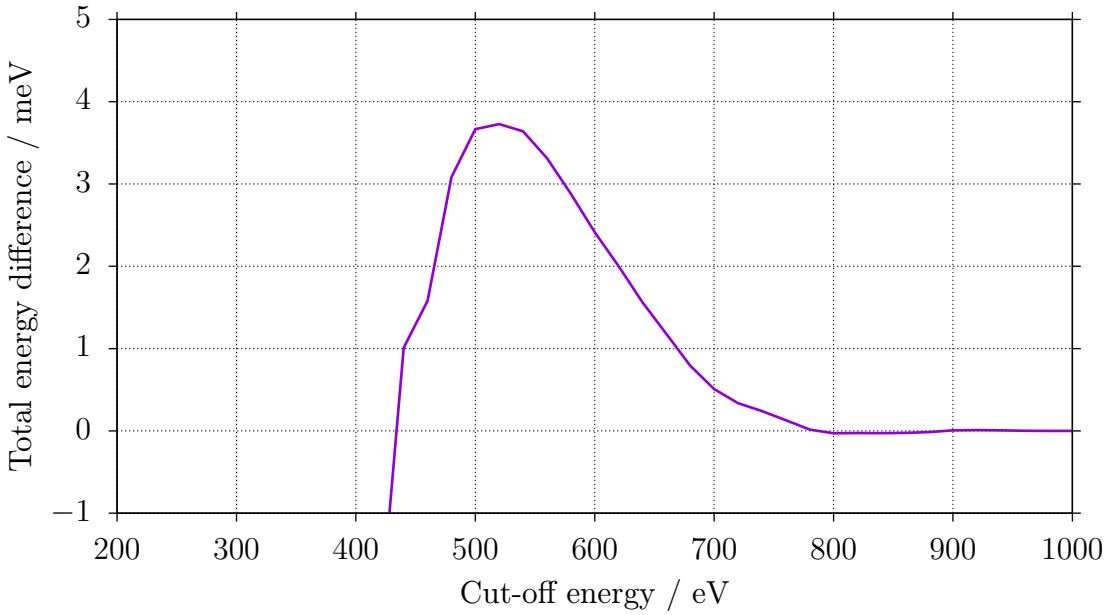

Figure 6.1: Convergence of the energy cut-off parameter using 5x5x5 Monkhorst-Pack k-points grid on the cubic lead zirconate. The 1 meV convergence criterion is reached for the cut-off energy equal to 700 eV.

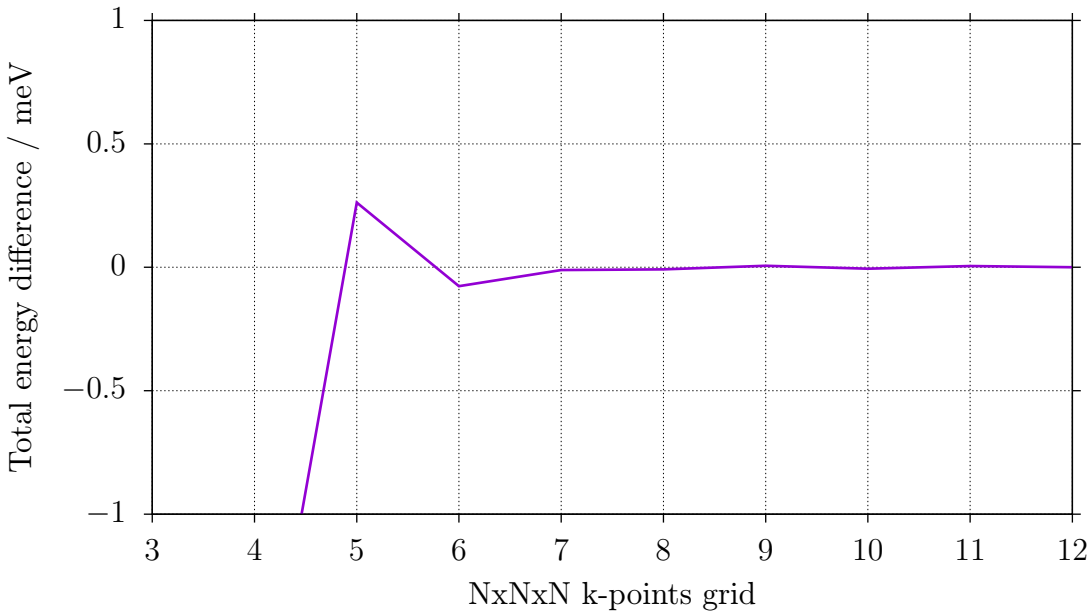

Figure 6.2: Convergence of the Monkhorst-Pack k-points grid using the 700 eV cut-off energy. The convergence criterion is reached for 5x5x5 k-points grid in the case of the cubic lead zirconate.

Cut-off energy and k-points grid are mutually dependent and it is necessary to reach both convergence criteria at the same time. With a change of one property must be also

checked the second property. Figures 6.1 and 6.2 show the convergence of the k-points grid and energy cut-off for the cubic lead zirconate unit cell. We can see that cut-off energy is converged at the same value as the k-points grid and vice versa.

DFT precalculations were also performed for the cubic lead titanate systems and we received the same energy cut-off and k-points grid as in the case of the lead zirconate.

6.1. Bulk properties of $PbZrO_3$ and $PbTiO_3$

Lead zirconate (PZ) is an antiferroelectric material which is employed in many applications like actuators, capacitors and charge storage devices [60]. The antiferroelectricity exists only in the orthorhombic phase which is stable up to 520 K [61]. When the lead zirconate is heated above this temperature, PZ becomes cubic.

Unlike the PZ, lead titanate is a ferroelectric material at the room temperature which stays tetragonal up to 760 K and then it is transformed to the cubic phase and the ferroelectricity disappears [62]. The ferroelectricity is caused by the displacement of the titanium atom from the center of the oxygen octahedra.

Phase		a [Å]	b [Å]	c [Å]	V [Å^3]
cPZ	PBE	4.19	4.19	4.19	73.56
	HSE	4.14	4.14	4.14	70.96
	Exp. [63]	4.16	4.16	4.16	72.06
oPZ	PBE	5.96	11.88	8.29	586.97
	HSE	5.85	11.83	8.22	568.87
	Exp. [64]	5.88	11.78	8.20	568.27
cPT	PBE	3.96	3.96	3.96	62.29
	HSE	3.92	3.92	3.92	60.24
	Exp. [65]	3.96	3.96	3.96	62.28
tPT	PBE	3.85	3.85	4.72	69.86
	HSE	3.87	3.87	4.24	63.50
	PBESol	3.90	3.90	4.08	62.06
	Exp. [66]	3.89	3.89	4.17	63.28

Table 6.1: Lattice parameters of the PZ and PT phases calculated with PBE, HSE and PBESol functional and compared with the experimental values.

This section is focused on the process of evaluating structural and electronic bulk properties of PZ and PT perovskites. The starting point of our calculations is the estimation of unit cells of all mentioned structures. The experimental data of the unit cells were taken as the starting configuration for calculations and we optimized them to its equilibrium state with respect to the volume of the cell, shape of the cell and internal coordinates of atoms. The energy cut-off was chosen according to the convergence calculations to 700 eV and we used 5x5x5 Monkhorst-Pack k-points grid. Electronic relaxations

were stopped when the energy differences between electronic steps were below 10^{-5} eV and ionic relaxation was stopped when all forces acting on ions were lower than 10^{-2} eV Å^{-1}.

Table 6.1 shows the bulk lattice parameters for the cubic and orthorhombic lead zirconate (cPZ, oPZ) and cubic and tetragonal lead titanate (cPT, tPT). Except the cPT phase, PBE overestimates the equilibrium volumes up to 3.6 % for the PZ phases. It is known from other perovskite structures that PBE tends to overestimate the volume of the cells [67]. It is also shown that PBE fails in describing the tetragonal lead titanate phase. The volume of the cell is increased by 10 % and c/a ratio which defines the tetragonal distortion is increased from 1,07 to 1,23. Because the results obtained by PBESol functional[1] are in much better agreement with the experimental data in the case of tetragonal lead titanate, we chose this functional for this phase for further calculations.

Figure 6.3 shows the calculated structures of all mentioned PT and PZ phases. The length of the unit cell vectors of the cubic lead zirconate shown in figure 6.3b is $\sim 1{,}06\times$ higher than for the cubic lead titanate. This increase of the length is expectable because zirconium atom has an extra d-shell filled with electrons compared to the titanium atom and has therefore a bigger atomic radius. Volumes of the tetragonal and cubic lead titanate unit cells are comparable. The main difference between these structures is a shift of titanium atoms upwards which gives rise to a dipole moment between the titanium and oxygen atom. The unit cell evinces a spontaneous polarization in direction of the shift of the titanium atom which causes this material to be ferroelectric. Zirconium atoms in the orthorhombic PZ are also displaced from the centers and all octahedra are alternately tilted to the right and to the left which causes opposite dipole moments and for this reason the material shows antiferroelectricity.

6.1.1. Electronic properties of the PZ and PT phases

An important quantity for investigation of the electronic properties is the density of states (DOS) which describes the number of states per energy interval. This property can be calculated using the equation 3.11 from the following formula:

$$\rho(E) = \frac{1}{N_k} \sum_{i,\mathbf{k}} \delta(\epsilon_{i,\mathbf{k}} - E) \tag{6.2}$$

where δ is a delta function which is equal to 1 for $\epsilon_{i,\mathbf{k}} - E = 0$, otherwise it is equal to 0. By plotting this energy we can obtain the important properties like a band gap value which defines whether the material is metallic, semiconductor or insulator. To estimate the localization of the states in atomic orbitals it is possible to monitor projected density of states (PDOS) which is calculated by inserting this complete orthonormal basis into the equation 6.2:

$$\rho(E) = \frac{1}{N_k} \sum_{i,\mathbf{k}} \sum_{\mu} \langle \psi_n | i_\mu \rangle \langle i_\mu | \psi_n \rangle \, \delta(\epsilon_{i,\mathbf{k}} - E) \tag{6.3}$$

where the orthonormal basis (like atomic orbitals) fulfill the condition $\sum_{\mu} |i_\mu\rangle \langle i_\mu| = \mathbf{1}$.

[1] PBESol functional also belongs to the GGA class and the computational cost is comparable with PBE.

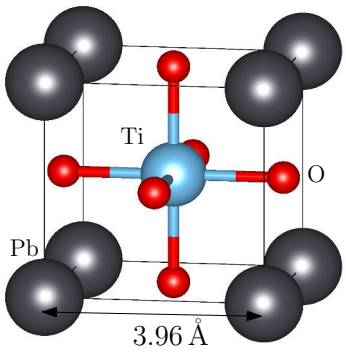

(a) Optimized cubic lead titanate structure with PBE functional.

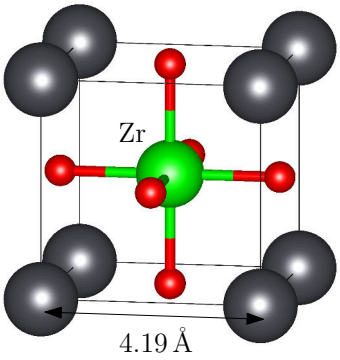

(b) Optimized cubic lead zirconate structure with PBE functional.

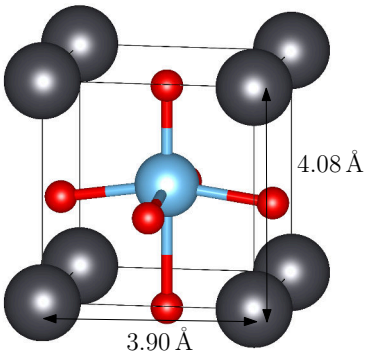

(c) Optimized tetragonal lead titanate structure with PBESol functional. The unit cell is prolongated in c direction and the titanium atom is shifted from the center of the oxygen octahedra.

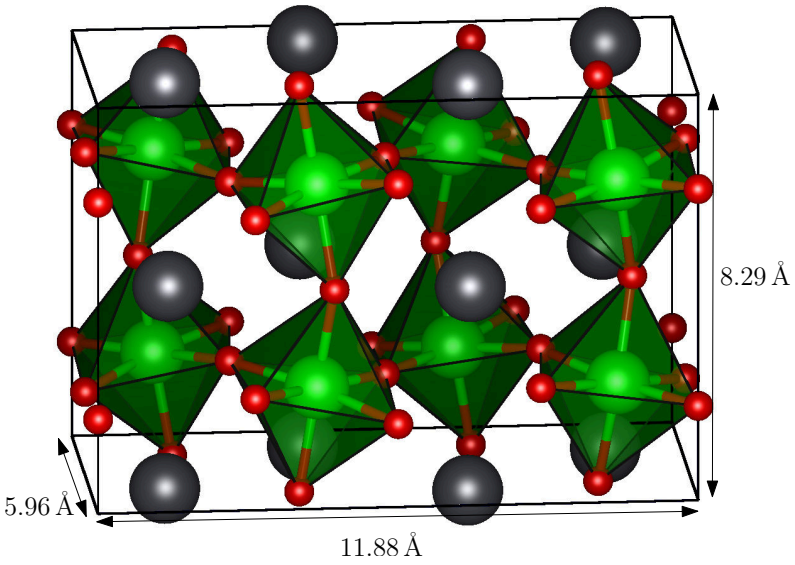

(d) Optimized structure of the orthorhombic lead zirconate. Oxygen octahedra are tilted in the material.

Figure 6.3: Structures of the calculated bulk phases of lead titanate and lead zirconate with PBE or PBESol functional.

Figures 6.4 show the plotted DOS and PDOS on the energy scale. Projected densities of states are taken with respect to the atomic orbitals localized at lead, titanium and zirconium atoms. Since the DFT calculations were performed at the 0 K temperature, the Fermi energy is equal to the energy of the highest occupied band. The Fermi energy in the graphs is set to zero so the states of the negative values of energy are related to valence and core bands, while the region of positive energies corresponds to a conduction band. The valence and conduction bands are split by the energy gap which can be experimentally measured. It turned out that the band gap values are not calculated correctly at GGA level [68]. Therefore we also performed hybrid HSE calculations which are in much better

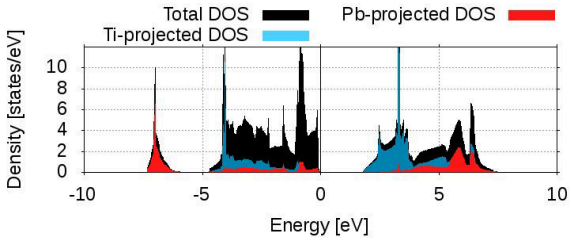

(a) Density of states for the cPT calculated with PBE functional. The band gap value is 1.83 eV.

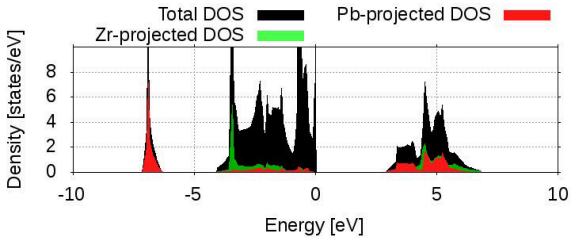

(b) Density of states for the cPZ calculated with PBE functional. The band gap value is 2.84 eV.

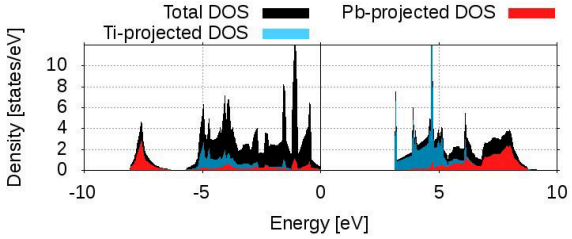

(c) Density of states for the cPT calculated with HSE functional. The band gap value is 3.19 eV.

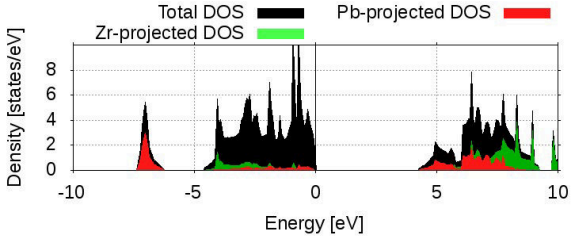

(d) Density of states of cPZ calculated with HSE functional. The band gap value is 4.29 eV.

Figure 6.4: Density of states of the cubic PT and PZ phases calculated with PBE and HSE functional.

agreement with the experimental band gap results of the titanate perovskites [69]. The density of states performed with HSE are calculated at the equilibrium lattice constant.

In all cases, the band gap is wider for the HSE functional and are in a better agreement with the experimental data which are shown in table 6.2. The PDOS show the important difference between cPZ and cPT plots in the conductive band. The states of the conductive band in cPT, which are shown in figures 6.4a and 6.4c, are localized mainly in the titanium atoms. On the other hand, PBE and HSE predict a localization of these states in the lead atoms for the cPZ as it is shown in figures 6.4b and 6.4d.

Phase	GGA	HSE	Exp.
cPT	1.83	3.19	3.4 [70]
cPZ	2.84	4.29	3.7 [70]
tPT	1.99	2.66	3.6 [71]
oPZ	2.80	5.00	4.3 [72]

Table 6.2: Comparison of experimental and calculated band gaps (in eV) at GGA and hybrid level. PBE functional was used for cPT, cPZ and oPZ phases, the band gap of the tPT phase was calculated with PBESol.

Figure 6.5 shows the plotted density of states and PDOS to the lead and tetravalent atom. By comparing images 6.5b with 6.5a or 6.5d and 6.5c we can see that the lead zirconate contains much more lead states in the conduction band as in the case of the

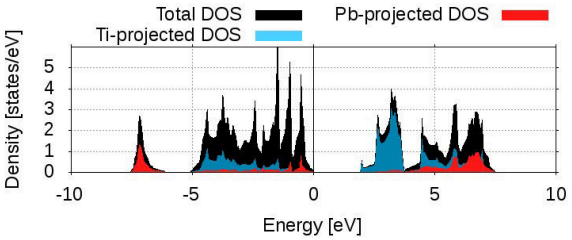

(a) Density of states for the tPT calculated with PBESol functional. The band gap value is 1.99 eV.

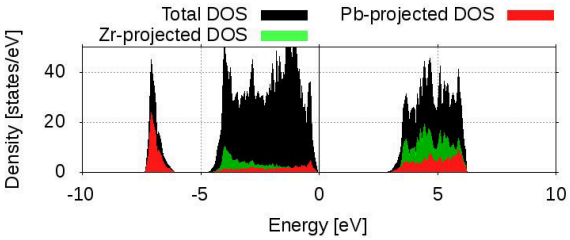

(b) Density of states for the oPZ calculated with PBE functional. The band gap value is 2.80 eV.

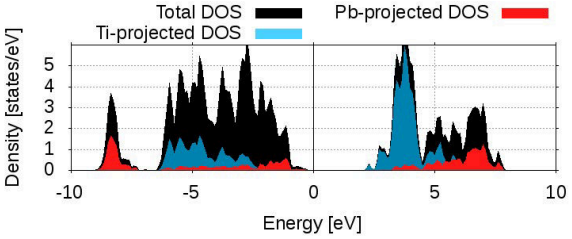

(c) Density of states for the tPT calculated with HSE functional. The band gap value is 2.66 eV.

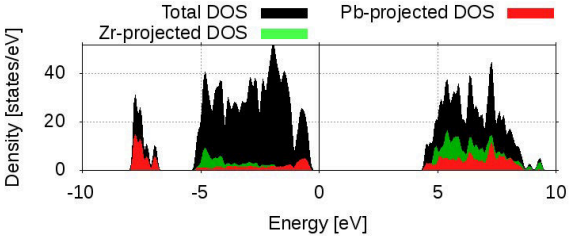

(d) Density of states of oPZ calculated with HSE functional. The band gap value is 5.00 eV.

Figure 6.5: Density of states of the tetragonal PT and orthorhombic PZ calculated with PBEsol/PBE and HSE functional.

cubic phase. The band gap of the orthorhombic phase is increased with respect to the cubic phase at PBE and HSE level. This is in agreement with observations in [72].

6.1.2. Formation of an oxygen vacancy

In real measurements of the ionic conductivity of PZT, concentration of oxygen vacancies is in terms of ppm. It is therefore necessary to build a supercell which is made of several unit cells to reflect this fact. Unfortunately we are only able to deal with concentrations around $\sim 1\,\%$ because of too large computational cost which is needed for calculations of larger supercells. An oxygen vacancy can be included to the system by removal one oxygen atom. Since we need to break the bonds of the oxygen, this process is described by a formation energy which defines how much energy is needed to form an oxygen vacancy. The formation energy can be thus calculated by the following equation with the energy of molecular oxygen as the reference.

$$E_{\text{form}} = E_{\text{Vac}} - NE_{\text{Bulk}} + \frac{1}{2}E_{\text{O}_2} \tag{6.4}$$

E_{Vac} is the total energy of the supercell with the oxygen vacancy, N notes number of unit cells which the supercell is made of and E_{Bulk} is the total energy of one unit cell of the same bulk phase.

When the structural changes are calculated, we can evaluate the influence of the oxygen vacancy on density of states as in the case of the bulk phases. The calculation procedure of the oxygen vacancy formation consists of introduction of the oxygen vacancy

by removal of one oxygen atom and relaxation of positions of ions inside the unit cell at the bulk lattice parameters.

We created 2x2x2 and 2x2x4 supercells containing 8 and 16 formula units[2] of all discussed phases. Because the calculated unit cell is bigger, the k-points grid can be reduced. According to the convergence tests, we chose 3x3x3 Monkhorst-Pack k-points grid for GGA calculations, which provided the total energy error 1.23 meV per atom. Calculation of the formation energies with the hybrid HSE were performed on 2x2x2 Gamma k-points grid with the total energy error equal to 3.7 meV per atom. Because the formation energies are in terms of electronvolts, the results are still reliable.

Phase	Functional	E_{bulk} [eV/f.u.]	$E_{\text{form,2x2x2}}$ [eV]	$E_{\text{form,2x2x4}}$ [eV]
cPZ	PBE	-39.19	4.83	3.92
	PBESol	-41.11	5.63	5.71
	HSE	-47.63	3.90	3.41
oPZ	PBE	-39.45	4.66	4.60
	PBESol	-41.38	5.84	5.28
	HSE	-48.17	5.61	7.04
cPT	PBE	-37.45	5.34	5.88
	PBESol	-39.36	5.21	4.77
	HSE	-45.92	3.35	3.47
tPT	PBESol	-39.42	5.44	5.41
	HSE	-46.01	3.61	3.02

Table 6.3: Bulk and formation energies for lead titanate and lead zirconate phases, considering 2x2x2 and 2x2x4 supercells.

Table 6.3 shows calculated bulk and formation energies of lead titanate and lead zirconate phases. E_{bulk} is the total energy of the ground state taken per formula unit. We can estimate the preference of the phases by comparing these energies with the corresponding functional. In the case of lead zirconate, all functionals predict that the orthorhombic phase is more stable than cubic phase. The total energy differences are in range from 270 meV/f.u. according to the PBESol to 540 meV/f.u. according to the HSE functional. The energetic order is in agreement with experiments because the antiferroelectric orthorhombic phase is more stable at low temperatures. Tetragonal lead titanate which is known from experiments at low temperatures, is more preferred according to PBE, PBESol and HSE functionals by 30, 60 and 90 meV/f.u., respectively.

Formation energies were calculated according to the equation 6.4. The energy of the supercells with an oxygen vacancy were calculated in different way for low temperature and high temperature phases. We observed significant octahedra distortions and dislocations of lead atoms for the cPZ and cPT phases. Therefore the positions of atoms whose distance was bigger than 5 Å were fixed. For most of the systems the formation energy is smaller in the bigger supercell which would mean that the vacancies are repulsive in the material.

[2]formula unit means the group of atoms which create the primitive cell. In our case one formula unit means $PbTiO_3$ or $PbZrO_3$ group.

Unfortunately the fixation of atoms can strongly influence the formation energies and the results for cubic phases are not thus reliable. There is a huge difference between the formation energies of orthorhombic lead zirconate calculated with HSE functional for different supercells. This can be an effect of strong localization of oxygen vacancies in the material which is a consequence of the non-symmetric rhombohedral unit cell. The charge localization can also depend on the functional. It is known that hybrid functionals tend to localize the electrons much stronger. To overcome this problem, one should build an orthorhombic supercell doubled in a and c direction, consisting of 32 formula units, which would lead to the computationally very demanding problem. Another aspect which we need to consider is the possibility that we obtained only the structure related to the local minimum. We can also see that the HSE results for other phases, where the oxygen vacancies are uniformly distributed, are $\sim 2\,\text{eV}$ lower than for the orthorhombic lead zirconate. According to the PBESol and HSE functionals, the formation energy of the tetragonal lead titanate is lower for the bigger supercells which corresponds with our expectations.

Electronic properties of the systems including oxygen vacancies

Density and projected density of states were calculated in the similar way as the bulk phases. We used 2x2x4 supercells containing 16 formula units with one oxygen vacancy. The low temperature phases were fully relaxed whereas the cPT and cPZ systems were partially optimized to keep the cubic structures and avoid octahedra distortions.

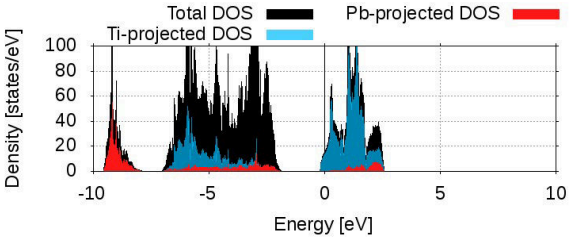

(a) Density of states for the cPT supercell with an oxygen vacancy calculated with PBE functional. The band gap value is 1.64 eV.

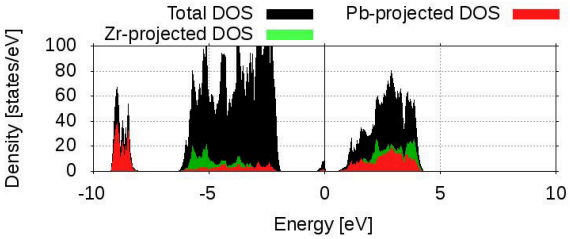

(b) Density of states for the cPZ supercell with an oxygen vacancy calculated with PBE functional. The band gap value is 2.42 eV.

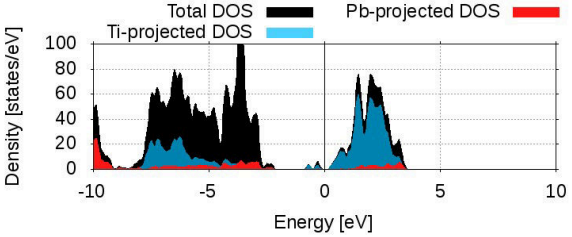

(c) Density of states for the cPT supercell with an oxygen vacancy calculated with HSE functional. The band gap value is 2.2 eV.

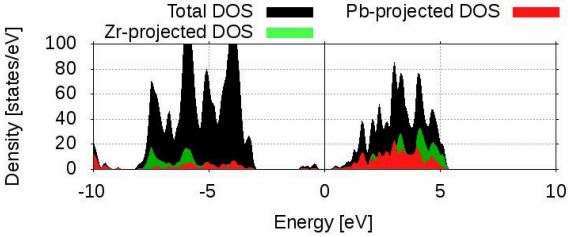

(d) Density of states of cPZ supercell with an oxygen vacancy calculated with HSE functional. The band gap value is 3.09 eV.

Figure 6.6: Influence of the oxygen vacancy on DOS and PDOS in the 2x2x4 cubic PT and PZ supercells calculated with PBE and HSE functional.

Removal of an oxygen atom from a supercell causes structural changes which have an effect on the resulting density of states. Furthermore, due to the oxygen bonds breaking, an extra states can be observed when the DOS are plotted. Depending on the localization of these states, the PDOS of Pb, Ti and Zr atoms can be also influenced. Figure 6.6 shows the DOS plots for the cubic phases. The first difference with respect to the bulk DOS is the presence of the "gap states" which come from creation of the oxygen vacancy. These gap states are clearly visible in HSE DOS plots as the dots in the middle of the band gap. In the case of cubic lead titanate PBE DOS, the gap states overlap the conduction band and the system is predicted to be metallic. The second difference with respect to bulk is the introduction of the gap states which are strongly localized in the titanium atoms in the case of the cubic lead titanate, while the gap states in the cubic lead zirconate phase are localized in the lead atoms. Figure 6.7 shows the charge distribution of the gap states in the unit cell which are localized in the vicinity of the oxygen vacancy. As we can see, the charge is strongly localized near the titanium atoms in the cubic lead titanate whereas in the cubic lead zirconate the gap states charge is localized in the lead plane.

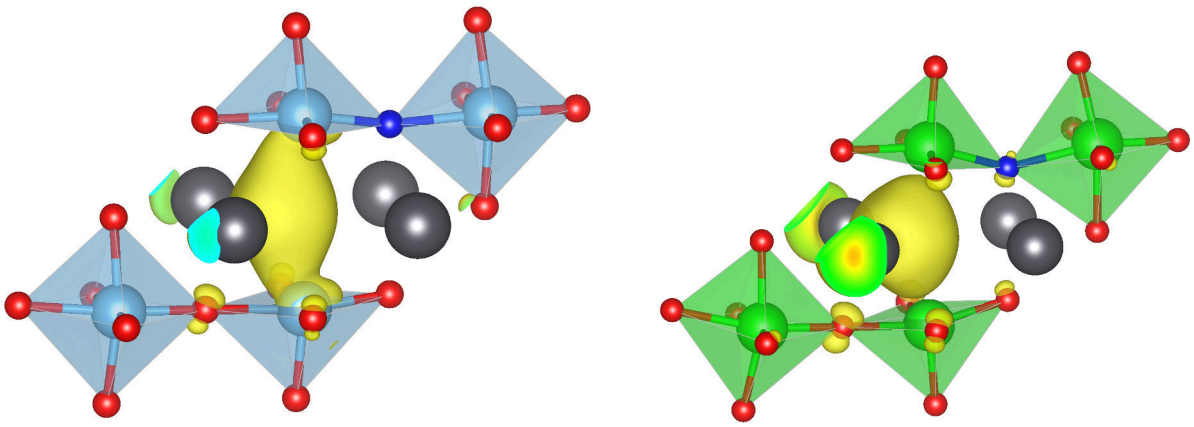

(a) Electronic charge density distribution of the gap states in the cubic lead titanate

(b) Electronic charge density distribution of the gap states in the cubic lead zirconate

Figure 6.7: Distribution of the charge related to the states which lay between the Fermi energy and 1 eV below. Blue oxygen atom is marked for the comparison with the transition states discussed later.

The plotted DOS graphs of the PBE functionals are very sharp while the HSE plots are much smoother. This is caused by different smearing method used to ensure the convergence of the calculations. PBE DOS plots are calculated with the tetrahedron method with Blöchl corrections [73] and for the HSE calculations we used gaussian smearing.

Figure 6.8 shows the plotted density of states for the orthogonal and tetragonal supercells. Many aspects are similar, but we can see the difference in the delocalization of the gap states which is caused by the broken symmetry. For example, the gap states for the tetragonal lead titanate calculated with HSE which are shown in figure 6.8c are made of two peaks, but only one of them is below the Fermi level. The HSE calculations of orthorhombic lead zirconate also show the splitting of the vacancy states located in the band gap.

Since the vacancy states are located in the band gap, we also present the comparison of the band gap values where the gap states in the middle of the band gap are omitted.

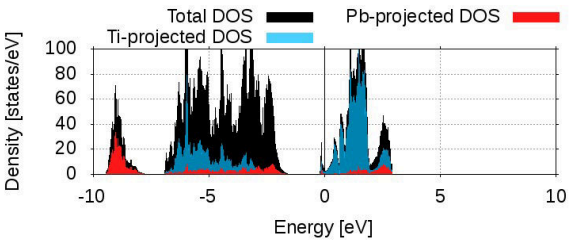

(a) Density of states for the tPT supercell with an oxygen vacancy calculated with PBE functional. The band gap value is 1.44 eV.

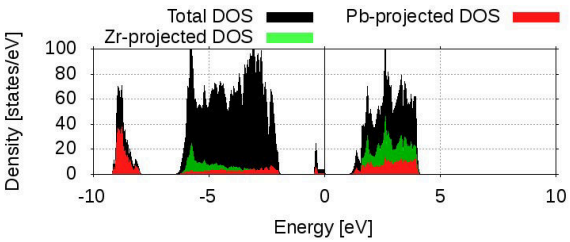

(b) Density of states for the oPZ supercell with an oxygen vacancy calculated with PBE functional. The band gap value is 2.89 eV.

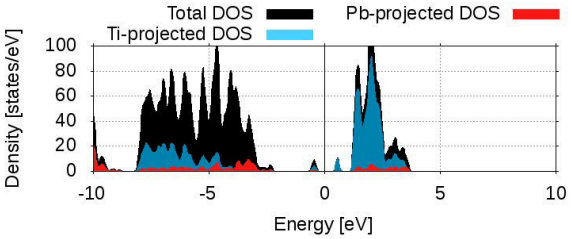

(c) Density of states for the tPT supercell with an oxygen vacancy calculated with HSE functional. The band gap value is 3.19 eV.

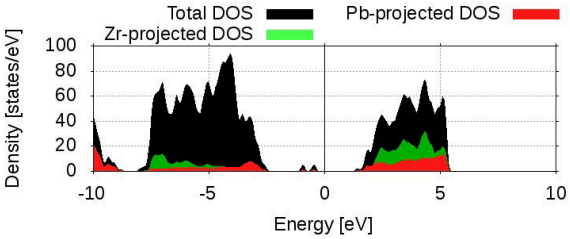

(d) Density of states of oPZ supercell with an oxygen vacancy calculated with HSE functional. The band gap value is 3.35 eV.

Figure 6.8: Influence of the oxygen vacancy on DOS and PDOS in the 2x2x2 tetragonal PT and 1x1x2 orthorhombic PZ supercells calculated with PBE, PBESol and HSE functional.

Comparing the results with the table 6.2, we can see that the gap states also influence the edges of the valence or conductive band. The increased value of the band gap in the tetragonal lead titanate by HSE functional is caused by the shift of the conductive band edge to the gap state so the band gap is higher. In other cases, the band gaps are comparable or lower than for the bulk phase. It means that the gap states are not only localized in the middle of the band gap but they also influence the valence and conduction band.

Phase	GGA	HSE
cPT	1.64	2.2
cPZ	2.42	3.09
tPT	1.44	3.19
oPZ	2.89	3.35

Table 6.4: Calculated band gaps (in eV) for the supercells with an oxygen vacancy at GGA and hybrid level. PBE functional was used for cPT, cPZ and oPZ phases, the band gap of the tPT phase was calculated with PBESol. The gap states were omitted.

6.2. Diffusion of the oxygen vacancy

This section describes the calculation process of energy barriers of the oxygen vacancy transport in the lead titanate and lead zirconate perovskites and several aspects will be examined to find out their influence on the barriers. Since the behavior of the vacancy states arising from the oxygen vacancy formation is different in the PZ and PT systems, the phase dependence on the energy barriers will be discussed. The influence of the oxygen vacancy concentration on the activation barriers is investigated by varying the size of the supercell. The last property which is studied in this chapter is the dependence of the energy barriers on the reaction path.

Computational setup

We investigated energy barriers of the oxygen vacancies in the supercells containing 8 and 16 formula units. In all cases, we used Gamma or Monkhorst-Pack 3x3x3 k-points grids which result in error lower than 1.23 meV per atom. Calculation of energy barriers required more computational effort, therefore the energy cut-off was reduced to 440 eV which resulted in the maximal total energy error 4 meV per atom. A motion of oxygen vacancies was specified using two different reaction paths which are shown in figure 6.9.

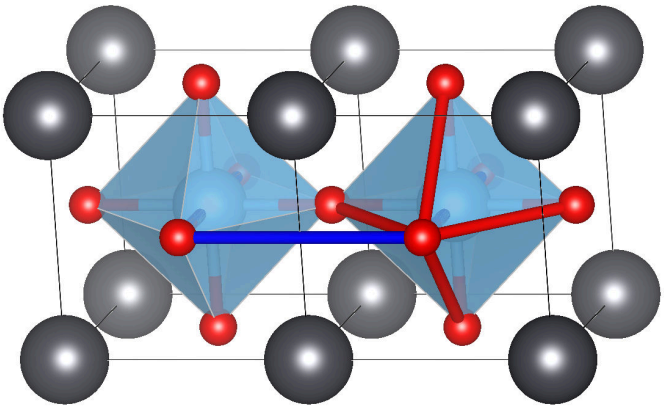

Figure 6.9: Studied reaction paths of the oxygen vacancy motion. Blue line marks a long path where the oxygen vacancy travels across two octahedra through the lead plane. Shorter red reaction path is related to the motion of the oxygen vacancy along a titanium octahedra.

In the first step, initial and final structures were created by removal of an oxygen at the beginning and at the end of a reaction path. Positions of ions in the unit cell were fully relaxed to obtain ground states for the initial and final systems containing an oxygen vacancy. These systems were taken as the ending points of the reaction path in the nudged elastic band method [74] (NEB). Figure 6.10 shows the optimized ground states with the oxygen vacancy. The blue oxygen moves along the titanium octahedra to the right which causes that the oxygen vacancy moves reversely with respect to the motion of the oxygen. In the next step, we generated the images between the initial and final positions by linear interpolation. Nudged elastic band method constrains these systems

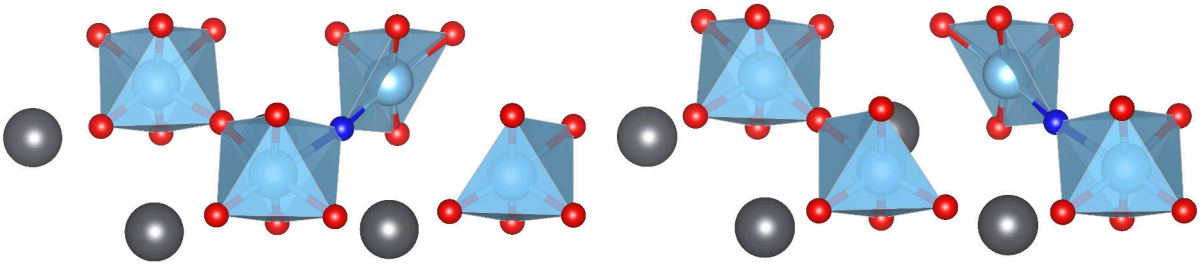

(a) Initial structure for the investigation of a reaction path with nudged elastic band method.

(b) Final structure for the investigation of a reaction path with nudged elastic band method.

Figure 6.10: Optimized initial and final states used of the cubic lead titanate system. The blue oxygen marks the moving atom from the initial to the final position.

by adding spring forces between the neighboring images along the band. All images are optimized with respect to their total energy which is biased by the potential coming from the forces between the bands. Figure 6.11 shows the linearly interpolated images from the initial to the final state. The difficulty of these calculations comes from the optimization of all structures at the same time.

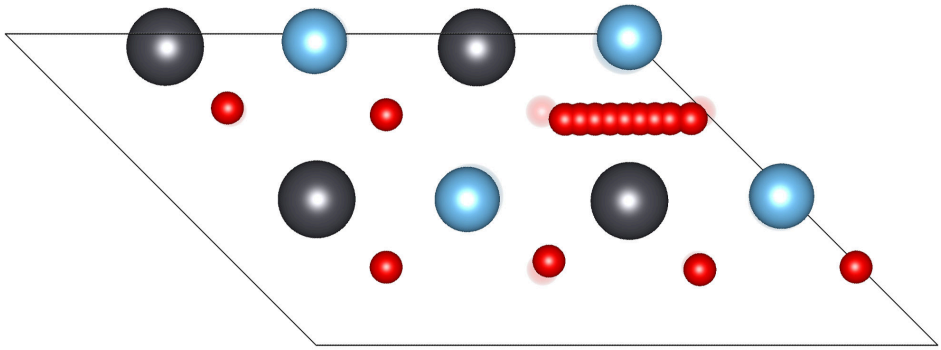

Figure 6.11: Linear interpolation of the initial and final state in the cubic lead zirconate supercell. The linear interpolation is shown only for the moved oxygen.

Nudged elastic band method is implemented in the VASP code. It is only necessary to create interpolated images and to define the spring constant which determines the force between the images. According to the size of the supercell, we used 4 or 8 interpolated images and the spring constant was set to -5 which is a default value. For the relaxation of ions, the quasi-Newton algorithm was used which turned out as the most stable option.

Figure 6.12 shows the resulting reaction path using the nudged elastic band method. The initial state is located at the zero on the x-axis, while the final state which is marked as the last point lies at 9. The intermediate steps are related to the NEB images and the interpolated line between these points shows the energy barrier for the oxygen vacancy. The height of the barrier is calculated only from the interpolation of the images which is going to be improved in the last step.

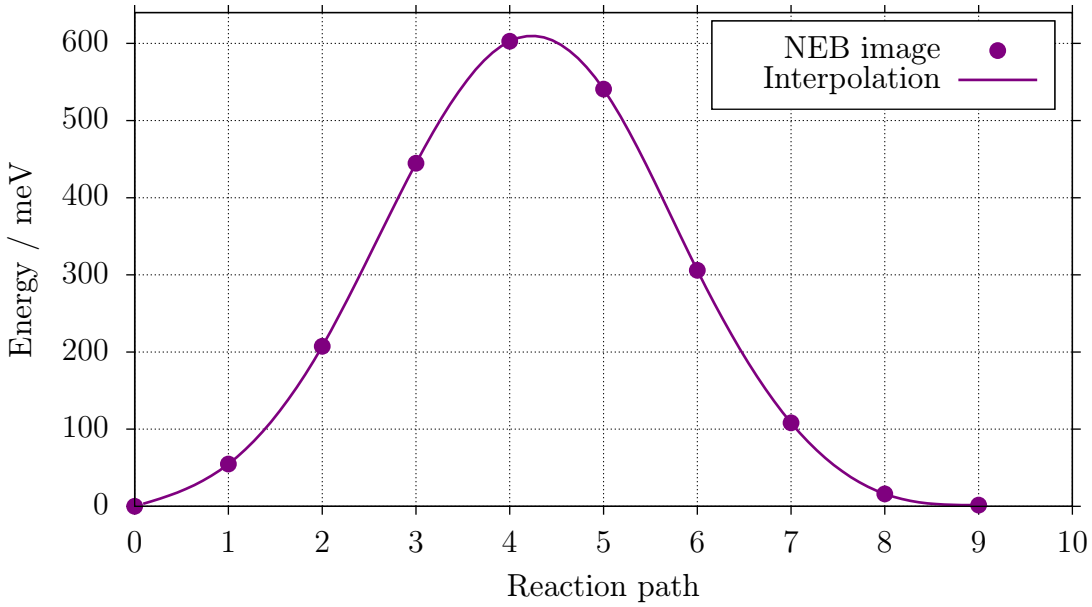

Figure 6.12: Energy barrier of the cubic lead titanate obtained by nudged elastic band method. The reaction path defines the transition between the initial and final states which are placed at 0 and 9 respectively. The reaction path was scanned using 8 images between the initial and final states.

The transition state was optimized using the dimer method [34], which requires the initial guess of the transition state and the initial velocities for each atom which define the starting direction to the transition state at the potential energy surface. We took the image from the NEB optimization with the highest energy as the initial guess for the transition state. Initial ion velocities were proportional to differences between positions of the initial guess and the image on the other side of the interpolated barrier. In the case of the cubic lead titanate, the image 4 from the figure 6.12 was taken as the initial guess of the transition state and image 5 was taken to define the initial velocities. Unfortunately, this method often failed in finding the proper transition state, especially in the bigger supercells which have more degrees of freedom. For this reason, we also calculated the energy barriers using the tangential forces acting on the moved oxygen atom.

To calculate the energy barriers from the tangential forces, we took the forces acting on the moved oxygen atom which are written in the OUTCAR file when the calculation was done. The force acting on the oxygen atom is considered as the negative gradient of the total energy. Therefore, the reaction barrier is interpolated from the total energy of the images and the forces with respect to the position of the oxygen. Since we consider the total energy and its derivative in two points on the reaction path, there are more ways how to interpolate the energy barrier. In this work we used linear and cubic spline interpolation.

Reaction path is visualized in figure 6.13. The violet atoms are related to the oxygen positions of the NEB images, the blue one comes from the transition state calculated with a dimer method. The neighboring red oxygens are placed at the initial and final positions.

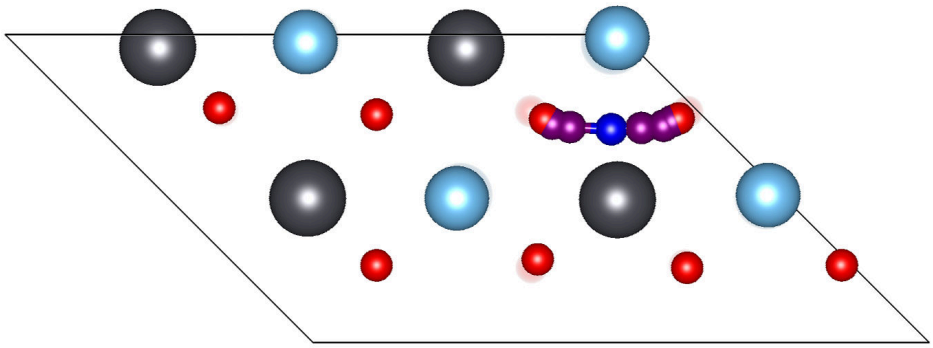

Figure 6.13: Visualization of the reaction path of the oxygen atom.

6.2.1. Dependence of the reaction path on barriers

We studied the reaction paths along and cross the octahedra as it is shown in figure 6.9 to investigate the basic mechanism how the oxygen vacancies diffuse in the material. According to all obtained data, the energy barriers are much higher for the long reaction path.

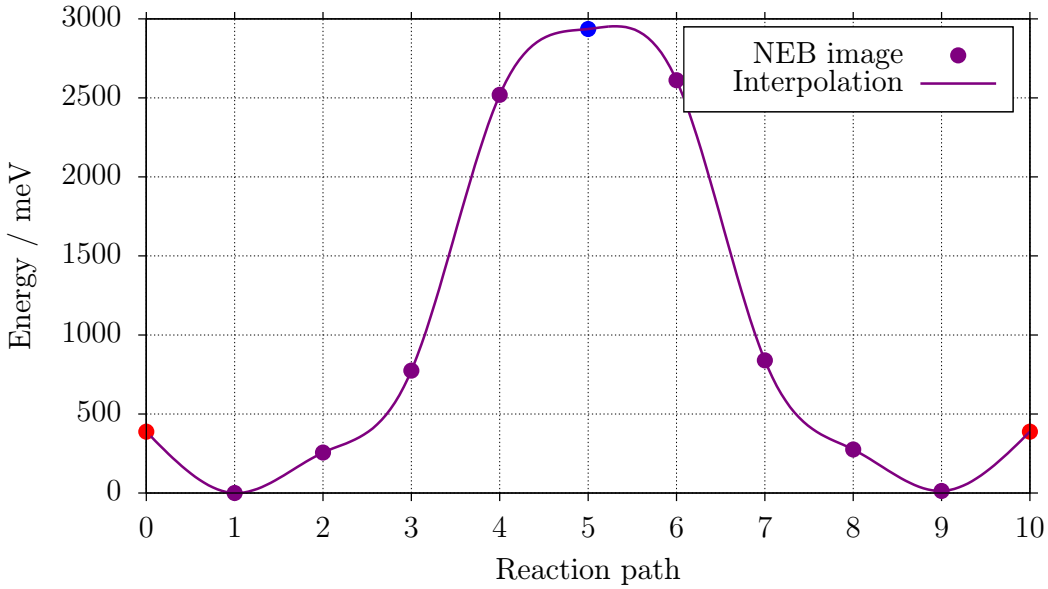

Figure 6.14: Energy barrier of the motion of the oxygen vacancy across an oxygen octahedra in the 2x2x2 cubic lead zirconate interpolated by cubic splines. The activation energy obtained by dimer method (the blue dot) is equal to 2936 meV. Red dots mark initial and final states. The blue dot is the transition state calculated with dimer method.

Figure 6.14 shows the energy barrier for the long path (across an oxygen octahedra) in the cubic lead zirconate 2x2x2 supercell, interpolated by cubic splines between the energies of the NEB images. The obtained activation energy is comparable with the

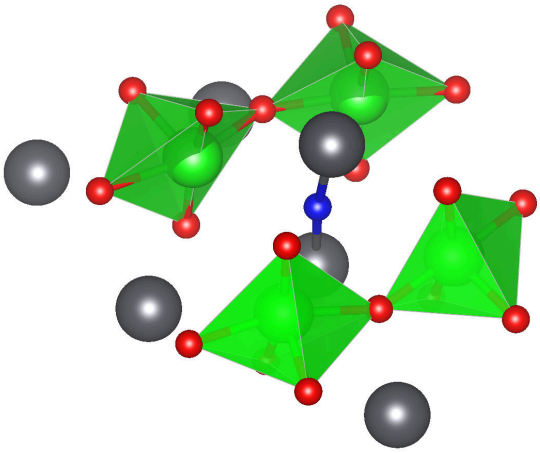

Figure 6.15: Transition state for the long path. The oxygen crosses the lead plane very close to the lead atoms, at the distance 2.24 Å. All neighboring octahedra are broken.

barriers related to the long paths in the lead titanate supercell. In the case of short paths, all energy barriers were at least 500 meV lower compared to the long paths, depending on the chosen phase. For example, the energy difference between the long and short paths for the cubic lead zirconate phase is 1454 meV which can be seen from figures 6.14 and 6.16. We assume that it is caused by breaking the bond between a moving oxygen and a tetravalent metal. Furthermore, the oxygen-lead distances are small – only 2.24 Å for the lead zirconate as it is shown in figure 6.15. According to the obtained energy barriers for the long and the short paths we assume that long paths are not preferred and the diffusion process is done only along the oxygen octahedra.

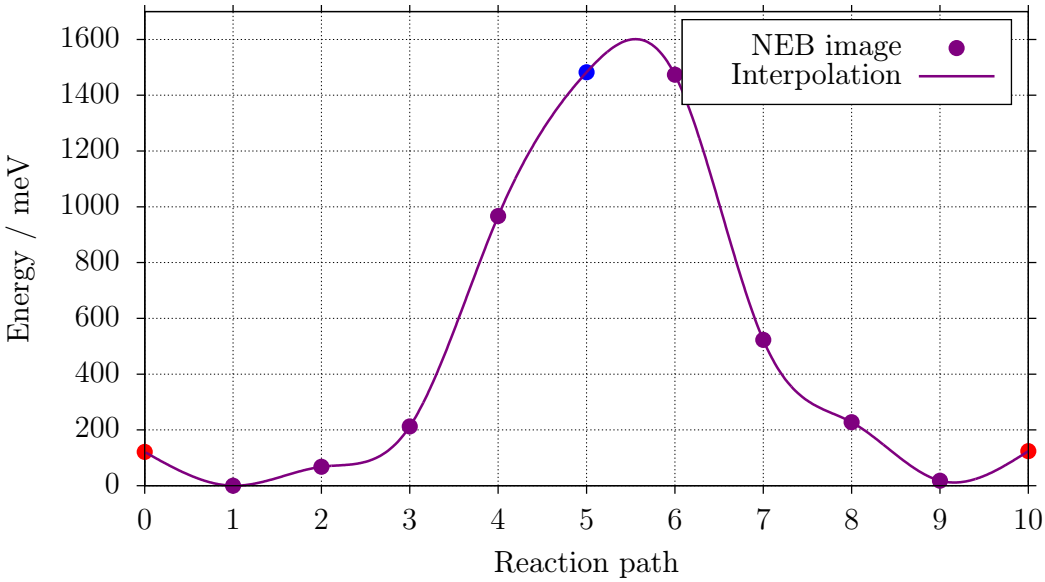

Figure 6.16: Energy barrier of the motion of the oxygen vacancy across an oxygen octahedra in the 2x2x4 cubic lead zirconate interpolated by cubic splines. The activation energy obtained by dimer method (the blue dot) is calculated to be 1482 meV. Red dots mark initial and final states.

6.2.2. Lead zirconate vs. lead titanate

A phase dependence was investigated with the same procedure. Even when titanium and zirconium atoms have the same electronic structure of valence electrons, we observed a difference in the vacancy states and different representation of lead states in conduction bands of PT and PZ phases. We also observed a strong influence of the activation energy by the tetravalent atom (titanium or zirconium).

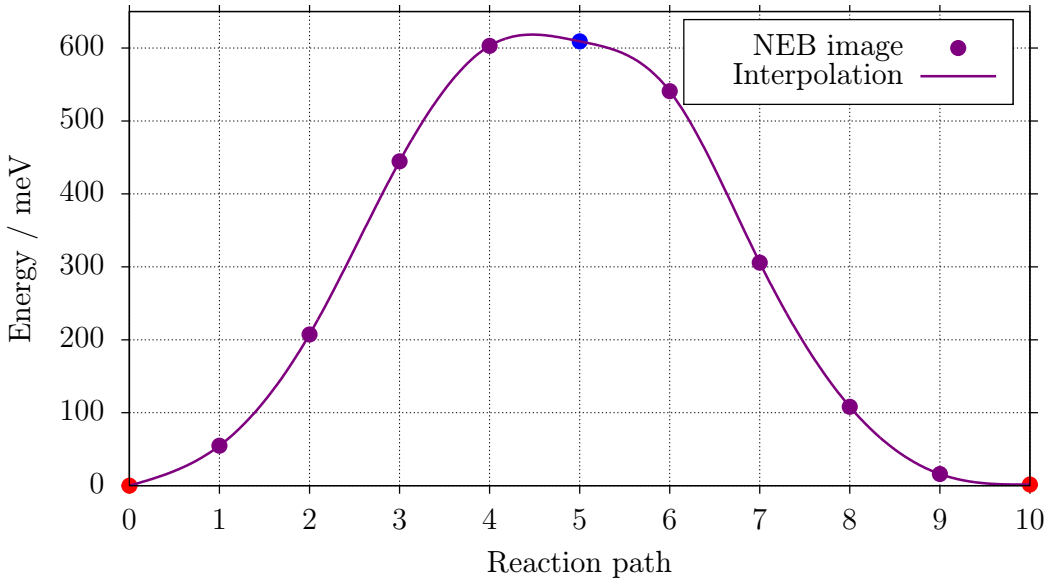

Figure 6.17: Energy barrier of the motion of the oxygen vacancy across an oxygen octahedra in the 2x2x2 cubic lead titanate interpolated by cubic splines. The activation energy obtained by dimer method (the blue dot) is calculated to be 609 meV. Red dots mark initial and final states.

Figure 6.17 shows the reaction barrier for the 2x2x2 cubic lead titanate. However, we observed large orthorhombic-like oxygen octahedra distortions and the shifts of lead atoms in the cubic zirconate supercell, most probably because of the large energy difference between the orthorhombic and cubic phases. NEB reaction path for the cubic lead zirconate is partly shown in figure 6.18. No transition state was found using the dimer method, but the NEB image with the highest total energy is located 1502 meV above the ground state which is $\sim$ 2,5$\times$ higher value than the activation energy obtained for the lead titanate systems. Moreover, we obtained similar values of the activation energy for the orthorhombic unit cell. Even when we observed large distortions in the material, a reaction path of the moving oxygen was similar to the lead titanate reaction path, which is shown in figure 6.13.

To take a close look on this surprising difference, we estimated the ground state and the transition state from the cubic lead titanate structures where we didn't observe the distortions. We expanded the lattice vectors by 1.058 which is related to the ratio between the cPZ and cPT lattice vectors, replaced titanium atoms to zirconium and we optimized the structures with the quasi-Newton algorithm, which minimizes the forces acting on ions and is also worth to use it to find the transition states if we have the sufficient initial structural guess. Using this approach, we obtained the transition state where the moving

oxygen atom is located in the middle of the path which indicates that the structure of the transition state is calculated correctly. Furthermore, the energy difference between the transition state and ground state obtained from the cPT structures is 1640 meV which is in agreement with the NEB path and also with activation energies calculated for the orthorhombic lead zirconate.

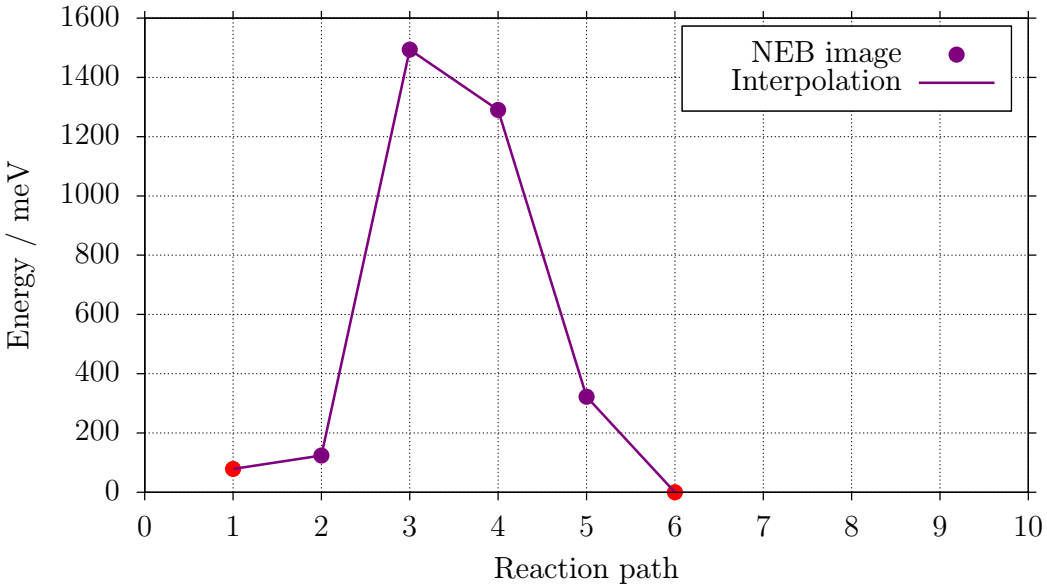

Figure 6.18: Energy barrier of the motion of the oxygen vacancy across an oxygen octahedra in the 2x2x2 cubic lead zirconate. Red dots mark initial and final states.

Figure 6.19 shows the difference in DOS between the transition states of cPT and cPZ structures. The difference is comparable with the DOS plots for the cubic phases in figure 6.6a and 6.6b where the localization of vacancy states follow the same rule – these states are strongly localized in titanium atoms for the cubic lead titanate phase and in lead atoms in the case of lead zirconate.

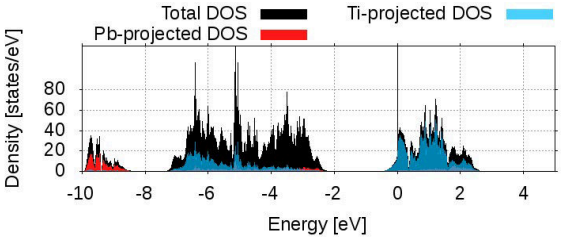

(a) Density of states of the transition state of the 2x2x2 cubic lead titanate supercell. The structure was calculated with dimer method.

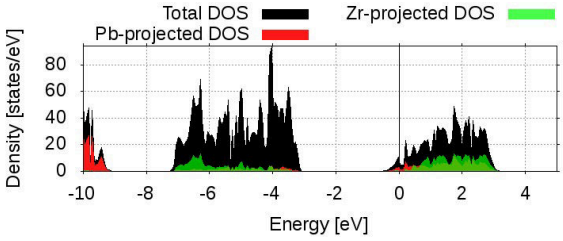

(b) Density of states calculated for the transition state of the 2x2x2 cubic lead zirconate supercell. The structure was derived from the transition state of the cubic lead titanate.

Figure 6.19: Comparison of DOS calculated for transition states of cubic lead zirconate and cubic lead titanate supercells.

The structure and distribution of the charge density related to the vacancy states is shown in figure 6.20. The main structural difference is the prolongation of the bond connecting the tetravalent metal and the blue moving oxygen from 1.82 Å to 1.96 Å. The electronic charge density distribution of the vacancy states for lead zirconate and lead titanate systems is comparable with the ground states and it is shown in figure 6.20. The states are localized only in the titanium atoms, whereas in the case of lead zirconate, the vacancy states are rather localized in the lead atom.

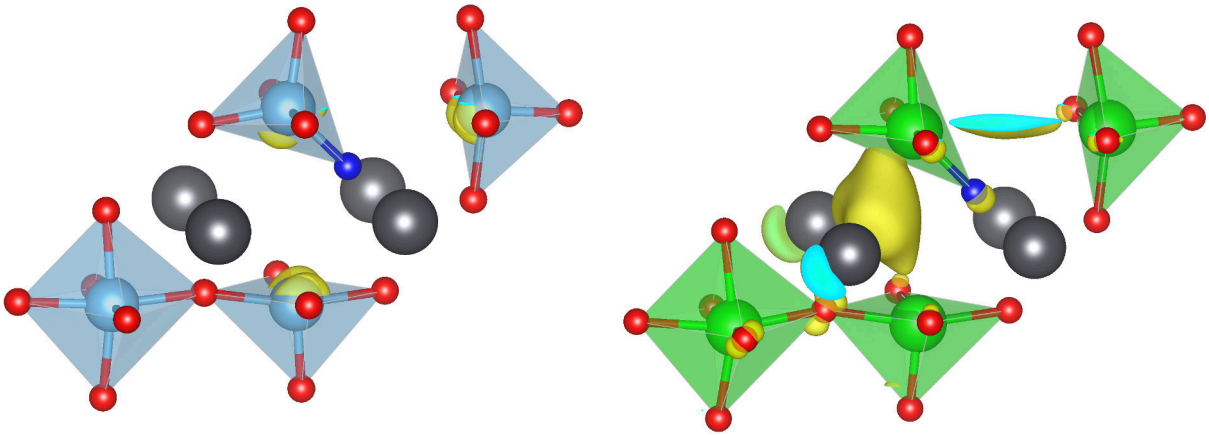

(a) Structure and electronic charge density distribution of the gap states in the cubic lead titanate transition state

(b) Structure and electronic charge density distribution of the gap states in the cubic lead zirconate transition state

Figure 6.20: Distribution of the charge density related to the states which lay between the Fermi energy and 1 eV below, calculated for the transition states of the cPT and cPZ supercells. The position of the blue oxygen atom which is moving from the initial to the final position is located in the middle of the path in both cases.

We assume that the difference between the energy barriers comes from the different localization of the vacancy states which are more significantly changed in the case of the lead zirconate – the most of charge density has to be moved from the lead plane to another one. While the vacancy states in the lead titanate are localized near titanium atoms and the change of the charge distribution is not so radical.

6.2.3. Summary and influence of other aspects on barriers

In the previous subsections we discussed the major effects which influence the activation energy of the oxygen vacancies diffusion in lead zirconate and lead titanate. Here we also present a complete overview of our results concerning various conditions and discussion of other effects for which we didn't observe any significant influence. Tables 6.5 and 6.6 show obtained activation energies for lead titanate and lead zirconate respectively. We calculated the activation energies by looking for the proper transition state by dimer method and we compare them with the interpolated values by linear and cubic spline interpolation. The interpolated activation energies are almost in all cases in a very good agreement with the dimer method, especially when the NEB images are close to the transition state. If there are too large forces acting on a moving oxygen or the positions of

this oxygen are too different in these images, this approximation doesn't work sufficiently, as, for example, in the case of a long path in cPZ 2x2x4 supercell.

Lead titanate

Supercell	Phase	Path type	Functional	E_A [meV]		
				dimer	spline	linear
2x2x2	cubic	short	PBE	610	606	606
2x2x4	cubic	long	PBE	2965	2987	3069
2x2x4	cubic	short	PBE	(425)	406	414
2x2x2	cubic	short	PBESol	650	605	620
2x2x2	tetra	short	PBESol	(963)	986	971
2x2x2	tetra	long	PBESol	(3625)	3605	3800
2x2x4	tetra	long	PBESol	–	3219	3467

Table 6.5: Summary of activation energies calculated for lead titanate. We considered different supercells, phases, path types and GGA functionals. Activation energy E_A was calculated by subtracting the total energies of transition systems obtained by dimer method and ground state systems. Furthermore, we calculated the activation energies from the cubic spline and linear interpolation using the NEB images closest to the transition state. Some transition states weren't found under the required accuracy and these numbers are therefore shown in parenthesis.

Lead zirconate

Supercell	Phase	Path type	Functional	E_A [meV]		
				dimer	spline	linear
2x2x2	cubic	long	PBE	(2936)	2895	3219
2x2x2[3]	cubic	short	PBE	–	1779	2150
2x2x4	cubic	long	PBE	2746	2152	2583
2x2x4	cubic	short	PBE	(1482)	1484	1485
1x1x1	ortho	short	PBE	1770	1675	1739
1x1x2	ortho	long	PBE	(2292)	2069	2087
1x1x2	ortho	short	PBE	–	1691	1689

Table 6.6: Summary of activation energies calculated for lead zirconate. We considered different supercells, phases and path types. Activation energy E_A was calculated by subtracting the total energies of transition systems obtained by dimer method and ground state systems. Furthermore, we calculated the activation energies from the cubic spline and linear interpolation using the NEB images closest to the transition state. Some transition states weren't found with the required accuracy and these numbers are therefore shown in parenthesis.

Supercell dependence

The activation energy decreases by $\sim$ 200 meV except for oPZ short path where the activation energy between bigger and smaller supercell is comparable. The result is in agreement with our expectations because the size of the supercell modulates the concentration of oxygen vacancies in material. We can consider the oxygen vacancies as the positively charged objects which repel each other and this effect is more significant in the smaller supercells because of the periodic boundary conditions.

Functional dependence

Table 6.5 doesn't show a significant dependency of the chosen GGA functional on activation energy for the cubic lead titanate and the short path. All results for tetragonal phases are also comparable with obtained values from the cubic cell. There is a 350 meV difference between the short paths which can be caused by the oxygen octahedra distortions so these paths are not equivalent anymore. This can be also connected with a phase dependence. The functional dependency should be also checked for the hybrid HSE functional, but these calculations would be much more time-demanding and are beyond the scope of this work.

Phase dependence

Considering the PBE functional, we can only compare the results from the lead zirconate phase because the description of tetragonal lead titanate was insufficient. When the symmetry is broken, the short paths can be differently favorable. In this work we checked the vacancy migration through the longest side of the orthorhombic lead zirconate. As figure 6.21 shows, the highest energy of the image is comparable in all cases and the values are placed in a 50 meV energy interval.

We only calculated one energy barrier for the cubic lead titanate by PBESol functional and we would need more data to make a proper conclusion. Nevertheless, concerning the short paths, the 300 meV energy difference between the cubic and tetragonal phase can be caused by the wrong choice of the path. The second effect which might influence the energy barrier is the ferroelectricity of the lead titanate. However, to determine this influence wouldn't be straightforward and it is beyond the scope of this work.

6.3. Outlook: metadynamics simulations

There is no guarantee that the dimer method finds the proper transition state. Mainly in bigger supercells where we need to consider more degrees of freedom, to find a proper saddle point between two ground states might be a very difficult problem. Furthermore, we are still limited to the 0 K temperature and it is not therefore possible to calculate for example the temperature dependence of the activation energy. To overcome this facts, we have to go beyond the nudged elastic band method and one of the possibilities is to set up a metadynamics simulation. Because these calculations are very time-demanding

[3] We took the NEB image with the lowest energy as the reference for a ground state because of the orthorhombic-like octahedra distortions. Energy barrier was estimated to 1640 meV by modifying the lead titanate ground state and transition structures.

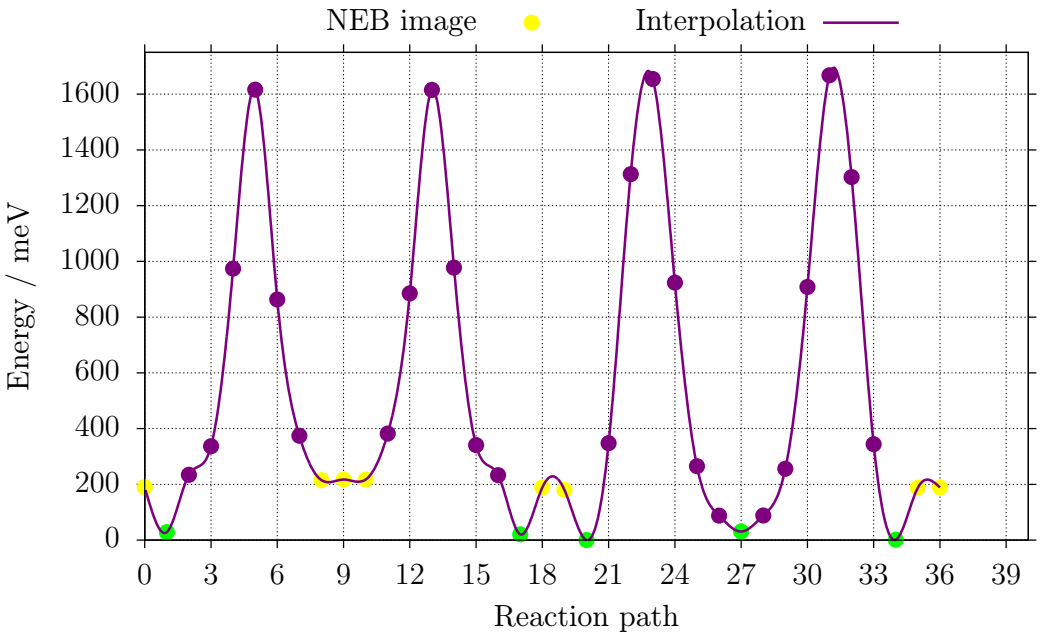

Figure 6.21: Energy barrier of the motion of the oxygen vacancy along different short paths in the orthorhombic lead zirconate. The green dots mark the ground states and the yellow ones meta-stable states.

and beyond the scope of this diploma thesis, we only present the preliminary results as an outlook for a subsequent work.

We studied a migration of oxygen vacancies along the short path in cubic 2x2x2 lead zirconate and lead titanate systems which are the most relevant for our aims. We used 440 eV cut-off energy which is converged to the total energy error 4 meV per atom. For the preliminary calculations we chose gamma-only k-points grid which results in very high, 127 meV per atom total energy error. We set the temperature to 700 K and applied a Nosé-Hoover thermostat with Nosé-mass equal to 0.3. The biased collective variable was defined as the difference between the distances of the moving oxygen and the oxygens which are placed along the motion. Figure 6.22 shows the oxygen bonds which define the collective variable. In principle, it would be possible to define the collective variable as the distance d_2. However, in the case of high-temperature calculations, it is recommended to determine the collective variable using more atoms to fix the motion of oxygen better along the vacancy path.

The bias potential was put into the system every 15 ionic steps in terms of Gaussian hills with the height of 10 meV and width 0.02 Å. In summary, we performed 10^5 ionic steps for lead titanate and 2×10^5 ionic steps for lead zirconate to scan the collective variable.

Unlike the NEB method, metadynamics simulation offers a way how to calculate a free energy which is not directly comparable with an activation energy and one needs to estimate the entropy contribution of the transition state. The free energy was estimated to $\sim$ 1050 meV for both cubic lead titanate and cubic lead zirconate unit cell. However, we need to keep in mind that there is a huge energy error coming from the sparse k-points

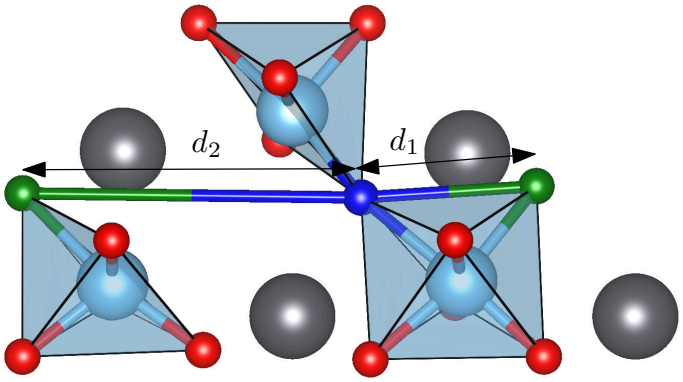

Figure 6.22: Collective variable used in the metadynamics simulation is defined as $d_1 - d_2$ for both systems. The blue oxygen is the moving one and the green oxygen atoms which are located along the motion are used to define the collective variable.

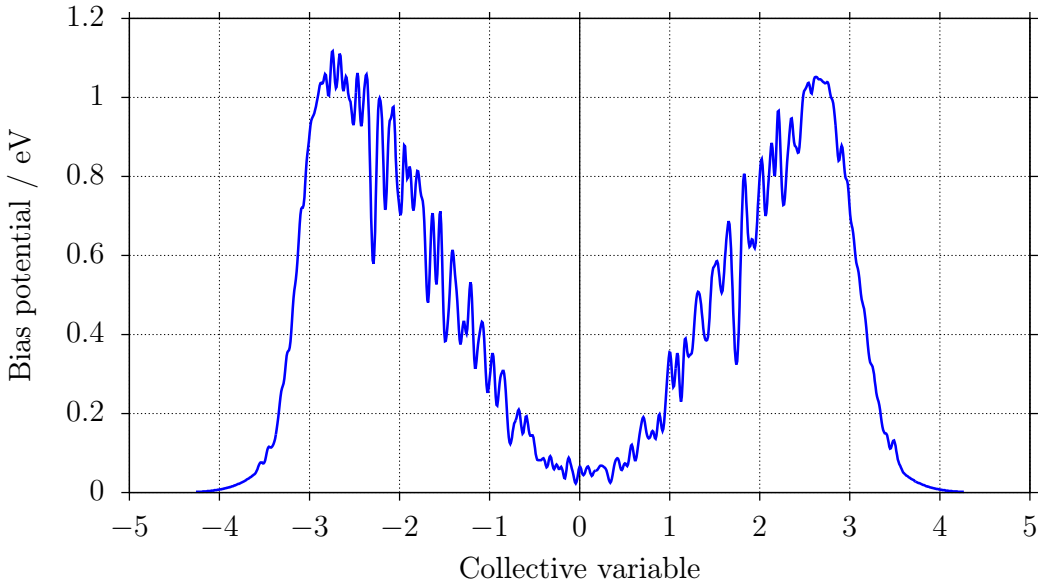

Figure 6.23: Sum of the Gaussian hills added as the bias potential to the collective variable. The transition state is correctly located at 0 where $d_1 = d_2$. The free energy is estimated to $\sim$ 1050 meV for lead titanate.

grid and we thus cannot compare these results with the activation energies calculated by NEB.

Nevertheless, the preliminary results show that metadynamics method is a promising way how to verify the barriers obtained with nudged elastic band method for the following reasons:

- The minimum and maxima of the obtained curves are located at correct positions. The transition state is related to the zero-point where the distances d_1 and d_2 in figure 6.22 are equal.
- Also the positions of maxima are located at the expectable values of collective variable – we receive the same value for the initial and final ground state systems

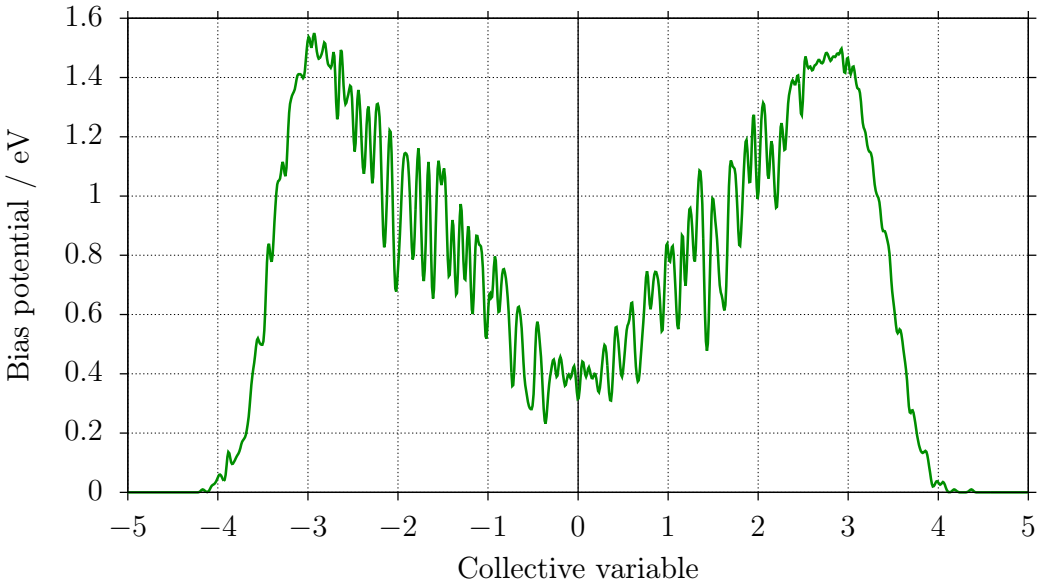

Figure 6.24: Sum of the Gaussian hills added as the bias potential to the collective variable. The transition state is correctly located at 0 where $d_1 = d_2$. The free energy is estimated to $\sim 1050\,\text{meV}$ for lead zirconate as well.

- Both peaks are symmetric which is in agreement with the symmetry of the cubic cell

7. Application of DFT on PZT alloys

In the last chapter of this work we move to the mixed alloys of lead zirconate and lead titanate and we will describe the influence of increasing concentration of zirconium on the activation energies in lead zirconate titanate. We used PBE functional and the same calculation setup as in the case of the separate bulk phases. In the first section of this chapter, we will move to the $PbZr_{0.125}Ti_{0.875}O_3$ alloy where one titanium atom is replaced by zirconium. To investigate the influence on activation energies of the oxygen vacancy diffusion, we will discuss the obtained barriers in the $PbZr_{0.25}Ti_{0.75}O_3$ material where two zirconium atoms replace titanium atoms in 2x2x2 supercells.

7.1. $PbZr_{0.125}Ti_{0.875}O_3$ alloy

The calculated structure of the $PbZr_{0.125}Ti_{0.875}O_3$ mixture is shown in figure 7.1. The unit cell has the cubic symmetry with lattice parameter 8.005 Å. This number is in agreement with the result from the previous chapter because the lattice parameter is slightly increased compared to the cubic lead titanate lattice parameter (3.96 Å). We also wouldn't expect any lattice distortions because the perturbation is uniformly distributed in the material.

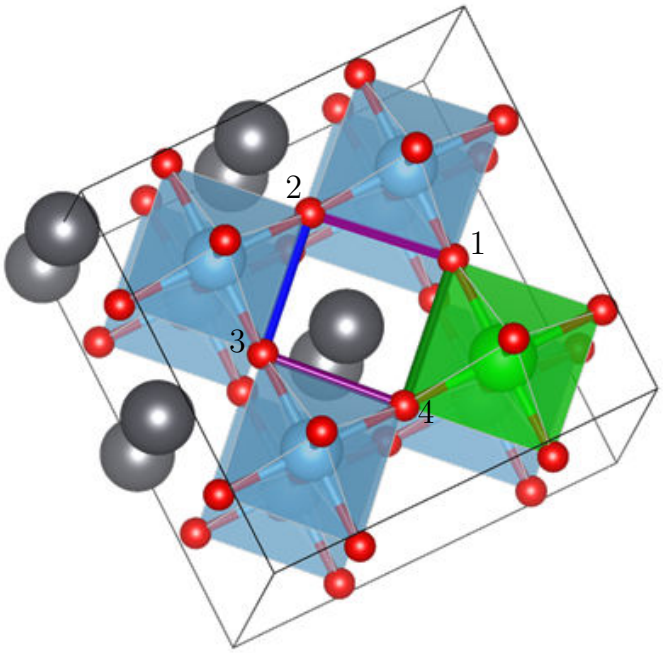

Figure 7.1: Structure of $PbZr_{0.125}Ti_{0.875}O_3$ alloy. The marked oxygen-oxygen bonds show the investigated oxygen vacancy paths.

The density of states is shown in figure 7.2. The plot is similar to the cubic lead titanate and the impurity states coming from the zirconium are neither in valence nor conduction band significant.

To see how the zirconium atom influences the energy barriers, we set up the nudged elastic band calculations along the green, violet and blue path which are shown in figure

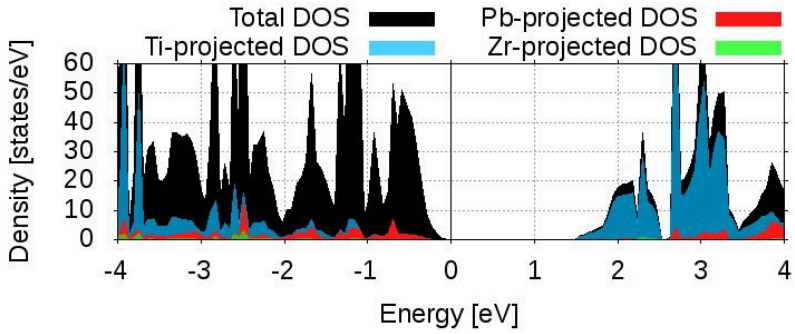

Figure 7.2: Density of states of the bulk $PbZr_{0.125}Ti_{0.875}O_3$ alloy. The energy gap between the conduction and valence band is equal to 1.52 eV. The conduction band is mainly composed of the titanium states.

7.1. Considering these paths, there are two unequal positions of the oxygen vacancy – zirconium-titanium position (number 1 and 4) and titanium-titanium position (2 and 3). We expect that the energy barriers of violet paths which are symmetric will be the same. Figure 7.3 shows the change of the density of states in the PZT material when the oxygen vacancy is created at the position "2" or "3" (figure 7.3a) and "1" or "4" (figure 7.3b). In both cases, the plots are similar to each other and also correspond to the plots for the lead titanate phase.

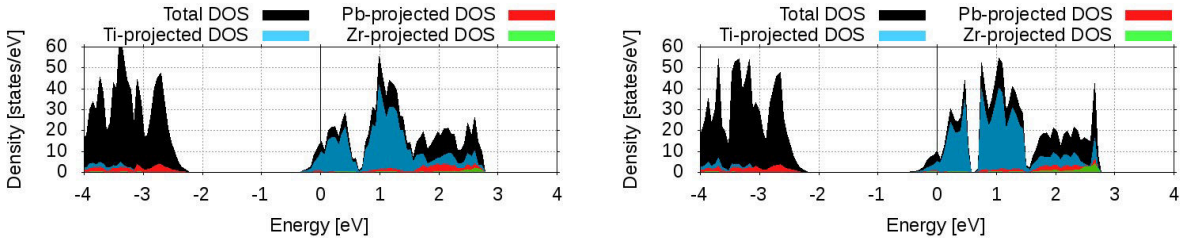

(a) DOS plot with the oxygen vacancy placed between two titanium atoms. The band gap value is estimated to 1.72 eV.

(b) DOS plot with the oxygen vacancy placed between titanium and zirconium atoms. The band gap value is estimated to 1.47 eV.

Figure 7.3: Density of states for the $PbZr_{0.125}Ti_{0.875}O_3$ alloy calculated with PBE functional with an oxygen vacancy placed at two different positions.

Formation energies of an oxygen vacancy were calculated for the positions "1" and "2" in the same way as in the previous chapter. The calculated values for these positions are 4.37 eV and 4.05 eV respectively, which means that it is easier to remove the atom neighboring with titanium and zirconium.

To see how the zirconium atom influences the energy barriers in this PZT alloy, we used the Nudged Elastic Band (NEB) method to scan the circular path shown in figure 7.1. The results are in agreement with the energy barriers of the separate phases. The highest barrier is related to the motion of the oxygen vacancy along the zirconium octahedra. We can also see that the violet barriers which correspond to the motion of the oxygen vacancy along the titanium octahedra neighboring with the zirconium atoms are asymmetric and the initial and final positions are not energetically equal. This is caused by the difference

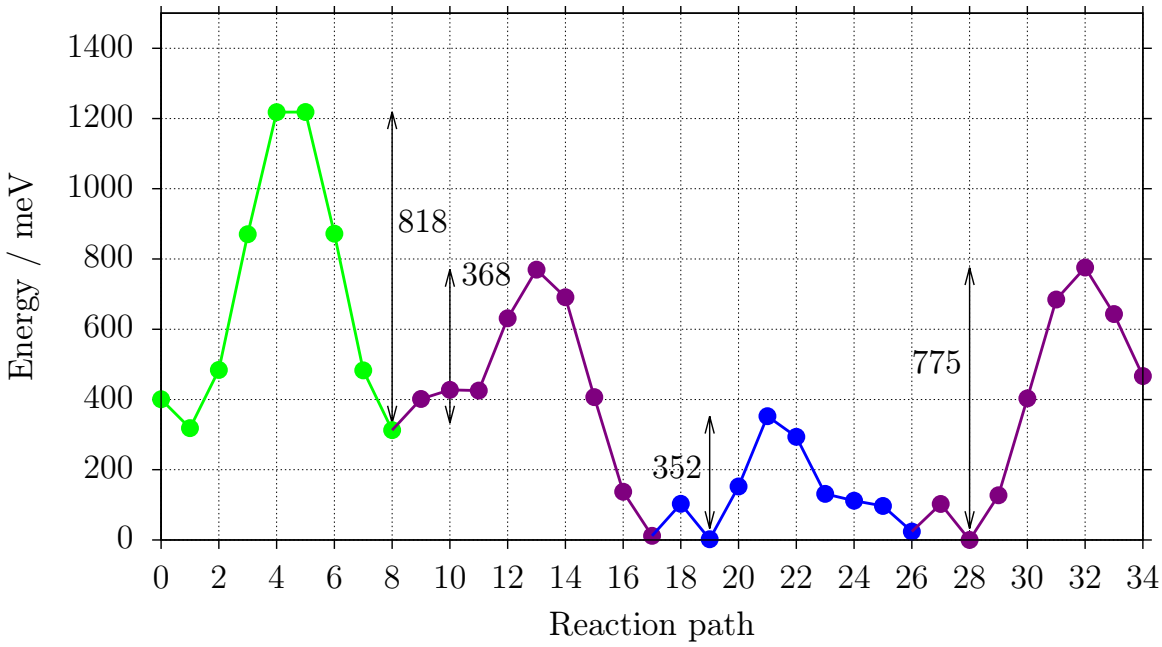

Figure 7.4: Energy barriers calculated with nudged elastic band method for the marked paths in image 7.1. The colors correspond to the investigated paths: the barriers mark the "4"-"1", "1"-"2", "2"-"3" and "3"-"4" paths related to the motion of the oxygen vacancy.

between the formation energy which prefers to place an oxygen vacancy to the titanium octahedra opposite to the zirconium atom.

From the NEB results we can see that zirconium atoms changes the barriers only in the close surrounding and it doesn't influence the motion of the oxygen vacancy in the non-neighboring titanium octahedra. The second section is focused on a lead zirconate titanate mixture where another zirconium atom replaces titanium and the barriers behave differently.

7.2. $PbZr_{0.25}Ti_{0.75}O_3$ alloy

$PbZr_{0.25}Ti_{0.75}O_3$ is the smallest supercell where we can investigate the influence of distribution of tetravalent atoms on structural and electronic properties. There are three possibilities how to build a 2x2x2 supercell which contains two zirconium atoms. As the first step, we investigated bulk properties of these structures which are shown in figure 7.5 and we called the "neighbor" (fig. 7.5a), "corner" (fig. 7.5b) and "cross" (fig. 7.5c) configurations, depending on the distribution of zirconium atoms in the supercell.

All presented calculations were performed with PBE functional. The structures were optimized to their equilibrium volume with the same procedure as the PZT structure in the previous section. A comparison of the structural properties is shown in table 7.1. We can observe a minor tetragonal distortion for the "neighbor" and "cross" configurations with c/a ratio 1.003 and 1.0003 respectively, while the "corner" unit cell stays cubic because zirconium atoms are uniformly distributed in the supercell. Table shows only a minor changes of the lattice parameters and the structures have therefore comparable volume.

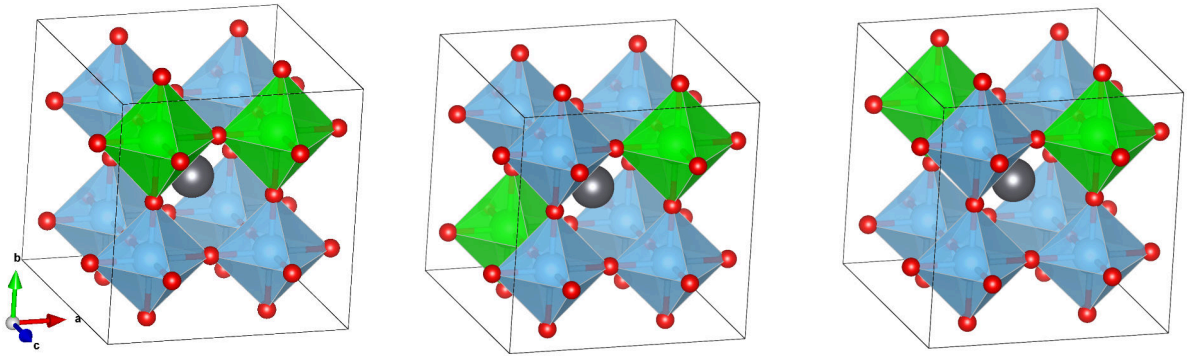

(a) "neighbor" structure (b) "corner" structure (c) "cross" structure

Figure 7.5: Investigated supercells of $PbZr_{0.25}Ti_{0.75}O_3$ alloy.

The main difference between these configurations is in the total energy. As we can see, the "cross" configuration is the most stable and the total energy difference between "neighbor" and "corner" configurations are 23.5 meV/f.u. and 12.9 meV/f.u. respectively.

Structure	a [Å]	b [Å]	c [Å]	V [Å^3]	E_b [eV]
"neighbor"	8.09	8.06	8.06	525.39	-302.013
"corner"	8.06	8.06	8.06	523.82	-302.098
"cross"	8.06	8.07	8.06	524.18	-302.201

Table 7.1: Structural properties of all possible configurations of $PbZr_{0.25}Ti_{0.75}O_3$. E_b notes the bulk energy of the whole supercell.

Density of states for the most stable "cross" configuration is shown in figure 7.6. It is surprising that there is not any significant change compared to $PbZr_{0.125}Ti_{0.875}O_3$ alloy. Even when another zirconium atom is placed to the supercell, we cannot see the change in the projected states to the lead or to the zirconium atoms. The band gap value is almost the same, 1.53 eV.

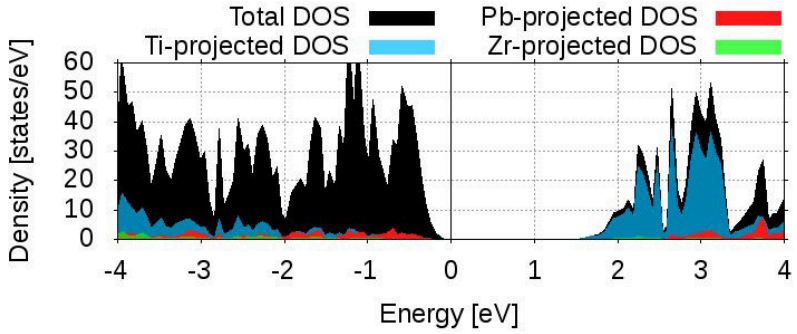

Figure 7.6: Density of states of the bulk $PbZr_{0.25}Ti_{0.75}O_3$ alloy. The energy gap between the conduction and valence band is equal to 1.53 eV. The conduction band is mainly composed of the titanium states.

However, we observed that the oxygen vacancy influences density of states in a different way. Figure 7.7 shows the calculated DOS for three different positions of the oxygen vacancy. All DOS plots are comparable and we can see that the gap states are located in the middle of the gap. It is also shown that these states are partially located in lead atoms and we can therefore expect higher energy barriers as we observed for the lead zirconate in the previous chapter.

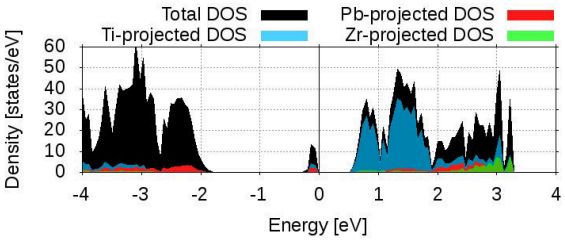

(a) DOS calculated for the "cross" supercell with an oxygen vacancy placed between two titanium octahedra. The energy gap between the valence and conduction band is equal to 2.25 eV.

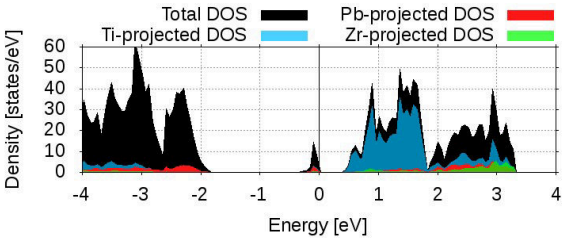

(b) DOS calculated for the "cross" supercell with an oxygen vacancy placed between titanium and zirconium octahedra. The energy gap between the valence and conduction band is equal to 2.08 eV.

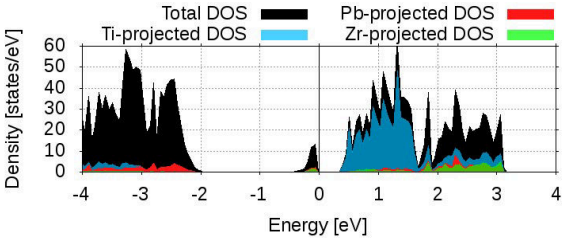

(c) DOS calculated for the "neighbor" supercell with an oxygen vacancy placed between two zirconium octahedra. The energy gap between the valence and conduction band is equal to 2.25 eV.

Figure 7.7: Density of states for different $PbZr_{0.25}Ti_{0.75}O_3$ positions of an oxygen vacancy.

Formation energies are consistent with the results from the previous section. As the table 7.2 shows, we calculated formation energies of an oxygen vacancy for all configurations considering all possible locations. The formation energies are only dependent on the two neighboring tetravalent atoms and we can see that the positions between two titanium octahedra are again the most preferred with respect to the formation energy. In

Configuration	Ti-Ti	Zr-Ti	Zr-Zr
"neighbor"	3.49-3,51	3.80	4.13
"corner"	3.56-3.57	3.92-3.93	–
"cross"	3.61-3.65	3.99-4.03	–

Table 7.2: Formation energies of the oxygen vacancy in all configurations considering the relevant positions.

the end of this section, we present an initial guess of the energy barriers calculated with

nudged elastic band method. Table 7.3 shows the obtained energy differences between the ground state and the NEB image with the highest energy. We can clearly see that the energy barriers are increased globally in the whole unit cell. Furthermore, the height of the energy barriers is comparable between the systems and it doesn't depend on the position of a zirconium atom with respect to the reaction path. This result corresponds to the statement that the energy barriers are increased due to the localization of the "gap states" charge density in a lead plane which we observed in all DOS plots for the structures with an oxygen vacancy at different positions.

Initial position	Final position	"Neighbor"	"Corner"	"Cross"
Ti-Ti	Ti-Ti	1006	1082	999
Ti-Ti	Zr-Ti	871, 1104	1470, 1268	1349
Zr-Ti	Zr-Ti	1163	1324	1072, 1198, 914
Zr-Ti	Zr-Zr	1190	–	–

Table 7.3

8. Conclusion

This diploma thesis deals with the structural and electronic properties of perovskite lead titanate, lead zirconate and their mixed compounds, in order to determine energy barriers for the diffusion of oxygen vacancies for different structural phases and diffusion paths. We performed Density Functional Theory calculations with periodic boundary conditions implemented in state-of-the-art computer codes using methods for mapping the diffusion barriers, namely the Nudged Elastic Band (NEB) method, the Dimer method and Metadynamics.

In the initial part of this work, we studied the vacancy diffusion in the bare systems. The oxygen vacancies pass through this materials along the sides of the oxygen octahedra surrounding the titanium or zirconium atoms. We found that, employing both the NEB and the dimer method, the energy barriers are much lower in lead titanate (400 meV - 650 meV) than in lead zirconate (1480 meV - 1780 meV). We conclude that this unexpected result is caused by a different localization of the electronic states related to the formation of an oxygen vacancy. In the case of lead titanate, these states are located at the titanium atoms and do not change significantly during the diffusion of an oxygen vacancy. However, in the case of lead zirconate, the vacancy states are forming localized bonds to the lead atoms, making the moving oxygen less mobile. We also discussed other effects which might influence the barriers, like the dependency on different phases. e.g. cubic vs. tetragonal, size of the supercell or chosen DFT functional. Finally, we presented an outlook with preliminary metadynamics simulations at 700 K, which offer a promising way how to assess the values obtained with NEB or Dimer method, which are treating the systems in the energetic ground state, corresponding to a temperature of 0 K. Thereafter we used these insights to build appropriate models of the mixed phases by replacement of titanium atoms by zirconium in 2x2x2 mixed lead titanate-zirconate supercells. Also for the mixed systems we found a strong dependency of the formation energy of the oxygen vacancy and the neighboring Ti/Zr cation. There was in both cases ~ 350 meV energy difference between the formation energy of the oxygen vacancy between two titanium atoms and between one titanium and one zirconium atom. The height of the barriers is dependent on the localization of vacancy states as in the case of pure phases.

While the energy barriers in the $PbZr_{0.125}Ti_{0.875}O_3$ supercell were influenced only locally by the zirconium atom and their heights corresponds to the results obtained for the separate bulk phases, in the $PbZr_{0.25}Ti_{0.75}O_3$ alloy all barriers are increased to values between 871 meV and 1349 meV which shows no correspondence to the pure lead titanate barriers anymore. The reason for the increase of the barriers is the same as in lead zirconate – the vacancy states are localized again in the lead planes so that a moving oxygen vacancy feels a larger restraining force.

Regarding the experimental data [50], the activation energy of a corresponding lead-free material is roughly 900 meV and the diffusion coefficients measured for lead zirconate titanate is 500 meV higher. This finding can be rationalized if we assume that the reactant is only short-lived in a mixed titanium-zirconium site, increasing the effective barrier by 350 meV. Furthermore, the experimentally investigated alloy was $PbZr_{0.6}Ti_{0.4}O_3$ with a higher Zr:Ti ratio. We therefore suggest that there are specific sites between titanium atoms where the oxygen vacancies are trapped, because they need to overcome an additional energy penalty as compared to starting already a site between a titanium and zirconium atom, where the initial energy is closer to the barrier maximum.

Bibliography

[1] MARINI, Andrea, S. PONCÉ and X. GONZE. Many-body perturbation theory approach to the electron-phonon interaction with density-functional theory as a starting point. *Physical Review B*. 2015, **91**(22). DOI: 10.1103/PhysRevB.91.224310.

[2] MARTIN, Richard M. *Electronic structure: basic theory and practical methods*. New York: Cambridge University Press, 2008. ISBN 978-0521534406.

[3] LEACH, Andrew R. *Molecular Modelling: Principles and applications*. 2nd ed. Harlow: Prentice Hall, 2001, 744 s. ISBN 05-823-8210-6.

[4] ANDERSON, E. *LAPACK users' guide*. 3rd ed. Philadelphia: Society for Industrial and Applied Mathematics, 1999. ISBN 08-987-1447-8.

[5] DAVID SHERRILL, C. and Henry F. SCHAEFER. The Configuration Interaction Method: Advances in Highly Correlated Approaches. *Advances in quantum chemistry*. 1999, **34**, 143-269. DOI: 10.1016/S0065-3276(08)60532-8.

[6] ČÍŽEK, Jiří. On the Correlation Problem in Atomic and Molecular Systems. Calculation of Wavefunction Components in Ursell-Type Expansion Using Quantum-Field Theoretical Methods. *The Journal of Chemical Physics*. 1966, **45**(11), 4256-4266. DOI: 10.1063/1.1727484.

[7] MØLLER, Chr. and M. S. PLESSET. Note on an Approximation Treatment for Many-Electron Systems. *Physical Review*. 1934, **46**(7), 618-622. DOI: 10.1103/PhysRev.46.618.

[8] STROUT, Douglas L. and Gustavo E. SCUSERIA. A quantitative study of the scaling properties of the Hartree–Fock method. *The Journal of Chemical Physics*. 1995, **102**(21), 8448-8452. DOI: 10.1063/1.468836.

[9] HOHENBERG, P. and W. KOHN. Inhomogeneous Electron Gas. *Physical Review*. 1964, **136**(3B), B864-B871. DOI: 10.1103/PhysRev.136.B864.

[10] KOHN, W. and L. J. SHAM. Self-Consistent Equations Including Exchange and Correlation Effects. *Physical Review*. 1965, **140**(4A), A1133-A1138. DOI: 10.1103/PhysRev.140.A1133.

[11] ROBERT G. PARR and WEITAO YANG. *Density-functional theory of atoms and molecules*. Reprint. New York: Oxford University Press, 1989. ISBN 978-019-5092-769.

[12] PERDEW, John P., J. A. CHEVARY, S. H. VOSKO, Koblar A. JACKSON, Mark R. PEDERSON, D. J. SINGH and Carlos FIOLHAIS. Atoms, molecules, solids, and surfaces: Applications of the generalized gradient approximation for exchange and correlation. *Physical Review B*. 1992, **46**(11). DOI: 10.1103/PhysRevB.46.6671.

[13] HE, Lianhua, Fang LIU, Geoffroy HAUTIER, et al. Accuracy of generalized gradient approximation functionals for density-functional perturbation theory calculations. *Physical Review B*. 2014, **89**(6). DOI: 10.1103/PhysRevB.89.064305.

[14] PERDEW, John P. Density functional theory and the band gap problem. *International Journal of Quantum Chemistry*. 1985, **28**(S19), 497-523. DOI: 10.1002/qua.560280846.

[15] PERDEW, John P., Kieron BURKE and Matthias ERNZERHOF. Generalized Gradient Approximation Made Simple. *Physical Review Letters*. 1996, **77**(18), 3865-3868. DOI: 10.1103/PhysRevLett.77.3865.

[16] PERDEW, John P., Adrienn RUZSINSZKY and Gábor I. CSONKA. Restoring the Density-Gradient Expansion for Exchange in Solids and Surfaces. *Physical Review Letters*. 2008, **100**(13). DOI: 10.1103/PhysRevB.89.064305.

[17] BYLANDER, D.M. and LEONARD KLEINMAN. The optimized effective potential for atoms and semiconductors. *International journal of modern physics B*. 1996, **10**(4), 399-425. DOI: 10.1142/S0217979296000167.

[18] KOCH, Wolfram and Max HOLTHAUSEN. *A chemist's guide to density functional theory*. 2nd ed. Weinheim: Wiley-VCH, 2002, xiii, 300 s. ISBN 35-273-0422-3.

[19] HEYD, Jochen, Gustavo E. SCUSERIA and Matthias ERNZERHOF. Hybrid functionals based on a screened Coulomb potential. *Journal of chemical physics*. 2003, **118**(18), 8207-8215. DOI: 10.1063/1.1564060.

[20] SLATER, J. C. An Augmented Plane Wave Method for the Periodic Potential Problem. *Physical Review*. 1953, **92**(3), 603-608. DOI: 10.1103/PhysRev.92.603.

[21] NEZVAL, David. *Výpočty interakce systému grafen/SiO2 s adsorbovanými atomy a molekulami pomocí DFT metod*. Brno, 2015, 52 s. Diplomová práce. Vysoké učení technické v Brně, Fakulta strojního inženýrství. Vedoucí práce Ing. Miroslav Bartošík, Ph.D.

[22] HAMANN, D. R., M. SCHLÜTER and C. CHIANG. Norm-Conserving Pseudopotentials. *Physical Review Letters*. 1979, **43**(20), 1494-1497. DOI: 10.1103/PhysRevLett.43.1494.

[23] VANDERBILT, David. Soft self-consistent pseudopotentials in a generalized eigenvalue formalism. *Physical Review B*. 1990, **41**(11), 7892-7895. DOI: 10.1103/PhysRevB.41.7892.

[24] BLÖCHL, P. E. Projector augmented-wave method. *Physical review B*. 1994, **50**(24), 1758-1775. DOI: 10.1103/PhysRevB.50.17953.

[25] ROSTGAARD, Carsten. *The Projector Augmented-wave Method* [online]. Cornell University Library, 2009 [cit. 2017-04-24]. Dostupné z: arXIv:0910.1921

[26] KRESSE, G. and D. JOUBERT. From ultrasoft pseudopotentials to the projector augmented-wave method. *Physical Review B*. 1999, **59**(3), 1758-1775. DOI: 10.1103/PhysRevB.59.1758.

[27] KRESSE, G. and J. FURTHMÜLLER. Efficient iterative schemes for ab initio total-energy calculations using a plane-wave basis set. *Physical Review B*. 1996, **54**(16), 11169-11186. DOI: 10.1103/PhysRevB.54.11169.

[28] Vienna Simulation Ab-initio Package. [*Vasp manual*] [online]. Vienna: Kresse, 2016 [cit. 2017-04-25]. Dostupné z: http://cms.mpi.univie.ac.at/vasp/vasp/vasp.html

[29] WOOD, D M and A ZUNGER. A new method for diagonalising large matrices. *Journal of physics a-mathematical and general*. 1985, **18**(9), 1343-1359. DOI: 10.1088/0305-4470/18/9/018.

[30] DAVIDSON, Ernest. *Methods in Computational Molecular Physics*. Dordrecht: Springer Netherlands, 1983, s. 95-113. ISBN 9789400972001.

[31] PACK, James D. and Hendrik J. MONKHORST. "Special points for Brillouin-zone integrations"—a reply. *Physical review B*. 1977, **16**(4), 1748-1749. DOI: 10.1103/PhysRevB.16.1748.

[32] *Classical and quantum dynamics in condensed phase simulations*. Singapore [u.a.]: World Scientific, 1998, s. 385-404. ISBN 9789810234980.

[33] Reaction path optimization using the Nudged Elastic Band method. In: *Atomistix ToolKit* [online]. Copenhagen: QuantumWise, 2008 [cit. 2017-05-23]. Dostupné z: https://quantumwise.com/documents/manuals/ATK-2008.10/chap.relax.html

[34] HENKELMAN, Graeme and Hannes JÓNSSON. A dimer method for finding saddle points on high dimensional potential surfaces using only first derivatives. *The Journal of Chemical Physics*. 1999, **111**(15), 7010-7022. DOI: 10.1063/1.480097.

[35] VAN SPEYBROECK, Veronique, Kristof DE WISPELAERE, Jeroen VAN DER MYNSBRUGGE, Matthias VANDICHEL, Karen HEMELSOET and Michel WAROQUIER. First principle chemical kinetics in zeolites: the methanol-to-olefin process as a case study. *Chemical society reviews*. 2014, **43**(21), 7326-7357. DOI: 10.1039/C4CS00146J.

[36] BARDUCCI, Alessandro, Massimiliano BONOMI and Michele PARRINELLO. Metadynamics. *Wiley interdisciplinary reviews-computational molecular science*. 2011, **1**(5), 826-843. DOI: 10.1002/wcms.31. ISBN 10.1002/wcms.31.

[37] WOODWARD, David I., Jesper KNUDSEN and Ian M. REANEY. Review of crystal and domain structures in the $PbZr_xTi_{1-x}O_3$ solid solution. *Physical Review B*. 2005, **72**(10). DOI: 10.1103/PhysRevB.72.104110.

[38] NOHEDA, B., D. E. COX, G. SHIRANE, J. A. GONZALO, L. E. CROSS and S-E. PARK. A monoclinic ferroelectric phase in the Pb(Zr1−xTix)O3 solid solution. *Applied Physics Letters*. 1999, **74**(14), 2059-2061. DOI: 10.1063/1.123756.

[39] YOKOTA, H., N. ZHANG, A. E. TAYLOR, P. A. THOMAS and A. M. GLAZER. Crystal structure of the rhombohedral phase of $PbZr_{1-x}Ti_xO_3$ ceramics at room temperature. *Physical Review B*. 2009, **80**(10), -. DOI: 10.1103/PhysRevB.80.104109.

[40] HINTERSTEIN, M., J. ROUQUETTE, J. HAINES, Ph. PAPET, J. GLAUM, M. KNAPP, J. ECKERT and M. HOFFMAN. Structural contribution to the ferroelectric fatigue in lead zirconate titanate ceramics. *Physical Review B*. 2014, **90**(9), 1073-1079. DOI: 10.1103/PhysRevB.90.094113.

[41] NOHEDA, B., D. E. COX, G. SHIRANE, R. GUO, B. JONES and L. E. CROSS. Stability of the monoclinic phase in the ferroelectric perovskite $PbZr_{1-x}Ti_xO_3$. *Physical Review B*. 2000, **63**(1). DOI: 10.1103/PhysRevB.63.014103.

[42] PANDA, P. K. Review: environmental friendly lead-free piezoelectric materials. *Journal of materials science*. 2009, **44**(19), 5049-5062. DOI: 10.1007/s10853-009-3643-0.

[43] CAO, Y., G. SHENG, J. X. ZHANG, S. CHOUDHURY, Y. L. LI, C. A. RANDALL and L. Q. CHEN. Piezoelectric response of single-crystal $PbZr_{1-x}Ti_xO_3$ near morphotropic phase boundary predicted by phase-field simulation. *Applied Physics Letters*. 2010, **97**(25). DOI: 10.1063/1.3530443.

[44] DUBOIS, Marc-Alexandre and Paul MURALT. Measurement of the effective transverse piezoelectric coefficient e31,f of AlN and $Pb(Zr_x,Ti_{1-x})O_3$ thin films. *Sensors and actuators A-Physical*. 1999, **77**(2), 106-112. DOI: 10.1016/S0924-4247(99)00070-9.

[45] KIM, Young-Sik, Hyo-Jin NAM, Seong-Moon CHO, Jae-Wan HONG, Dong-Chun KIM and Jong U. BU. PZT cantilever array integrated with piezoresistor sensor for high speed parallel operation of AFM. *Sensors and actuators A-Physical*. 2002, **103**(1-2), 122-129. DOI: 10.1016/S0924-4247(02)00311-4.

[46] JONES, R.E., P.D. MANIAR, R. MOAZZAMI, P. ZURCHER, J.Z. WITOWSKI, Y.T. LII, P. CHU and S.J. GILLESPIE. Ferroelectric non-volatile memories for low-voltage, low-power applications. *Thin solid films*. 1995, **270**(1-2), 584-588. DOI: 10.1016/0040-6090(95)06754-X. ISBN 10.1016/0040-6090(95)06754-X. Dostupné také z: http://linkinghub.elsevier.com/retrieve/pii/004060909506754X

[47] IZYUMSKAYA, N., Y. -I. ALIVOV, S. -J. CHO, H. MORKOÇ, H. LEE and Y. -S. KANG. Processing, Structure, Properties, and Applications of PZT Thin Films. *Critical reviews in solid state and materials sciences*. 2007, **32**(3-4), 111-202. DOI: 10.1080/10408430701707347.

[48] EZHILVALAVAN, S. and Victor D. SAMPER. Ferroelectric properties of sol-gel derived Ca modified $PbZr_{0.52}Ti_{0.48}O_3$ films. *Applied Physics Letters*. 2005, **87**(13). DOI: 10.1063/1.2041820.

[49] NGUYEN, Minh D., Thong Q. TRINH, Matthijn DEKKERS, Evert P. HOUWMAN, Hung N. VU and Guus RIJNDERS. Effect of dopants on ferroelectric and piezoelectric properties of lead zirconate titanate thin films on Si substrates. *Ceramics international*. 2014, **40**(1), 1013-1018. DOI: 10.1016/j.ceramint.2013.06.098.

[50] SLOUKA, Christoph, Theresa KAINZ, Edvinas NAVICKAS, Gregor WALCH, Herbert HUTTER, Klaus REICHMANN and Jürgen FLEIG. The Effect of Acceptor and Donor Doping on Oxygen Vacancy Concentrations in Lead Zirconate Titanate (PZT). *Materials*. 2016, **9**(11). DOI: 10.3390/ma9110945.

[51] BOUKAMP, B, M PHAM, D BLANK and H BOUWMEESTER. Ionic and electronic conductivity in lead–zirconate–titanate (PZT). *Solid state ionics*. 2004, **170**(3-4), 239-254. DOI: 10.1016/j.ssi.2004.03.005.

[52] SLOUKA, Christoph, Gerald HOLZLECHNER, Lukas ANDREJS, Edvinas NAVICKAS, Herbert HUTTER, Jürgen FLEIG and H. CHAN. Oxygen Ion Conduction in Bulk and Grain Boundaries of Nominally Donor-Doped Lead Zirconate Titanate (PZT): A Combined Impedance and Tracer Diffusion Study. *Journal of the American Ceramic Society*. 2015, **98**(10), 3259-3269. DOI: 10.1111/jace.13769.

[53] DENK, Ingrid, Wolfram MÜNCH and Joachim MAIER. Partial Conductivities in $SrTiO_3$: Bulk Polarization Experiments, Oxygen Concentration Cell Measurements, and Defect-Chemical Modeling. *Journal of the American Ceramic Society*. 1995, **78**(12), 3265-3272. DOI: 10.1111/j.1151-2916.1995.tb07963.x.

[54] EYRAUD, Lucien, Paul GONNARD and Bernard CLAUDEL. Causes of Instability and Aging of Piezoelectric Power Ceramics. *Journal of the American Ceramic Society*. 1990, **73**(7), 1854-1856. DOI: 10.1111/j.1151-2916.1990.tb05234.x.

[55] INAGUMA, Yoshiyuki, Kie TANAKA, Takeshi TSUCHIYA, et al. Synthesis, Structural Transformation, Thermal Stability, Valence State, and Magnetic and Electronic Properties of $PbNiO_3$ with Perovskite- and $LiNbO_3$ -Type Structures. *Journal of the American Chemical Society*. 2011, **133**(42), 16920-16929. DOI: 10.1021/ja206247j.

[56] GOODENOUGH, John B and Jianshi ZHOU. Varied roles of Pb in transition-metal $PbMO_3$ perovskites (M = Ti, V, Cr, Mn, Fe, Ni, Ru). *Science and Technology of Advanced Materials*. 2016, **16**(3). DOI: 10.1088/1468-6996/16/3/036003.

[57] SÁGHI-SZABÓ, Gotthard, Ronald E. COHEN and Henry KRAKAUER. First-principles study of piezoelectricity in tetragonal $PbTiO_3$ and $PbZr_{1/2}Ti_{1/2}O_3$. *Physical review B*. 1999, **59**(20), 12771-12776. DOI: 10.1103/PhysRevB.59.12771.

[58] PONTES, D. S. L., L. GRACIA, F. M. PONTES, A. BELTRÁN, J. ANDRÉS and E. LONGO. Synthesis, optical and ferroelectric properties of PZT thin films: experimental and theoretical investigation. *Journal of materials chemistry*. 2012, **22**(14), 6587-6596. DOI: 10.1039/c2jm15150b.

[59] MOMMA, Koichi and Fujio IZUMI. VESTA 3 for three-dimensional visualization of crystal, volumetric and morphology data. *Journal of applied crystallography*. 2011, **44**, 1272-1276. DOI: 10.1107/S0021889811038970.

[60] SENGUPTA, S. S., D. ROBERTS, J.-F. LI, M. C. KIM and D. A. PAYNE. Field-induced phase switching and electrically driven strains in sol-gel derived antiferroelectric (Pb,Nb)(Zr,Sn,Ti)O_3 thin layers. *Journal of Applied Physics*. 1995, **78**(2), 1171-1177. DOI: 10.1063/1.360353.

[61] KOTOMIN, E. A., S. PISKUNOV, Yu. F. ZHUKOVSKII, R. I. EGLITIS, A. GOPEJENKO and D. E. ELLIS. The electronic properties of an oxygen vacancy at ZrO2-terminated (001) surfaces of a cubic $PbZrO_3$: computer simulations from the first principles. *Physical chemistry chemical physics*. 2008, **10**(29), 4258-4263. DOI: 10.1039/b802740d.

[62] NOHEDA, Beatriz, Noé CERECEDA, Tomás IGLESIAS, Ginés LIFANTE, Julio A. GONZALO, Hui Ting CHEN and Yong Ling WANG. Composition dependence of

the ferroelectric-paraelectric transition in the mixed system $PbZr_{1-x}Ti_xO_3$. *Physical Review B*. 1995, **51**(22), 16388-16391. DOI: 10.1103/PhysRevB.51.16388.

[63] AOYAGI, Shinobu, Yoshihiro KUROIWA, Akikatsu SAWADA, Hiroshi TANAKA, Jimpei HARADA, Eiji NISHIBORI, Masaki TAKATA and Makoto SAKATA. Direct Observation of Covalency between O and Disordered Pb in Cubic $PbZrO_3$. *Journal of the Physical Society of Japan*. 2002, **71**(10), 2353-2356. DOI: 10.1143/JPSJ.71.2353.

[64] TESLIC, S. and T. EGAMI. Atomic Structure of PbZrO 3 Determined by Pulsed Neutron Diffraction. *Acta Crystallographica Section B Structural Science*. 1998, **54**(6), 750-765. DOI: 10.1107/S0108768198003802.

[65] YOSHIASA, Akira, Tomotaka NAKATANI, Akihiko NAKATSUKA, Maki OKUBE, Kazumasa SUGIYAMA and Tsutomu MASHIMO. High-temperature single-crystal X-ray diffraction study of tetragonal and cubic perovskite-type $PbTiO_3$ phases. *Acta Crystallographica Section B Structural Science, Crystal Engineering and Materials*. 2016, **72**(3), 381-388. DOI: 10.1107/S2052520616005114.

[66] GLAZER, A. M. and S. A. MABUD. Powder profile refinement of lead zirconate titanate at several temperatures. II. Pure $PbTiO_3$. *Acta Crystallographica Section B Structural Crystallography and Crystal Chemistry*. 1978, **34**(4), 1065-1070. DOI: 10.1107/S0567740878004938.

[67] TINTE, S., M. G. STACHIOTTI, C. O. RODRIGUEZ, D. L. NOVIKOV and N. E. CHRISTENSEN. Applications of the generalized gradient approximation to ferroelectric perovskites. *Physical Review B*. 1998, **58**(18), 11959-11963. DOI: 10.1103/PhysRevB.58.11959.

[68] PERDEW, John P. Density functional theory and the band gap problem. *International Journal of Quantum Chemistry*. 1985, **28**(S19), 497-523. DOI: 10.1002/qua.560280846. ISSN 00207608. Dostupné také z: http://doi.wiley.com/10.1002/qua.560280846

[69] FRANCHINI, Cesare. Hybrid functionals applied to perovskites. *Journal of Physics: Condensed Matter*. 2014, **26**(25), 253202-. DOI: 10.1088/0953-8984/26/25/253202.

[70] ROBERTSON, John. Band offsets of wide-band-gap oxides and implications for future electronic devices. *Journal of Vacuum Science*. 2000, **18**(3), 1785-1791. DOI: 10.1116/1.591472.

[71] GOU, G. Y., J. W. BENNETT, H. TAKENAKA and A. M. RAPPE. Post density functional theoretical studies of highly polar semiconductive $Pb(Ti_{1-x}Ni_x)O_{3-x}$ solid solutions: Effects of cation arrangement on band gap. *Physical review B*. 2011, **83**(20). DOI: 10.1103/PhysRevB.83.205115.

[72] PISKUNOV, S., A. GOPEYENKO, E.A. KOTOMIN, Yu.F. ZHUKOVSKII and D.E. ELLIS. Atomic and electronic structure of perfect and defective PbZrO3 perovskite: Hybrid DFT calculations of cubic and orthorhombic phases. *Ferroelectrics*. 1992, **136**(1-4), 65-83. DOI: 10.1016/j.commatsci.2007.03.012.

[73] BLÖCHL, Peter E., O. JEPSEN and O. K. ANDERSEN. Improved tetrahedron method for Brillouin-zone integrations. *Physical review B*. 1994, **49**(23), 16223-16233. DOI: 10.1103/PhysRevB.49.16223.

[74] MILLS, Gregory, Hannes JÓNSSON and Gregory K. SCHENTER. Reversible work transition state theory: application to dissociative adsorption of hydrogen. *Surface Science*. 1995, **324**(2-3), 305-337. DOI: 10.1016/0039-6028(94)00731-4.

9. List of abbreviations

AFM Atomic Force Microscopy

APW Augmented Plane Waves

cPT cubic Lead Titanate

cPZ cubic Lead Zirconate

DFT Density Functional Theory

DOS Density Of States

GGA Generalized Gradient Approximation

HK Hohenberg-Kohn

KS Kohn-Sham

LAPACK Linear Algebra PACKage

LAPW Linearized Augmented Plane Wave

LCAO Linear Combination of Atomic Orbitals

LDA Local Density Approximation

MEP Minimum Energy Path

MPB Morphotropic Phase Boundary

NEB Nudged Elastic Band

NVRAM Non-Volatile Random-Access-Memory

oPZ orthorhombic Lead Zirconate

PAW Projector Augmented Wave

PDOS Projected Density Of States

PES Potential Energy Surface

PT Lead Titanate

PZ Lead Zirconate

PZT Lead Zirconate Titanate

SI International System

ToF-SIMS Time-of-Flight Secondary Ion Mass Spectroscopy

tPT tetragonal Lead Titanate